FABRICATION OF POLYMER/METAL OXIDE COMPOSITES THROUGH POLYMERIZATION-INDUCED PHASE SEPARATION AND CHARACTERIZATION OF THEIR MECHANICAL AND ELECTROCHEMICAL PROPERTIES

A Dissertation

Presented to

The Graduate Faculty of The University of Akron

In Partial Fulfillment

of the Requirements for the Degree

Doctor of Philosophy

Jeongwoo Lee

December, 2015

FABRICATION OF POLYMER/METAL OXIDE COMPOSITES THROUGH POLYMERIZATION-INDUCED PHASE SEPARATION AND CHARACTERIZATION OF THEIR MECHANICAL AND ELECTROCHEMICAL PROPERTIES

Jeongwoo Lee

Dissertation

Approved:	Accepted:
Advisor Dr. Bryan D. Vogt	Department Chair Dr. Sadhan C. Jana
Committee Member Dr. Alamgir Karim	Dean of the College Dr. Eric J. Amis
Committee Member Dr. Sadhan C. Jana	Dean of the Graduate School Dr. Chand Midha
Committee Member Dr. Yu Zhu	Date
Committee Member Dr. Homero Castaneda-Lopez	

ABSTRACT

Polymerization-induced phase separation of nanoparticle-filled solution is demonstrated as a simple approach to control the structure of polymer composites. Therefore, polymer/metal oxide nanocomposites are fabricated by the polymerization-induced phase separation and the composites are characterized their mechanical and electrochemical properties.

The first work was conducted on fabrication and characterization of poly(ethyl acrylate) (PEA)/poly(methyl methacrylate) (PMMA)/aluminium oxide (Al_2O_3) composite to confirm the effect of their morphologies on mechanical properties. The dispersion state of Al_2O_3 in the PEA/PMMA blend matrix has a decisive effect on mechanical properties of PEA/PMMA/Al_2O_3 composite materials. Since the interactions between the PEA/PMMA chains and Al_2O_3 nanoparticles are at work, the small-sized clusters and individual clusters of Al_2O_3 into the composites improve the tensile strength as compared with neat PEA/PMMA blend. On the contrary, the larger and interconnected clusters of Al_2O_3 bring several partial failures because of the severe modulus mismatch between polymer and Al_2O_3 nanoparticles.

When the polymer composite materials are pyrolyzed and then carbon composite materials are obtain, the carbon composites can be used for battery electrodes. Especially, the morphology of composite materials used in battery electrodes is critical to provide the

requisite transport paths for ions and electrons to enable high performance. Therefore, polymer nanocomposites are demonstrated as the active component for sodium ion battery anode. For fabrication of the composites, poly(hydroxybutyl methacrylate) (PHBMA) is dissolved in furfuryl alcohol (carbon precursor) containing a photoacid generator (PAG), and then titanium oxide (anatase, TiO_2) nanoparticles are dispersed in the solution. When the PAG exposes to UV, it turns into a strong acid that catalyzes the furfuryl alcohol polymerization. Carbonization of this polymer composite yields a porous nanocomposite. This nanocomposite exhibits nearly 3-fold greater gravimetric capacity in Na-ion batteries than the same titanium oxide nanoparticles that have been coated with carbon.

In addition, a simple and scalable method to tune the morphology of carbon/TiO_2 composite is described using polymerization-induced phase separation of a mixture containing commercial TiO_2 nanoparticles, poly(hydroxyethyl methacrylate) (PHEMA), and photoacid generator (PAG) dissolved in furfuryl alcohol (FA). The morphology is controlled by the molecular weight of PHEMA and FA concentration that impact the miscibility and mobility. The polymerized composite is carbonized to yield porous carbon/TiO_2 electrodes. Electrochemical impedance spectroscopy (EIS) analysis illustrates that subtle changes in synthetic conditions can dramatically impact the electrical or ion conductance, primarily through modulation in the solid electrolyte interphase (SEI). A careful investigation of the SEI layer on the porous carbon/TiO_2 composites demonstrates a clear correlation between the SEI and the surface area of the porous anode as determined by transmission electron microscopy (TEM) and X-ray photoelectron spectroscopy (XPS).

ACKNOWLEDGEMENTS

This thesis includes all my research works, which were conducted in Department of Polymer Engineering at The University of Akron, during the past five years. I would like to express my sincere gratitude to all those who helped me to accomplish my research.

First of all, I would like to thank my Ph.D advisor, Prof. Bryan D. Vogt, for his guidance, help, and providing me with great atmosphere and great opportunities for doing researches. I also appreciate all the help provided by Prof. Sang Eun Shim at Inha University (S. Korea) as a spiritual mainstay of my life and the helps from my other committee members.

Furthermore, I would like to expand my thanks to Young Ho Kim for his affection for me like father. I also appreciate all people who share with me for almost five years in my lab and all Korean students who have been through a lot together in Akron.

Finally, I would like to thank my parents, brother, and sister-in-law to trust my decision and take care of my life.

I believe that this achievement cannot be completed without any one of you.

TABLE OF CONTENTS

Page

LIST OF FIGURES

Figure Page

LIST OF TABLES

CHAPTER I

INTRODUCTION

1.1 Polymer phase separation

The polymer materials have consistently come into the spotlight with covering various fields of products from disposable cups to electronic devices due to their low price and excellent processability.[1] The improvement of their properties can be obtained through the control of structures of components. For example, it is an efficient method to blend different polymers which retain their individual properties to fabricate new nano- and microstructural polymer materials.[2] To understand and control the mechanisms of phase separation and nanostructure formation in the polymer blends should enable that the properties of polymer blends are adapted to various applications. For example, co-continuous polymer blends consisting of a main component with lower-melting point and an added component with higher-melting point are able to increase thermal and mechanical properties such as toughness, strain and stress at break, or high-temperature creep resistance.[2]

1.1.1 Mechanisms of phase separation

After the melt mixing of immiscible polymers to fabricate the polymer blends, the system proceeds towards the thermodynamic equilibrium state, which favors the phase separation for less miscible polymer mixture compared to the initial mixing state. The phase separation depends on the temperature and the composition of the polymer mixture and the relationships are illustrated as a phase diagram in Figure 1.1.

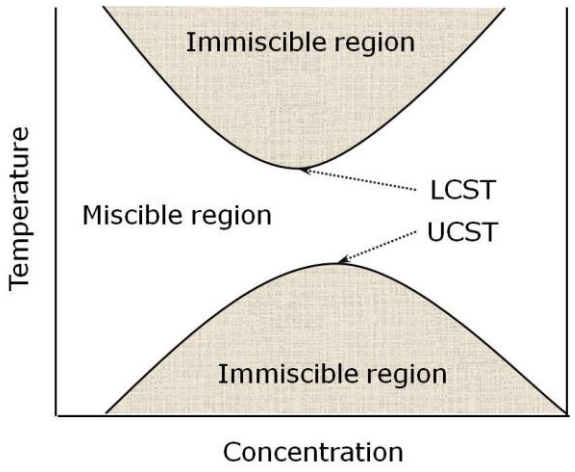

Figure 1.1. Phase diagram of a polymer blend illustrating that the polymer blend undergoes phase separation above the lower critical solution temperature (LCST) and below the upper critical solution temperature (UCST).[3]

The polymer blends are miscible when there are favorable specific interactions between the polymers leading to a negative value of the Gibbs free energy of mixing.[4] If the favorable interactions between the polymers are weak, the polymer mixture will exhibit an upper critical solution temperature (UCST). At lower temperature, the polymers are immiscible due to the weak interactions, whereas they are miscible at higher temperature because of increased the favorable interactions.[3] It is observed only when one or two components have relatively low molecular weight (oligomer).[4-6] On the other hand, miscible polymer-polymer mixtures tend to occur the phase separation between the

polymers at elevated temperatures.[4] This miscible polymer blends exhibit a lower critical solution temperature (LCST) behavior, which occurs as a general phenomenon in polymer solutions. They are miscible at lower temperature due to favorable interactions, while they are immiscible at higher temperature due to free volume differences.[3] The dissimilarity between the free volumes of polymers is due to the difference of size or chain length, and the smaller (or shorter) polymer is more expanded than the larger (or longer) polymer.[7]

A phase diagram can be classified into three regions; stable, metastable, and unstable regions as shown in Figure 1.2. The boarder lines that separate different regions have thermodynamic importance and are called binodal and spinodal curves.[8] The binodal curve is the equilibrium phase boundary between the single phase and the phase separated region,[9] and the spinodal curve is the limit of the metastable region.[10] In different regions of the phase diagram, the phase separation occurs through different mechanisms: nucleation-growth (NG) and spinodal decomposition (SD).

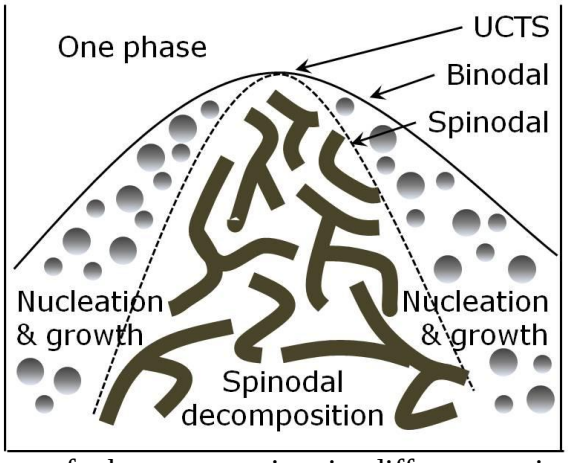

Figure 1.2. Mechanisms of phase separation in different regions of stability; phases separate as nucleation-growth (NG) in metastable region and spinodal decomposition (SD) in unstable region.

The nucleation-growth occurs in the metastable region of the phase diagram (the area between binodal and spinodal).[11] The change of a system from one-phase to two-phase state in the metastable region has relevance to amplification of fluctuations in the composition and to expansion of the microregions of a new phase. The diffusion flows of components in the metastable region occur towards decreasing fluctuations, and thus the phase separation in this case sequentially occurs as follows: the appearance, growth, and coalescence of microregions of developed new phase by evaporation or condensation.[12] On the other hand, the spinodal decomposition is the commonly observed mechanism for phase separation in homopolymer blends and occurs in the unstable region of the phase diagram. It results from small-amplitude concentration fluctuations that grow spontaneously into phase-separated regions.[13]

1.1.2 Crystallization

Another type of phase separation occurs in polymer blends when one of the components is crystallizable. Crystalline polymers usually exhibit excellent physical properties compared to amorphous polymers, and thus much research has interested in the crystallization behaviors and crystalline morphologies of the binary polymer blends with crystalline polymer(s).[14, 15]

The polymer crystallization is generally divided into three classes; primary nucleation, secondary nucleation and growth, and secondary crystallization.[16] The primary nucleation can be divided into two classes; homogeneous nucleation and heterogeneous nucleation. The homogeneous nucleation is the sporadic formation of critical nuclei from the pure phase, whereas heterogeneous nucleation occurs at the

surface of impurities within the system.[17] After the primary nucleation, polymer chains will diffuse to the growth front and crystallize further, which is called secondary nucleation and growth because it nucleates the growth of a single new layer.[16, 18]

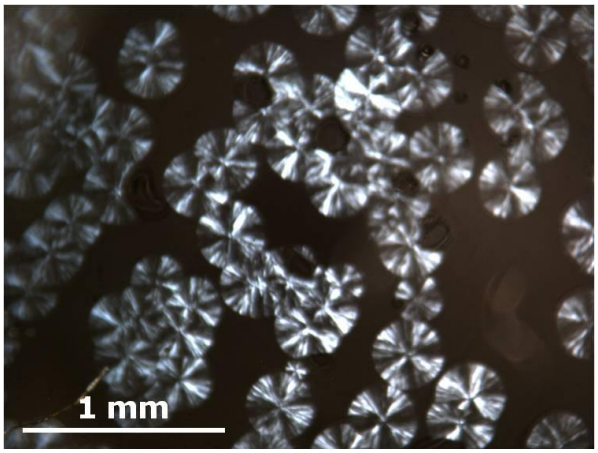

Figure 1.3. Spherulites images of polybutene at 90°C and annealing time of 90 seconds.

When polymer chains are crystallized from the melt, spherulites (sphere-shaped crystalline structures as shown in Figure 1.3) can be obviously observed, and the spherulite growth can continue microscopically in the amorphous regions between lamellae, this is called secondary crystallization.[16, 19]

1.1.3 Polymerization-induced phase separation

The initially homogeneous solution of a nonreactive component in reactive monomers can be occurred the phase separation during polymerization of the monomers, which is known as polymerization-induced phase separation (PIPS).[20, 21] Initially, monomers and other polymers (or low molecular weight solvents) form a binary homogeneous solution, in other words, the binary solution is one-phase at the initiatory stage. The monomers can polymerize through photoinitiation[22,23] or thermal initiation.[24, 25] At some point during polymerization of the monomers, phase separation occurs as

shown in Figure 1.4, because the immiscibility in the solution increases with increasing polymer chain length.[26]

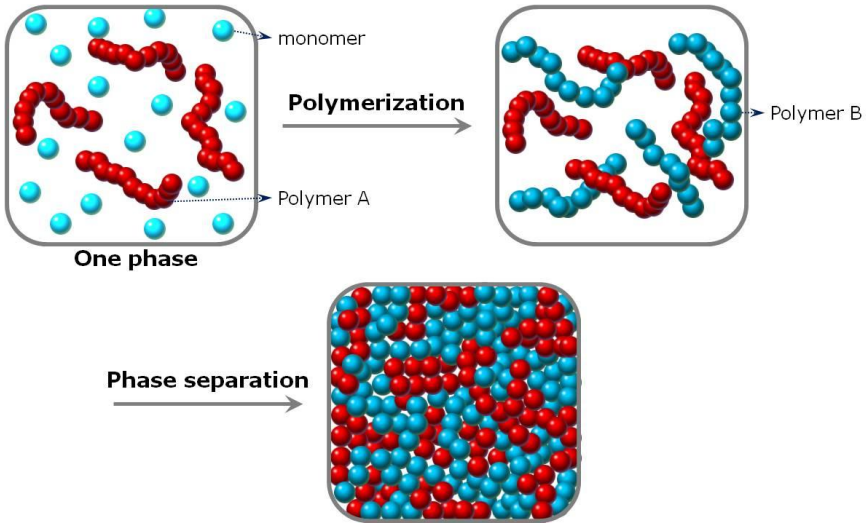

Figure 1.4. Schematic morphology of a polymer blend fabricated by the polymerization-induced phase separation.

Depending on the composition of the solution, the metastable or the unstable region will result in nucleation and growth or spinodal decomposition, respectively.[27] The PIPS occurs by the mechanism of nucleation-growth in the metastable region or spinodal decomposition in the multiphase coexisting region of the phase diagram depending on the relative rates of the phase separation and the polymerization processes.[28]

During the phase separation of the solution, polymerization can continuously produce branching through cross-linking. Ultimately, this cross-linking causes the gelation and formation of a three-dimensional network, and the viscosity of the solution at this point is infinite which prohibits molecular movement.[26] An increase of the cross-linking temperature can increase the interdiffusion rate at phase separation, but the higher cure rate also results in a faster molecular weight increase. Therefore, the higher cure rate

reduces the diffusion rate of the components of the polymer blend and it gives rise to a thermodynamically unstable polymer system.[27]

1.2 Polymer nanocomposites

Polymers have widely been used in various fields from textiles to electrical parts due to their lightweight, easy fabrication, exceptional processability, durability, and relatively low cost.[29] However, they have relatively poor mechanical, thermal, and electrical properties as compared to metals and ceramics.[30] Therefore, polymer-nanoparticle composite materials have received a lot of attention due to their synergistic and hybrid properties derived from several components.[31] In polymer matrices, these components can offer unique mechanical, electrical, optical, and thermal properties.

1.2.1 Nanoinorganic components

Polymer nanocomposites are hybrid organic-inorganic materials, in which the inorganic component is nano-scale (less than 100 nm).[32] They have received the attention of many researchers because they provide the significantly improved properties such as high modulus,[33] solvent resistance,[34] thermal stability,[35] and reduction in gas permeation[36] at low filler levels (5 wt% or lower). Since the nanosized inorganic particles have very high surface-to-volume ratios, they can provide the improved properties for the polymer nanocomposites. On the contrary, the micronsized particles cannot bring the dramatically improved properties to the more conventional composites reinforced with micronsized particles. Consequently, one important advantage of the nanoparticles in polymer composites is the extremely high surface area compared to microparticles. The extremely high surface area provides many contact sites between the

nanoparticles and the polymer matrix. Therefore, the improved properties in polymer nanocomposites come from the strong interfacial interactions between nanoparticles and the polymer matrix.[37]

1.2.2 Methods to disperse nanoparticles

Nanoparticles have a much higher ratio of surface to volume than ordinary micron-sized particels. On this account, forces between nanoparticles such as van der Waals and electrostatic forces become stronger.[38] Therefore, the nanoparticles have a strong tendency to form clusters or agglomerates to reduce their surface energy. The clusters or agglomerates are challenging to disperse individually and uniformly in the polymer matrix.[30, 39]

Generally there are three methods to disperse the inorganic nanoparticles into polymer matrices.[40] The first method is the top-down process, which consists in the direct mixing of the inorganic nanoparticles into a polymer matrix in melt or in solution. In the melt mixing, the agglomerated nanoparticles are broken down to nano-scale by the shear stress induced in a polymer melt. The inorganic nanoparticles in the polymer melt are dispersed depending largely on the shear stresses induced in the polymer melt during mixing.[41] Meanwhile, in the solution mixing, the nanoparticles are predispersed in a solution of polymer and solvent, followed by evaporation of the solvent from a solution of polymer and nanoparticles. The shear stress in a solution of polymer and nanoparticles during the solution mixing is much lower than that in a polymer melt during the melt mixing, and thus it is necessary that the nanoparticles are predispersed in a solution of polymer and solvent using an external force such as ultrasonication.[42, 43]

The second method is based on in-situ polymerization in the presence of the inorganic nanoparticles or in-situ synthesis of inorganic nanoparticles in the presence of polymer. For in-situ polymerization method, inorganic nanoparticles are dispersed in the monomer or monomer solution, and then the monomer in a mixture is polymerized.[44, 45] Therefore, a key part of in-situ polymerization is good dispersion of nanoparticles into the monomer, and this often requires the surface modification of nanoparticles to improve their wettability with the monomer.[41] On the other hand, in-situ synthesis of inorganic nanoparticles has advantages of controlling the size and morphology of the inorganic nanoparticles as well as improving the dispersion state of the inorganic nanoparticles into a polymer matrix.[46]

The last method is in-situ synthesis of the inorganic and organic components from the precursor of inorganic components and monomer of polymers. This is a method combined with in-situ formation of the inorganic nanoparticles and in-situ polymerization by using a sol-gel technique. Using this method, it is possible to disperse the inorganic nanoparticles with a dimension shorter than the molecular chain length of a polymer matrix. However, the polymer species are limited to water-soluble polymers and specific polymers with hydrogen bond acceptor groups, which are able to form hydrogen bonds with the hydroxyl groups on the surface of inorganic nanoparticles.[41] The last two methods are defined as bottom-up processes.[47] Figure 1.5 illustrates examples of the top-down and bottom-up processes for the synthesis of polymer nanocomposites.

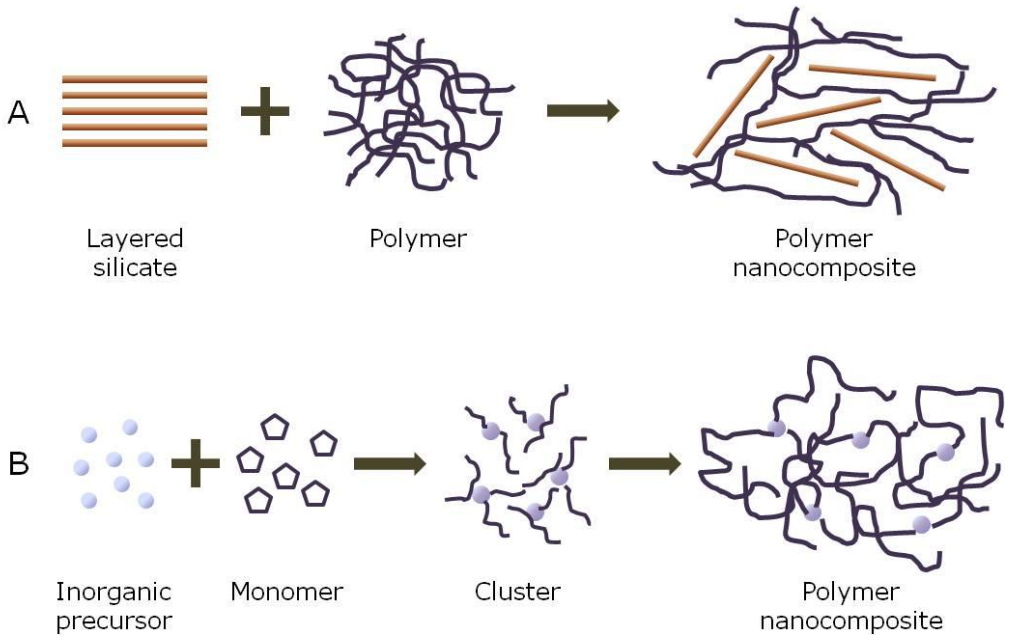

Figure 1.5. Schematic representation of A) top-down and B) bottom-up processes for the synthesis of polymer nanocomposites.

1.2.3 Properties of nanocomposite

Dimensional stability. The thermal expansion coefficients of polymers cause dimensional changes during the processing of polymers.[48] In other words, the poor dimensional stability can cause warping or other changes in shape that affect the function of polymer materials. Therefore, dimensional stability is vital in various applications of polymer materials. To reduce the coefficient of thermal expansion, fillers commonly have been dispersed into polymer matrices.

The polymer nanocomposites provide the crucial solution for improving the dimensional stability. For instance, State *et al.*[49] investigated that polymer composites based on polyurethanes and epoxy resin filled with aluminium oxide and/or tungsten powders, which were novel ultrasound backing materials with an improved thermal dimensional stability. These filler particles hinder the mobility of polymer chains, which

reduced the mechanical damping of the polymer composites, and thus it results in a decrease in the volumetric fraction of the polymer. Jamel *et al.*[35] studied the dimensional stability of polyvinyl chloride (PVC)/glass fiber foam composites to improve their properties like thermal shrinkage and heat resistance. The thermal shrinkage decreased by ~ 60%, with visible improvements to the shape distortion. This results from the glass fiber content in the PVC matrix, which has higher resistance to thermal expansion and/or contraction. In addition, this is attributed to an interlocking and bonding between the glass fiber and the foam matrix along the glass fiber length.

Mechanical properties. One of the main reasons for adding nanofillers into polymer matrices is the improvement of their mechanical properties such as the tensile strength, modulus or stiffness.[30, 50] For example, Pattanayak *et al.*[51] studied the improved mechanical properties of polyurethane (PU)/clay nanocomposites. The PU/clay nanocomposites obtained the significantly improved mechanical properties compared with neat PU when the clay particles were fully exfoliated. The PU/clay nanocomposites provided 110% improved tensile modulus, 170% improved tensile strength, 110% improved tear strength, 120% improved fracture toughness, and 40% improved abrasion resistance. These improvements in mechanical properties are originated from clay-PU tethering as well as hydrogen bonding between the clay particles and the PU matrix.

Herrera-Franco *et al.*[52] studied the mechanical behavior of continuous natural fiber reinforced high density polyethylene (HDPE), which stiffness increases by 339% compared to the stiffness of the HDPE matrix. This improvement is attributed to a change of the interaction between the surface-modified natural fiber and HDPE matrix, which is the increase of the area of contact and then improves the fiber wetting and impregnation.

Thermal conductivity. Polymers are widely used as insulating materials. However, there are many attempts to improve their thermal conductivity through the fabrication of polymer nanocomposites, which is desirable in order to the efficient dissipation of heat.[53] Polymers have a low thermal conductivity due to their relatively low atomic density, weak interactions or chemical bonding, and complex crystal structure.[54] Typical thermal conductivity values of some polymers are listed in Table 1.1. Incorporation of nanofillers including graphite,[55] carbon black,[56] carbon fibers,[57] ceramic,[58] or metal[59] particles into the polymers is a common approach to improve thermal properties.

Table 1.1. Thermal conductivity of polymers[53]

Polymer	Thermal conductivity (W/mK)
Low density polyethylene	0.28 – 0.32
High density polyethylene	0.38 – 0.58
Epoxy resin	0.17 – 0.21
Polypropylene	0.18 – 0.24
Phenol resin	0.24 – 0.29

Su *et al.*[60] reported an improved thermal conductivity of epoxy composites with hybrid boron nitride nanotubes (BNNTs) and boron nitride nanosheets (BNNSs). These composites yielded a thermal conductivity of 0.47 W/mK at 2 wt% filler loading. This improvement in thermal conductivity was due to the generation of three-dimensional thermal networks between BNNTs and BNNSs, which can provide easy paths for the heat flow through the composites.

Electrical conductivity. Electrically conductive polymer nanocomposites have been widely studied for applying in various fields such as anti-static materials,[61] electromagnetic interference (EMI) shielding,[62] chemical sensor,[63] bipolar plates for fuel cells,[64] and so on. Generally, polymers play a role as electrical insulators. Therefore, to increase the electrical conductivity of polymers, the electrically conductive polymer nanocomposites are fabricated with specific conductive additives such as metallic powder,[65] metallic fibers,[66] carbon black,[67] graphene,[68] and so on.

Chang *et al.*[69] have demonstrated an effective and simple approach to increase the electrical conductivity of poly(dimethylsiloxane)/MWCNT composites. The composite possessing 0.5 wt% of MWCNT shows an electrical conductivity jump from 2 $\times 10^{-12}$ S/cm to 4 $\times 10^{-8}$ S/cm. Guo *et al.*[70] showed an efficient and easy route to fabricate aligned CNT/polymer fibers by using acrylic acid (AA). They fabricated fabricate the CNT/polymer fibers through the introduction of monomers during in situ polymerization of AA followed by the immersion of CNT into AA. The resulting composite fibers improved their electrical conductivity compared with either the pure CNT fibers or the CNT/polymer fibers fabricated by the direct incorporation of polymers.

1.2.4 Applications

Polymer nanocomposites have been developed to meet the requirements of various applications, such as optics, electronics, mechanics, energy, environment, biology, and medicine because they can possess various properties depending on nanofillers.[71-73] Therefore, depending on the properties of nanofillers, the polymer nanocomposites have been used in membranes and separation devices, functional smart coatings, fuel and solar

cells, catalysts, sensors, military equipment, paints, automobiles, aerospace, drug carriers, and tissue engineering.[73] Some of the potential applications of polymer nanocomposites are listed in Table 1.2.

Table 1.2. Potential applications of polymer nanocomposites[71, 73]

Nanocomposites	Applications
Poly(methyl methacrylate)/SiO_2	Dental application and optical devices
Polyaniline/Fe_3O_4	Microwave absorber
High-density polyethylene/TiO_2	Bone repair
Nylon-6/Clay	Films and bottles
Nylon-6/Layered silicates	Automotive timing-belt
Poly(ethylene oxide)/Layered silicates	Airplane interiors
Polylactic acid/Layered silicates	Lithium battery development
Polyethylene terephthalate/Clay	Food packaging application
Epoxy/Montmorillonite	Materials for electronics

1.3 Anodes for sodium ion batteries

In these days, sodium ion batteries have received attention as an alternative to lithium ion batteries. Therefore, this part provides an overview of the sodium ion batteries.

1.3.1 Sodium ion battery

Lithium ion batteries are the most common type of secondary rechargeable cells because they are light weight, more compact, work at an operating voltage of ~ 4 V, and deliver with a specific energy density up to 200 Wh/kg and long lifecycle of 3000 cycles.[74, 75] Their demand is rapidly increasing because lithium is the lightest metallic element, which can provide fast diffusion kinetics into electrode materials,[76] and has a

very low redox potential ($E°_{(Li^+/Li)}$ = -3.04 V versus standard hydrogen electrode), which enables cells with high voltage and high energy density.[77, 78]

However, as lithium resources are limited natural deposits and the cost of lithium continues to increase, much research has been conducted to find the new rechargeable cells replacing the lithium ion batteries. One potential candidate of the next generation is sodium ion batteries because of more abundant and lower cost of sodium than lithium, and very suitable redox potential ($E°_{(Na^+/Na)}$ = -2.71 V versus standard hydrogen electrode).[77] Although sodium shares some properties of lithium and is inexpensive, there are some drawbacks to use sodium.

Its gravimetric capacity is lower than the capacity of lithium (1165 mAh/g compared to 3829 mAh/g).[79] In addition, the larger size of sodium ions brings the lack of suitable anode materials to host Na^+ due to a diffusion problem into anode materials compared to lithium ion. The difference between lithium and sodium is presented in Table 1.3. Therefore, in order to successfully replace lithium ion batteries by sodium ion batteries, new anode materials having a high specific capacity and low redox potential should be introduced.[80]

Table 1.3. The different characteristics between lithium and sodium[79]

Category	Lithium	Sodium
Cation radius (Å)	0.76	1.06
Atomic weight	6.9	23
Standard potential E^0 (V)	-3.04	-2.71
Capacity (mAh/g), metal	3829	1165
Cost ($/ton), carbonates	5000	150

1.3.2 Types of anodes

The chemical potential difference between two electrodes (anode and cathode) creates a voltage of batteries, and thus the battery performance characters such as specific capacity and operation voltage are determined by the electrode materials.[78] Therefore, the major challenge in sodium ion batteries is to find good electrodes.

Carbonaceous anode materials. For lithium ion batteries, graphite is used the most as anode materials. However, the sodium ion could not be successfully intercalated between the layers of graphene sheets because of its larger size (1.06 Å) than lithium ion (0.76 Å).[77] Therefore, many other non-graphitic anodes that consist largely of various carbonaceous materials have been investigated for the insertion of Na^+ ions, such as soft carbons (small regions of ordered graphen) and hard (disordered) carbons.[81]

Doeff *et al.*[81] investigated the insertion of Na ions into various carbon compounds in sodium cells. Only a small amount of Na ions is inserted into a graphite electrode (~ NaC_{70}), whereas more Na ions are inserted into petroleum coke (NaC_{30}) and Shawinigan black (NaC_{15}). Polyacrylonitrile solution was electrospun by Chen *et al.*[82] to fabricate carbon fibers, which were investigated as anode materials for sodium ion batteries. The carbon fibers exhibit a dominant adsorption/insertion sodium storage mechanism because of their small regions of ordered structure and a large interlayer spacing between graphene sheets. Therefore, they show excellent cycle stability, which is 97.7% capacity retention ratio over 200 cycles. Furthermore, the carbon fibers have reversible capacities of 233 mAh/g at a current density of 50 mA/g. However, the theoretical capacity of graphite in sodium ion cells is ~ 35 mAh/g.[83]

Metal oxide anode materials. Metal oxides are considered to be promising anode materials for sodium ion batteries because it delivers high capacities achieved compared to carbon materials.[84] Alcántara *et al.*[85] investigated that Na can induce conversion reactions of metal oxides like as Li; $n\mathrm{Li}^{+} + n\mathrm{e}^{-} + \mathrm{M}^{n+}\mathrm{X} \leftrightarrow \mathrm{Li}_n\mathrm{X} + \mathrm{M}^{0}$ (M is a metal, X is an anion, and n is the oxidation number of the metal ion in MX). The multiple electron reaction of the conversion reaction leads to high theoretical specific capacity.78

Jiang *et al.*[86] fabricated Fe_2O_3 thin films by electrostatic spray deposition that areversible capacity of 386 mAh/g at 100 mA/g is achieved over 200 cycles; as high as 233 mAh/g is sustained even cycling at a large current density of 5 A/g. This investigation indicates that the traditional conversion reactions contribute the distinguished sodium storage performance.

Wang *et al.*[87] reported on the preparation of porous CuO nanowires that are composed of nanoparticles (~50 nm) via a simple decomposition of $Cu(OH)_2$ precursor. The CuO anode displayed a discharge capacity of 640 mAh/g in the first cycle at 50 mA/g. After 50 cycles, a high capacity of 303 mAh/g obtained. This high capacity is based on the conversion reactions and the nanostructure of CuO, which can improve the Na^{+} ion intercalation kinetics (the structure of anode material will be discussed in the next section).

Intermetallic anode materials. Although carbonaceous materials have been widely investigated as anodes for sodium ion batteries because of their good cyclability, they have low capacity (less than 300 mAh/g)[88] compared to metals. Therefore, as anode materials for sodium ion batteries, pure metals such as tin (Sn), germanium (Ge), antimony (Sb), and so on have been considerably examined because their high theoretical capacities- 847 mAh/g,[89] 1625 mAh/g,[90] 664 mAh/g,[91] respectively.

For instance, Yamamoto *et al.*[92] reported that the discharge capacity of Sn thin film as an anode of a sodium ion battery was 790 mAh/g at a C/10 rate in the first cycle. Ellis *et al.*[93] also presented that the first discharge capacity of a sputtered Sn anode of a sodium ion battery was ~830 mAh/g at a C/25 rate. Abel *et al.*[94] investigated that the nanocolumnar Ge thin film had the initial discharge capacity of 430 mAh/g at a C/20 rate. For Sb as an anode of a sodium ion battery, Darwiche *et al.*[95] reported that pure micrometric Sb had the first charge capacity of 544 mAh/g at a C/2 rate. Although they bring high capacities in the first cycle, the capacities fade rapidly within few cycles. The rapid deterioration of capacities is attributed to the large volume expansion accompanied by insertion/desertion of Na^+ ions into/from the anode materials which leads to cell failure.[84]

To overcome this problem, intermetallic materials (active materials in inactive matrices) have been considered as promising anode materials for sodium ion batteries. The complex reaction mechanisms of the intermetallic materials help to relieve mechanical strain during charge/discharge.[96] Xiao *et al.*[97] investigated the SnSb nanocomposite (1 : 1 molar ratio) as an excellent example of the intermetallic anodes. The SnSb anode achieved a high capacity (544 mAh/g at 100 mA/g rate), good rate

capacity and cyclability (80% capacity retention over 50 cycles) for a sodium ion battery. The volume change of the SnSb nanocomposite is less than the individual metals which their volume change is typically ~400%.[97] Farbod *et al.*[98] provided the first report on several compositions of ternary Sn-Ge-Sb thin film alloys, which had an initial reversible specific capacity of 833 mAh/g at 85 mA/g rate and 662 mAh/g after 50 charge-discharge cycles. The ternary alloy suffers an expansion of roughly ~350%, whereas Sn has the largest volume expansion, with ~425% upon complete sodiation.

1.3.3 Importance of structure

Recently much research have been focused on the structure change of the anode resulted in an increase in electrochemical properties.[99, 100] These studies are based on how the electrochemical reactions are affected by the structures of electrodes or how the reactive sites on electrodes have increased through the control of surface area of electrode materials.[101] These anode materials have generally 2-1000 times larger surface areas compared to a planar electrode of similar size, and consist of oriented or random pore morphology. These large surface areas provide the increase of electrochemical reaction sites on the anode surface, and thus it leads to larger currents because Faradaic current generally is proportional to the electrode surface area. Furthermore, it leads to the increase of ion diffusion sites.[102] For example, Tang *et al.*[103] reported for the first time the use of hollow carbon nanospheres as sodium ion battery anode materials. The unique hollow structure can increase mass transport by offering a large surface area and a short diffusion distance.[104] The reversible capacity of the hollow carbon nanosphere anode was 200 mAh/g at a current density of 50 mA/g and a voltage range 0 - 2.5 V.

As mentioned, much research has focused on the fabrication of functional anode materials with high surface areas, which can increase the electrochemical properties of cells by facilitating better contacts between the electrolyte and electrode.[105, 106] However, other research has focused on low surface area anode materials because the first-cycle Coulombic efficiency of high surface area anodes is typically very low (less than 75%). The lower first-cycle Coulombic efficiency results from the formation of solid electrolyte interphase (SEI) layer on the large surface area materials.[107] The formation of the SEI layer causes the decrease of the full-cell capacity (SEI layer will be discussed in the next section).[108] Therefore, Luo *et al.*[108] investigated the hard carbon with low surface area (5.4 m^2/g), fabricated by doping graphene oxide into sucrose as a precursor for hard carbon. This hard carbon having low surface area remarkably enhances the first-cycle Coulombic efficiency from 74% to 83% and acquires a highly stable cyclic performance by retaining 95% of capacity after 200 cycles.

1.3.4 Solid electrolyte interphase (SEI) layer

The salts and solvents of electrolyte solutions are reduced at certain potential which is higher than the intercalation potential of ions in rechargeable batteries.[109] The decomposition of salts and solvents results in the precipitation of various species on the surface of anode materials. The formed layer by the precipitation of various species is named the solid electrolyte interphase (SEI) layer.[110]

Once formed, the SEI layer obstructs electron transport from the electrode and thus prevents further electrolyte decomposition, while still allowing ions to diffuse between the electrolyte and the electrode.[111] The SEI layer also increases a resistance,

reducing the energy density of the electrochemical cells and strongly affects the cyclability and safety of the electrochemical cells.[112]

At carbonaceous anodes for sodium ion batteries, electrochemical processes are generally considered to be dominated by two reactions: Na intercalation into carbon layers and decomposition of electrolyte. The Na intercalation represents the preferred reversible reaction, whereas the electrolyte decomposition gives rise to the irreversible consumption of Na and the degradation of a sodium ion battery.[113] The irreversible passivating layer, SEI is formed on the electrode surface due to the reductive decomposition of electrolyte during the first charge-discharge cycle.[110] The SEI layer on a typical negative electrode is diagrammatically shown in Figure 1.6.

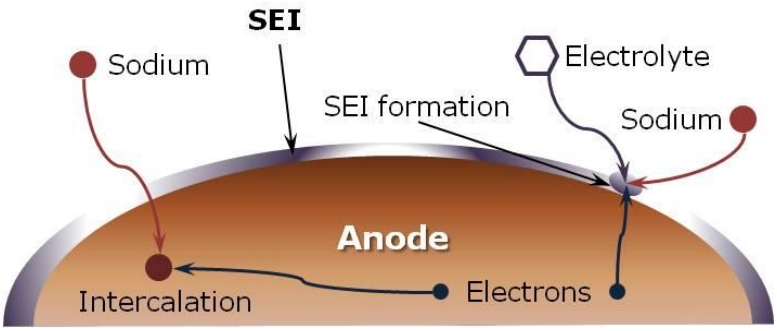

Figure 1.6. Schematic diagram of a solid electrolyte interphase (SEI) layer on an anode and its formation.

The type of anode materials affects the SEI layer and the battery performance is significantly affected by the attributes of the SEI layer such as its composition, thickness, morphology, and compactness. Therefore, a great deal of research on the SEI layer has been conducted.

Chan *et al*.[114] figured out that the volume expansion of a silicon (Si) anode during the ion insertion into the Si contributes to the dynamic nature of a SEI layer and the SEI

layer on a Si anode is dependent upon the potential. They determined that a thick SEI layer (5 μm) with large particles forms at low potentials, and then the large particles dissolve partly and crack with increasing the potential during the discharge.

Dang *et al.*[115] studied the improved electrochemical performance of nanoporous MnO frameworks with metallic Co nanoparticles as an electronic conductor and a SEI layer as a mediator for the active materials. The SEI layer plays a role as an ion conductor and a mediator of other components in the composite through the volume change during charge-discharge cycles. Therefore, they confirmed that the composites (MnO/Co/SEI) have a great property as an active material with high electron conductivity, high ion conductivity, and high durability.

Winter *et al.*[116] showed that the irreversible charge loss attributed to SEI formation is linearly proportional to the BET (Brunauer Emmett Teller) specific surface area of the carbon. Furthermore, Zheng *et al.*[117] found that the crystallographic structure and particle morphology affect the SEI layer. They showed that coke and graphite powders having same BET specific surface area exhibit different irreversible charge loss.

1.4 Dissertation overview

The broad goal of this research is to fabricate the advanced nanostructural polymer/metal oxide nanocomposites by the polymerization induced phase separation and to characterize their structure and properties (mechanical or electrochemical properties) depending on the phase and chemical composition. This dissertation is organized into 5 chapters.

Chapter 1 provides general background information about this research. Of the following three chapters, each chapter represents an independent study on the polymer/metal oxide composites fabricated by the polymerization-induced phase separation, which their mechanical and electrochemical properties are improved using Al_2O_3 and TiO_2 nanoparticles, respectively. Chapter 2 involves the mechanical property testing of poly(ethyl acrylate)/Poly(methyl methacrylate)/Al_2O_3 composites fabricated through polymerization-induced phase separation. This work in Chapter 2 is a paper to be submitted. Chapter 3 is a paper published in the ACS Applied Materials & Interfaces that focuses on fabrication of porous carbon/TiO_2 composite through polymerization-induced phase separation and use as an anode for Na-ion batteries. Chapter 4 is a paper to be submitted that includes the content of using poly(furfuryl alcohol)/poly(hydroxyethyl methacrylate) blends to tune the morphology of nanoporous carbon-titania composites for anodes of sodium ion batteries. Finally, Chapter 5 includes conclusions and the future works.

CHAPTER II

FABRICATION OF PEA/PMMA/AL_2O_3 COMPOSITE THROUGH POLYMERIZATION-INDUCED PHASE SEPARATION AND EFFECT OF ITS MORPHOLOGY ON MECHANICAL PROPERTIES

2.1 Introduction

Mechanical properties of polymer blends depend on phase-separated morphologies of the blends. The reason is that most homopolymers are immiscible, which occurs phase separation with poor mechanical properties due to low interfacial interactions.[1] The polymer blend morphologies can be divided into three categories; dispersed, stratified, and co-continuous morphologies.[2] Among the categories of morphologies, the co-continuous two-phase structure in polymer blends provides the improved mechanical properties such as high toughness, large extension, and excellent strain recovery.[3,4] Therefore, the co-continuous two-phase structure in polymer blends has attracted interest in the development of novel polymer blend materials.

One of the phase separation methods in polymer blends is polymerization-induced phase separation (PIPS). The PIPS is a process, which an initially homogeneous solution of monomer and solvent (or polymers) becomes phase separated during polymerization of the monomer. This process can be triggered either thermally or by exposure to a

radiation (visible light, UV, or electron beam) according to the needs with a proper choice of constituents including the chemical nature of initiators and monomer units.[5] In an initially homogeneous solution of monomer and other polymer(s), the molecular weight of a polymer increases with the polymerization of the monomer. Consequentially, the entropy of mixing decreases and the phase separation occurs.[6]

Meanwhile, polymer composites based on nano-sized inorganic filler particles have received much attention because such hybrid materials can possess combined properties of both the incorporated inorganic particles and polymers. The inorganic nanofillers play significant roles in modifying the desirable properties of polymer matrices and reducing the cost of their composites.[7] Indeed, the polymer/inorganic particle nanocomposite materials can be much enhanced their various properties such as mechanical,[8] electrical,[9] and optical properties,[10] and so on. Therefore, the nanocomposites have been applied to the various fields such as military equipments, automobile, aerospace, electronic equipments, optical devices, and so on.[11]

To improve such properties of polymer nanocomposites, some promising ceramic fillers such as Al_2O_3,[12] ZnO,[12] SiC,[13] TiO_2,[14] AlN,[15] and so on were studied by many research groups. Among the ceramic particles, Al_2O_3 is one of the most widely used engineering ceramic materials because the Al_2O_3 particles have excellent properties such as high elastic modulus, high wear resistance, excellent dielectric properties, high chemical corrosion resistance, high-temperature stability, good thermal conductivity, and the retention of strength at high temperatures.[16,17]

In this study, we prepared poly(ethyl acrylate) (PEA)/poly(methyl methacrylate) (PMMA)/aluminium oxide (Al_2O_3) nanocomposites by the polymerization-induced phase separation to confirm the effect of their morphologies on mechanical properties. We studied the effect of Al_2O_3 loading and PEA/PMMA/Al_2O_3 nanocomposite morphology on the mechanical properties of the nanocomposites. Accordingly, the structure of the resulting nanocomposites was examined with transmission electron microscopy (TEM), and the tensile test of the nanocomposites was examined with universal testing machine (UTM).

2.2 Experiment

Materials. Ethyl acrylate (EA, 99%, Sigma-Aldrich) and ethylene glycol dimethacrylate (EGDMA, 98%, Sigma-Aldrich) removed an inhibitor (monomethyl ether hydroquinone) by passing them through a removal column packed with alumina particles (Particle size: 50-200 μm, Alumina Basic Super I, Dynamic Adsorbents, Inc.), and then they were stored at ~5 °C prior to use. Ethylene glycol dimethacrylate was used as a crosslink agent and benzoin (98%, Sigma-Aldrich) was used as a photo-initiator. Polymethyl methacrylate (PMMA, M_w 75,000 g/mol) was purchased from Scientific Polymer Products, Inc. (Ontario, NY) and used as received. Aluminium oxide (Al_2O_3, NanoDur®AL-2420, 45 nm) was purchased from Alfa Aesar. The Al_2O_3 particles were separated from water by centrifugation (accuSpin™400, Fisher Scientific) at 7000 rpm for 5 min, and the highly concentrated Al_2O_3 slurry was re-dispersed into deionized water and EtOH using an ultrasonic cleaner (VWR® symphony™, operating frequency: 35 kHz, VWR International) to remove the surfactant dispersant and then collected again by centrifugation. This washing process was repeated 3 times.

Fabrication of PEA/PMMA/Al_2O_3 composites. In order to fabricate the PEA/PMMA blends, PMMA (0.3 and 0.7 g) was dissolved in EA (1.7 and 1.5 g). EGDMA (1 wt% related to EA) and benzoin (0.5 wt% related to EA) were dissolved into the solution of PMMA and EA. These mixtures were filled in a silicone mold, and then EA polymerization was induced by broadband UV (Spectroline, 4500 μW/cm) exposure. The polymerization was carried out at 60 ºC for 20 min. Following the guidelines provided in ASTM document D638, the silicone casting mold were designed and

fabricated with poly(dimethylsiloxane) (PDMS) base and curing agent (Sylgard 184, Dow Corning). The silicone casting mold was prepared at 10:1 w/w ratio of base to curing agent with the components physically mixed by hand. The mixture was poured onto a flat glass plate, which the 'dog-bone' shaped tensile test specimen was stuck on. The PDMS was allowed to cure and degas at room temperature for 4 h, followed by an elevated temperature cure at 120 °C for 2 h. The mold had the intagliated 'dog-bone' shapes, which dimensions are shown in Scheme 2.1.

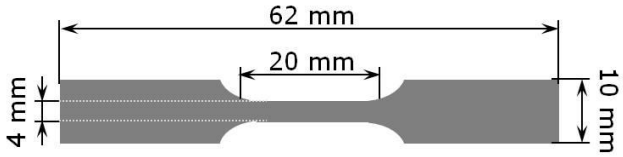

Scheme 2.1. Dimensions of a 'Dog-bone' shaped tension test specimen.

In order to fabricate the polymer nanocomposites, the different amount of Al_2O_3 (0.01, 0.03, 0.05, 0.07, 0.1, 0.15, 0.2, and 0.23 g) was ultrasonically dispersed into 1.5 g EA, and then 0.5 g PMMA, 0.015 g EGDMA, and 0.0075 g benzoin were dissolved in the solution of EA and Al_2O_3. These mixtures were filled in a silicone casting mold, and then EA polymerization was induced by broadband UV (Spectroline, 4500 μW/cm) exposure. The polymerization was carried out at 60 ºC for 20 min.

Characterization. The morphology of the nanocomposites was elucidated using transmission electron microscopy (TEM, JSM-1230, 120 kV, JEOL). Cross-sections of the composites were prepared by an ultramicrotome (PT−PC PowerTome, RMC) using a diamond knife at room temperature. The sliced specimens were approximately 70 nm thick and supported on a 3.05 mm Cu grid (01753-F, TED PELLA, Inc.) for TEM

characterization. For compositional information, the nanocomposite materials were dried overnight in a vacuum oven at 85 °C and thermogravimetric analysis was performed on TGA Q50 (TA Instrument) with a heating rate of 20 °C/min to 650 °C in air to confirm the PEA/PMMA blend and Al_2O_3 composition. The stress–strain measurements were performed on PEA/PMMA/Al_2O_3 nanocomposites. The mechanical properties of the nanocomposites were measured by universal testing machine (UTM, Instron 5567). The scan rate was 10 mm/min, and the load cell was 1 kN.

2.3 Results and discussion

Two stress-strain curves for polymer blends with different ratio of PEA to PMMA are shown in Figure 2.1. The results show that the ultimate tensile stress of specimens increases to 46 % with increase of the ratio of PMMA to EA. This is attributed to the PMMA domain, which is relatively stiff (~58 MPa of tensile strength)[18], in the rubbery PEA matrix (~0.65 MPa of tensile strength)[19]. When the ratio of PMMA to EA increases over 1:0.33 (EA:PMMA), the solution has too high viscosity to fill in a silicone casting mold. Therefore, the specimens cannot be fabricated over 1:0.33 (EA:PMMA).

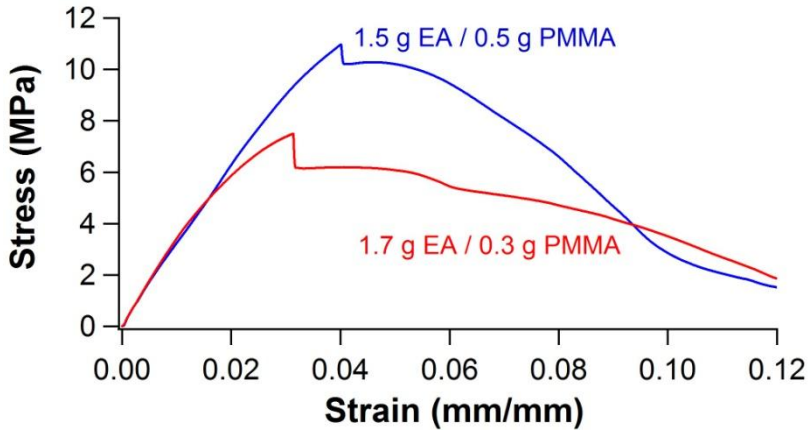

Figure 2.1. Strain-stress curves of PEA/PMMA blends fabricated using different ratio of EA to PMMA.

As a greater tensile strength is found using the 1.5 g EA/0.5 g PMMA, the ratio of PMMA to EA is fixed and the different amount of Al_2O_3 nanoparticles are loaded into the PEA/PMMA blends as the fillers to be the controlling factor for determining the morphology and mechanical properties of the nanocomposites.

TGA curves of the neat PEA/PMMA blend and the nanocomposites embedding different Al_2O_3 content are shown in Figure 2.2, and this data determine the weight

fraction of Al_2O_3 nanoparticles in the PEA/PMMA/Al_2O_3 composites. As shown in Figure 2.2, the composites have from 0.75 wt% to 15.32 wt% Al_2O_3 nanoparticles with increasing the mass of Al_2O_3 from 0.01 g to 0.23 g.

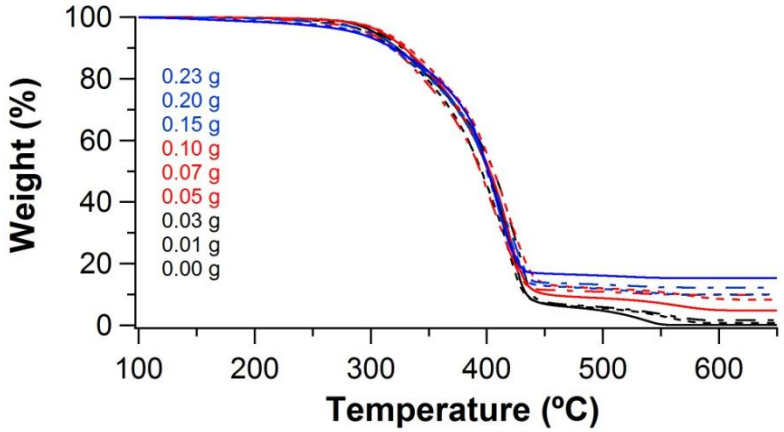

Figure 2.2. TGA curves of 1.5 g PEA/0.5 g PMMA/Al_2O_3 composites fabricated using different amount of Al_2O_3 nanoparticels to determine Al_2O_3 content by oxidation in air.

Figure 2.3 indicates the morphology change of PEA/PMMA/Al_2O_3 composites as a function of Al_2O_3 nanoparticle contents in the composites. Although it is too hard to distinguish between PEA and PMMA domains in the blend (as shown in Figure 2.3A), the TEM micrographs of the nanocomposites show that the size of clusters constituted of Al_2O_3 nanoparticles dispersed in PEA/PMMA blends increases as a function of Al_2O_3 nanoparticle contents. With randomly oriented Al_2O_3 particles at high fractions, there is not only strong interaction between particles, but also the randomness of the orientation is affected. Therefore the particles tend to stack together to forming larger clusters at high fractions.[20] The hydroxyl groups on the surface of nanoparticles lead to this agglomeration of Al_2O_3 nanoparticles through the hydrogen bonds between the surface hydroxyl groups.[21,22] The Al_2O_3 aggregates in PEA/PMMA/Al_2O_3 composites below ~5

wt% of Al_2O_3 (Figure 2.3B, C, and D) show individual domains, whereas they are interconnected above ~5 wt% of Al_2O_3 (Figure 2.3E, F, G, H, and I).

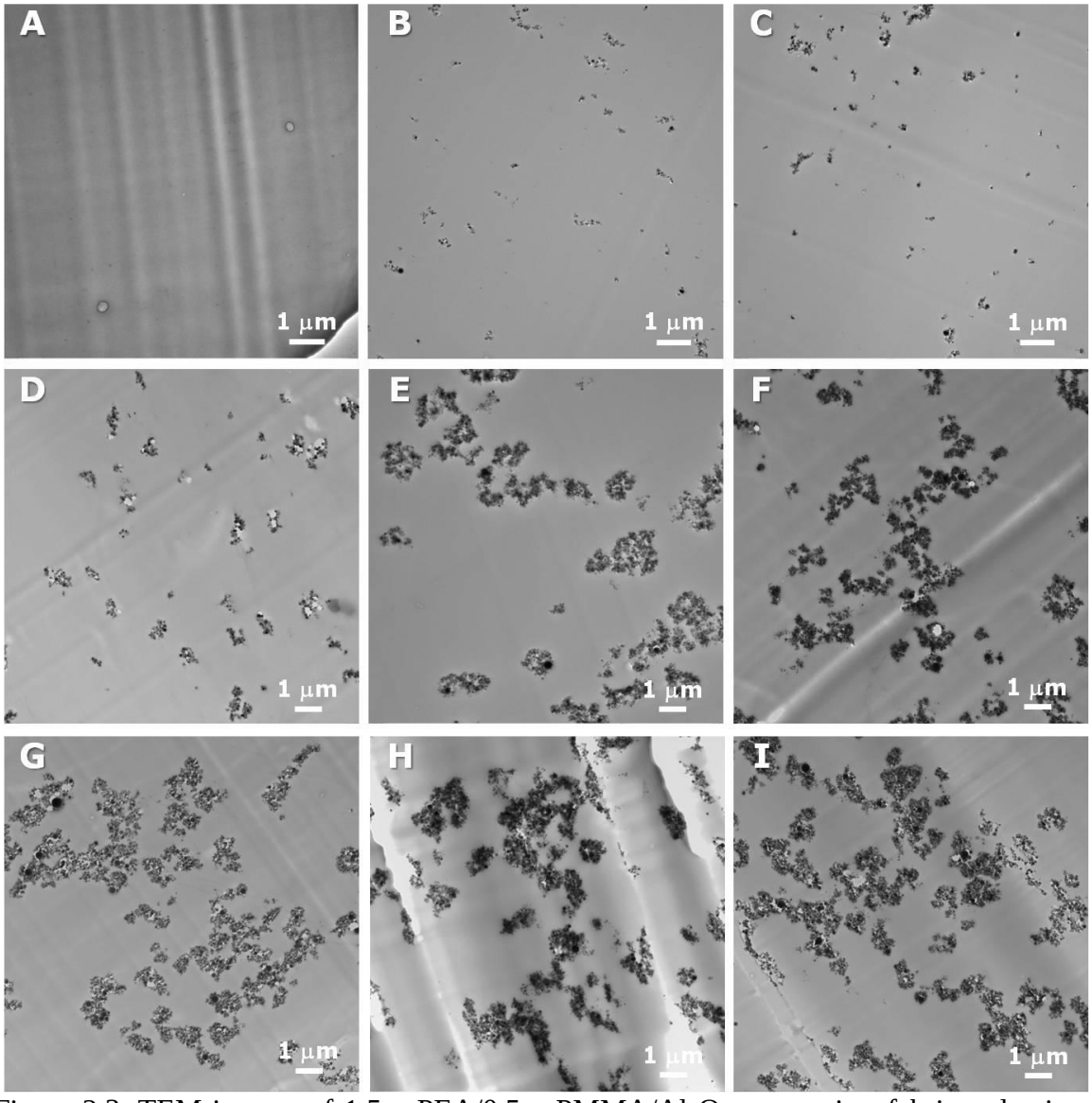

Figure 2.3. TEM images of 1.5 g PEA/0.5 g PMMA/Al_2O_3 composites fabricated using different amount of Al_2O_3 nanoparticles; (A) 0, (B) 0.75, (C) 1.65, (D) 4.87, (E) 8.35, (F) 9.92, (G) 10.03, (H) 12.27, and (I) 15.32 wt%.

To confirm mechanical properties of the PEA/PMMA/Al_2O_3 nanocomposite, tensile tests are carried out using the composite specimens as a function of Al_2O_3 concentration, 0 - 15.32% weight fraction. Figure 2.4 shows the strain-stress curves of the

nanocomposites, and the strain-stress behavior of specimens can be divided into two groups depending on Al_2O_3 concentration into the PEA/PMMA blend. The nanocomposite specimens with 0.75 - 4.87 wt% Al_2O_3 show ductile behavior, whereas other specimens with 9.92 - 15.32 wt% Al_2O_3 show quasibrittle behavior. Especially, with increasing the Al_2O_3 concentration, the ultimate tensile stress of each sample presents at lower strain. This is caused by the dispersion state of Al_2O_3 nanoparticles into PEA/PMMA blend matrix. At relatively high Al_2O_3 contents, the size of the Al_2O_3 aggregates increases with increasing Al_2O_3 contents as shown in Figure 2.3. This is due to the tendency of nanoparticles to interact with each other due to surface forces. These interact through weak van der Waals's forces creating clusters.[22] Khalid et al.[23] researched that the clusters of fillers in the matrix play a role as the failure initiation sites, which can help in the propagation of the crack or fracture.

The large Al_2O_3 clusters cause several partial failures under relatively low strain as the polymer matrix separates along Al_2O_3 clusters because the clusters act like large soft particles during the deformation process.[24] Furthermore, the nanocomposites become stiff above ~5 wt% of Al_2O_3 because Al_2O_3 clusters are interconnected, and the stress-strain relationship of the brittle samples is linear and the fracture strain is less than 4%. After the first fracture at ~3% strain, the PEA/PMMA matrix gradually separates from the Al_2O_3 particles and clusters as the strain continues to increase. Therefore, the strain-stress curves show stair-shape after ~3% strain.

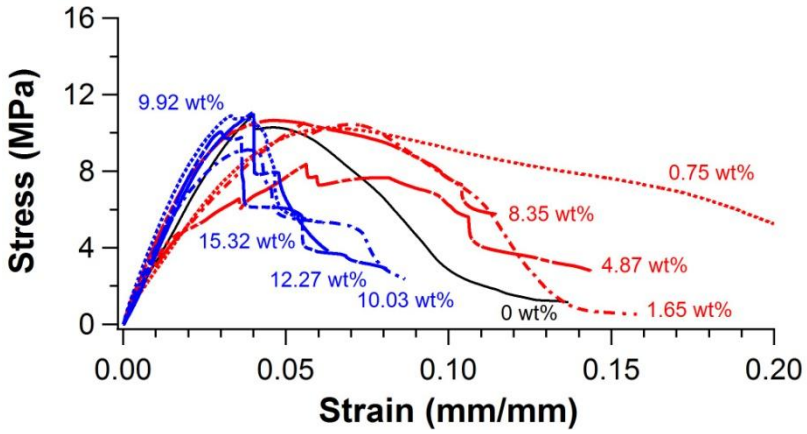

Figure 2.4. Strain-stress curves of 1.5 g PEA/0.5 g PMMA/Al_2O_3 composites as a function of Al_2O_3 nanoparticle contents in the composites.

Figure 2.5A shows the effect of Al_2O_3 content on ultimate tensile strength of PEA/PMMA/Al_2O_3 composites. It illustrates that the tensile strength of the composites decreased with increasing of Al_2O_3 content. The decrease in strength properties with increasing the Al_2O_3 content is caused both by the effective matrix (PEA/PMMA blend) cross-section reduction and stress concentration increase. In addition, a lack of interfacial adhesion between the matrix and Al_2O_3 clusters leads to the decrease of the mechanical strength.[25] The effect of Al_2O_3 loading on elongation at ultimate strength of the composites is depicted in Figure 2.5B. It shows that the elongation increases by addition of 1.65 wt% Al_2O_3 nanoparticles, whereas the elongation at over 1.65 wt% Al_2O_3 is dropped. As elongation is in inverse proportion to the stiffness of a material, the elongation results show that the Al_2O_3 nanoparticles impart a stiffening effect.[22] The elongation values at over 1.65 wt% Al_2O_3 are even smaller than the value of neat PEA/PMMA blend. The reduction in elongation at ultimate strength implies that the ductility of PEA/PMMA has been suppressed by the presence of Al_2O_3 particles. At low Al_2O_3 content (0.75 and 1.65 wt%), partial tensile strain can be transferred to Al_2O_3 embedded in PEA/PMMA matrix and the ductile PEA/PMMA matrix can stretch under

tensile stress, which leads to the increase of elongation. When the amount of Al_2O_3 particles in the matrix increases, more Al_2O_3 agglomerates form and thus more defects are introduced into the matrix. The increase of Al_2O_3 agglomerates leads to the decrease of elongation. The decrease in elongation at ultimate tensile strength comes from the fact that the deformation of the Al_2O_3 nanoparticles is generally much less than that of the polymer matrix. As a result, the polymer matrix is deformed more than the deformation of the overall composite.[26]

Young's modulus (stiffness) of the PEA/PMMA/Al_2O_3 composites can be determined from the stress-strain curves. The moduli are measured on the linear domain of the stress-strain curves. Figure 2.5C shows the variation of Young's modulus for the composites as a function of Al_2O_3 nanoparticle contents in the composites. The Young's modulus of the composites increased with the increase of Al_2O_3 nanoparticle loading by ~10 wt% of Al_2O_3. Compared to the pure PEA/PMMA blend, the Young's modulus of the 9.92 wt% filled nanocomposite sample increased to approximately 47%. This indicates that the Al_2O_3 nanoparticles are acting as reinforcement in the PEA/PMMA blend matrix. However, the decrease in Young's modulus of the composites above ~10 wt% of Al_2O_3 can be interpreted by a change in the dispersion status of Al_2O_3 nanoparticels. It is believed that filler dispersion into the polymer matrix is of great importance for improving the mechanical behavior of composites. A higher filler loading is detrimental to its uniform dispersion in the polymer matrix. Transmission electron microscopy (TEM) images in Figure 2.3 showed that the size of the dispersed phases increases with increasing Al_2O_3 nanoparticle content in the composites. The aggregates of Al_2O_3 act like large soft particles during the tensile test. The agglomerated Al_2O_3 nanoparticles create

stress concentrations in the polymer matrix and therefore decreased the Young's modulus; the poor bonding between the polymer chains and the agglomerations of Al_2O_3 nanoparticles decreases the modulus.[27]

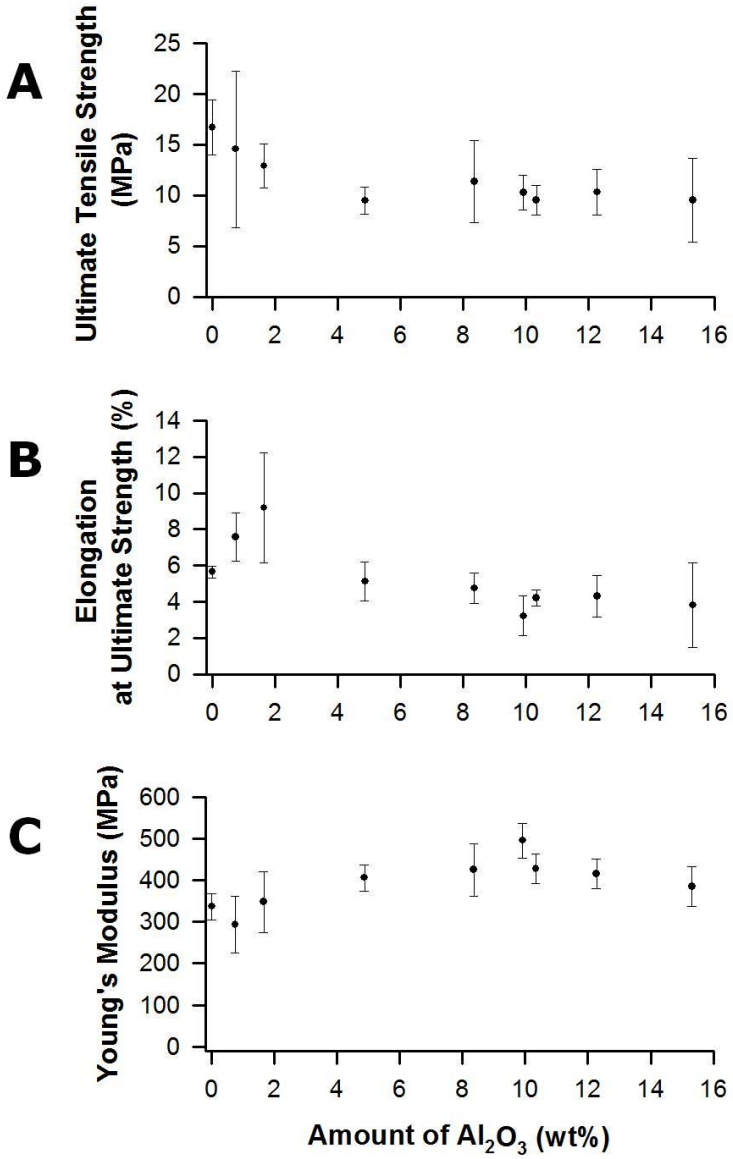

Figure 2.5. Young's modulus of 1.5 g PEA/0.5 g PMMA/Al_2O_3 composites as a function of Al_2O_3 nanoparticle contents in the composites.

2.4 Conclusions

Poly(ethyl acrylate) (PEA)/poly(methyl methacrylate) (PMMA)/aluminium oxide (Al_2O_3) nanocomposites are fabricated by the polymerization-induced phase separation to confirm the effect of their morphologies on mechanical properties. The dispersion state of Al_2O_3 in the PEA/PMMA blend matrix has a decisive effect on mechanical properties of PEA/PMMA/Al_2O_3 composite materials. With increasing of the Al_2O_3 content, the Al_2O_3 clusters become bigger and form an interconnecting network.

The small-sized clusters and individual clusters of Al_2O_3 into the composites improve the tensile strength as compared with neat PEA/PMMA blend due to interactions between the polymer chains and Al_2O_3 nanoparticles. On the other hand, the larger and interconnected clusters of Al_2O_3 bring several partial failures under relatively low strain as the polymer matrix separates along Al_2O_3 clusters because of the severe modulus mismatch between polymer and Al_2O_3 nanoparticles, and thus they cause the reduction of ductile behavior.

CHAPTER III

FABRICATION OF POROUS CARBON/TIO_2 COMPOSITES THROUGH POLYMERIZATION-INDUCED PHASE SEPARATION AND USE AS AN ANODE FOR NA-ION BATTERIES

3.1 Introduction

Batteries provide a relatively robust strategy for mobile energy storage with high energy densities for emergent green technologies.[1–4] In particular, lithium-based batteries have dominated the development landscape because of the favorable roperties of lithium: lightweight, low redox potential, and small size for ease of insertion.[5, 6] Much of the effort has focused on higher energy density devices with developments in lithium−O_2[7] and lithium−sulfur[8] batteries. However, one critical challenge for the adaptation of these technologies is cost.[9] The increasing cost of lithium and its limited natural abundance has driven interest in the development of sodiumion batteries as a low-cost alternative to its lithium analog.[10, 11] Unlike lithium, sodium is one of the most naturally abundant elements (6th most common) with a crustal concentration estimated to be 3 orders of magnitude greater than lithium. However, the potential battery performance is reduced for sodium relative to lithium.

The inferior performance of sodium can be primarily attributed to two factors: size and intrinsic mass per charge. The Na ion (1.06 Å) is about 40% larger than the Li ion (0.76 Å), which limits intercalation rate of Na and associated diffusion processes.[12] Second, the molar mass of sodium (23 g/mol) is more than 3 times that of lithium (6.9 g/mol). One key metric is the specific capacitance on a mass basis. Both Na and Li ions carry the same charge (+1), so there is a large difference in efficacy of charge storage on a mass basis between these ions. Nonetheless for some applications, namely stationary energy storage,[10] the low cost of sodium may provide sufficient advantage for adaptation.[13] One advantage for sodium-ion battery development is the similarities between sodium and lithium ions.[14] Prior work on lithium-ion batteries can provide insight into material selection for sodium-ion batteries. For example, spinel metal oxide phases that accommodate lithium insertion also tend to accommodate sodium.[15] However, the thermodynamics and, more importantly, kinetic differences between these ions can lead to unexpected differences in performance between sodium and lithium.[11]

One of the largest differences between sodium and lithium ions for batteries is the inability of sodium to intercalate in graphite, which is a common electrode for commercial lithium ion batteries.[11] Despite these challenges, several common routes to the production of high performance sodium-ion batteries have been identified. Hard carbons, unlike graphite, can intercalate sodium. The performance of sodium ion batteries with these hard carbons can be comparable to graphite in lithium analogs.[16] Significant enhancements in performance of Na-ion batteries can be obtained by use of spinel or layered metal oxides, in particular titanates.[12] The architectural design of electrodes by inclusion of doped graphene sheets for charge transport with TiO_2 nanoparticles can lead

to capacities exceeding 400 mAh/g for sodium ion batteries.[17] Similarly, defective graphene sheets can produce capacities exceeding 1000 mAh/g.[18] As an alternative to pure carbon, carbon fluorides are highly reversible and exhibit high performance (>750 mAh/g).[19] However, the use of specialty nanomaterials is counter to the low-cost motivation for sodiumion batteries. Relatively inexpensive starting materials, such as Prussian Blue,[20] can yield modest (ca. 100 mAh/g) performance electrodes. One promising low-cost material is the family of titanates.[12] However, the performance of titanium dioxide in sodium ion batteries is strongly dependent on the electrolyte,[21] the nature and size of the TiO_2,[22] the binder,[23] and the morphology associated with facilitating both ion and electron transport.[16, 17]

One additional intriguing aspect about titania is its prevalence in existing commodity products, ranging from white pigment to the active component in sunscreen. This availability should lead to low material cost, but translating commercially available powders into a usable morphology for sodium ion batteries is still a challenge due to the nanostructure requirements for high performance. For example, titanium dioxide-based battery electrodes have been fabricated by electrochemical anodization of titanium to generate nanotubes from the surface[24, 25] or direct growth of nanotubes from the current collector.[22] For TiO_2 nanoparticles, doped grapheme sheets have been demonstrated as one route to high performance through generation of porosity for Na-ion transport and improved electrical connectivity of the TiO_2 nanoparticles to the current collector.[17] This design is similar to those used for supercapacitors where the higher energy density of metal oxides is coupled with the improved electrical conductivity of carbons.[26] Recently, carbon-doped mesoporous titania has been obtained using a titanium alkoxide as the

source for both the carbon and titania,[27] which provides a benefit in terms of ease of fabrication. However, the cost of the alkoxide precursor may be problematic, similar to price considerations for the silica source for commercial zeolites.[28]

In this work, an alternative method for fabrication of porous electrode materials containing carbon and TiO_2 is proposed based on the phase separation of a filled polymer blend during polymerization. A renewable monomer, furfuryl alcohol (FA), is used as the carbon source and the initial solvent for dispersing TiO_2 nanoparticles and dissolving the polymeric porogen, poly(hydroxybutyl methacrylate, PHBMA. Acid induces polymerization of the FA to poly(furfuryl alcohol), PFA.[29] PFA produces a high yield of nongraphitizing char[30] to form the carbon matrix, whereas PHBMA fully decomposes to yield pores during carbonization. The resultant porous carbon/TiO_2 composite was tested as an anode material for sodium ion batteries. Significant improvement in performance is observed for the composite over either porous carbon or carbon-coated titania. We attribute this improvement to the hierarchical morphology developed during polymerization induced phase separation. This simple phase separation method for generating controlled porosity in carbon composites may be applied to other nanoparticle/polymer systems to generate materials for sodium-ion battery electrodes.

3.2 Experiment

Materials. Titanium(IV) tetrachloride ($TiCl_4$, Aldrich), benzyl alcohol (BzOH, anhydrous 99.8%, Aldrich), furfuryl alcohol (FA, 98%, Aldrich), diethyl ether (Anhydrous, Fisher Scientific), ethyl alcohol (EtOH, ≥ 99.5%, Aldrich), mesityl oxide (90%, Aldrich), N-methyl-2-pyrrolidone (NMP, 99.5%, Aldrich), and poly(vinylidene fluoride) (PVDF, M_n = 107 kDa, Aldrich) were used as received without further purification. Poly(hydroxybuthyl methacrylate) (PHBMA, M_w = 100 kDa) was purchased from Scientific Polymer Products, Inc. and used as received. To generate the acid catalyst, a photoacid generator, Rhodorsil PI2074, was obtained from Promerus, LLC. For battery testing, sodium perchlorate ($NaClO_4$, 98% Aldrich) dissolved in a 1:1 (w/w) mixture of ethylene carbonate (EC, 99%, Aldrich) and propylene carbonate (PC, 99.7%, Aldrich) was used as the electrolyte. Na metal (99.8%, Acros Organics) was used as the counter electrode and copper foil (0.025 mm thick, Puratronic) was used as a current collector of the anode electrode in the coin cells.

Synthesis of TiO_2. TiO_2 nanoparticles were synthesized by alkyl halide elimination.[31] Ethanol was added as a cosolvent for the $TiCl_4$ to decrease the violence of the reaction and improve control of particle formation.[32] In a typical synthesis, 6 mL of $TiCl_4$ was slowly injected into 16 mL of EtOH. Under vigorous stirring, the ethanoic $TiCl_4$ solution was subsequently slowly injected into 50 mL of BzOH that was preheated to 80 °C in a 250 mL round-bottom flash and allowed to react for 8 h at 80 °C under continuous stirring. The synthesized nanoparticles were separated by precipitation by addition of 30 mL of the reaction solution to 300 mL of cold diethyl ether (9 °C) and subsequent centrifugation (accuSpin400, Fisher Scientific) at 7000 rpm for 5 min. The

precipitate was redispersed into deionized water and EtOH using an ultrasonic cleaner (VWR symphony, operating frequency: 35 kHz, VWR International) to remove residual precursors and then collected again by centrifugation. This washing process was repeated 5 times.

Surface Modification of TiO_2. The strong acidic surface of the assynthesized TiO_2 nanoparticles acts as a catalyst for the polymerization of FA. In order improve control of the polymerization, a poly(furfuryl alcohol), PFA, shell was fabricated around the TiO_2 nanoparticles prior to production of the composite. In a typical synthesis, 1 g of TiO_2 was dispersed in a solution of mesityl oxide (20 mL) and FA (0.5 mL), and the suspension was stirred at 60 °C for 6 h. FA was polymerized on the surface of TiO_2 and then the PFA-coated TiO_2 was collected by centrifugation at 7000 rpm for 5 min.

Fabrication of PHBMA/PFA/TiO_2 Composites. To fabricate composites, we dissolved 0.35 g of PHBMA in a mixture of 0.3 g of FA and 0.2 g of EtOH; 0.3 g of PFA-coated TiO_2 was ultrasonically dispersed in 0.3 g of EtOH and 1.5 mg of Rhodorsil PI2074 was dissolved in this solution. This dispersion was mixed with the polymer solution and cast into a PTFE Petri dish. FA polymerization was induced by broadband UV (Spectroline, 4500 μW/cm) exposure. The polymerization of FA was allowed to proceed at 60 °C for 10 min. After the polymerization, the composite was pyrolyzed at 900 °C under a N_2 atmosphere with controlled heating steps of 1 °C/min to 650 °C, held at 650 °C for 3 h, 1 °C/min to 900 °C, and held at 900 °C for 1 h. The temperature was then cooled at 3 °C/min to room temperature.

Characterization. Fourier-transform infrared spectroscopy (FTIR, Nicolet iS50, Thermo Scientific) was used to characterize the chemistry of the TiO_2 nanoparticles and the composite powders using diffuse reflection (Praying Mantis DRP accessory), 512 scans, and a deuterated L-alanine doped triglycine sulfate (DLaTGS) detector. The chemical composition of the composites was also assessed with X-ray photoelectron spectroscopy (XPS, PHI 5000 Versa probe II scanning XPS microprobe, ULVAC-PHI Inc.). The scans were recorded at a takeoff angle of 45°, probing approximately 10 nm into the surface of the thin films. The morphology of the samples was elucidated using transmission electron microscopy (TEM, JSM-1230, 120 kV, JEOL). Cross-sections of the composites embedded in epoxy resin (Embed-812 Resin, Electron Microscopy Sciences) that was hardened at 60 °C for 12 h were prepared by an ultramicrotome (PT−PC PowerTome, RMC) using a diamond knife at room temperature. The sliced specimens were approximately 70 nm thick and supported on a 3.05 mm Cu grid (01753-F, TED PELLA, Inc.) for TEM characterization. To determine the size of pristine and PFA-coated TiO_2 particles, the TEM micrographs were analyzed in ImageJ. The area of these PFA-coated TiO_2 particles was used to calculate an effective diameter with 20 particles examined to obtain statistics. For compositional information, the composite materials were dried overnight in a vacuum oven at 85 °C and thermogravimetric analysis was performed on TGA Q50 (TA Instrument) with a heating rate of 20 °C/min to 700 °C in air to confirm the carbon and TiO_2 composition. Nitrogen adsorption/desorption isotherms were obtained at 77 K using a Micromeritics TriStar II instrument. The specific surface area of samples was calculated by the Brunauer−Emmett−Teller (BET) method[33]

and the pore size distribution was determined from the adsorption isotherm using the Barrett−Joyner−Halenda (BJH) method.[34]

Battery Fabrication and Testing. The carbonized materials were ground by mortar and pestle into a powder. The carbon/TiO_2 composite, carbon black (N330, Sid Richardson Co.), and PVDF (binder) were mixed with a small amount of NMP to form concentrated slurry at 85:5:10 (w/w/w) ratio for the solids. Electrodes based on neat carbon (obtained without the addition of TiO_2 nanoparticles) and carbon-coated TiO_2 were also prepared with the same methodology as controls. The slurry was coated onto copper foil using a Mayer rod (RDS 22) and the coated foil was dried overnight under vacuum at 80 °C. The dried coating on foil was punched to 13 mm (diameter) for the battery anode; a representative anode contained approximately 1.5 mg of active material. CR2032 coin cells (MTI Corporation) were assembled in an Ar-filled glovebox (O_2 < 0.5 ppm, H_2O < 0.5 ppm) using the composite as the anode electrode, Na metal as the cathode electrode, Celgard 3501 (Celgard, LLC.) as the separator, and 1 M solution of NaClO4 in EC and PC (1:1 v/v) as the electrolyte.

For testing the performance of the coin cells, galvanostatic charge and discharge experiments were performed with a battery tester (BST8-WA, MTI) at current densities between 21 and 440 mA/g. Two different half-cell potential windows were examined, 0.01−2.00 V and 0.01−3.00 V vs Na/Na^+, for the operation of the battery as both have been used previously for TiO_2 based anodes for Na-ion batteries.[17, 21, 35, 36] Electrochemical impedance spectroscopy (EIS) analysis was conducted using an electrochemical workstation CHI660D (CH Instruments) with an applied amplitude of 5 mV in the range of 100 kHz to 0.001 Hz after operating the electrodes for 70 cycles.

3.3 Results and discussion

Figure 3.1 illustrates schematically the methodology associated with the production of the composite. First, the surface of the TiO_2 nanoparticles is capped (see Figure 3.2) by exposure to dilute FA. The acidic surface of the as-synthesized TiO_2 induces polymerization of FA, even after the particles are rinsed with deionized water and EtOH several times. Without passivation of the TiO_2, this polymerization leads to loss of control of the morphology of the composite. After this surface modification of the TiO_2, the three primary components (PHBMA, FA, and TiO_2) plus the photoacid generator are dispersed in solution. With the PFA-coated TiO_2 nanoparticles, the mixture is stable until exposure to UV light. The PAG then produces a strong acid that induces polymerization of the FA. The increasing molecular weight of (P)FA on polymerization drives the phase separation of PFA and PHBMA, but TiO_2 nanoparticles may limit the size scale because of the inherent surfactancy of nanoparticles.[37, 38] Unlike bijels,[37] this morphology is kinetically trapped by the decreasing mobility of the system as the FA polymerizes.

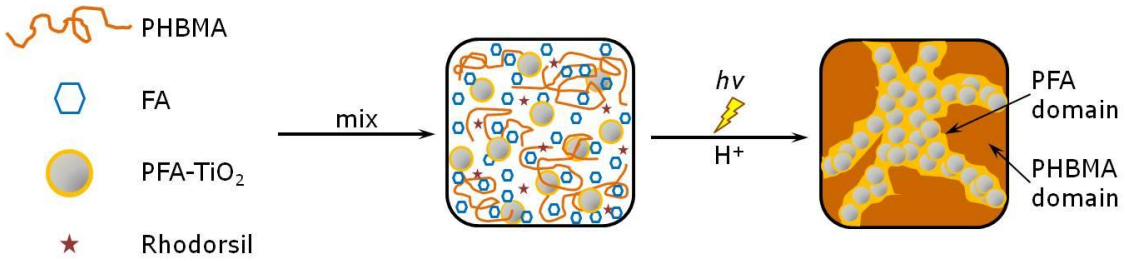

Figure 3.1. Schematic illustration of morphology developed during the polymerization of FA after dispersing PFA coated-TiO_2 nanoparticles and PHBMA in FA. Exposure to light triggers the condensation of FA by generation of acid.

FT-IR has been employed to investigate the surface modification of TiO_2 nanoparticles by the PFA coating. As shown in Figure 3.2, the spectra for all samples show one broad band near 3600 cm^{-1} and a peak near 1100 cm^{-1} (black dotted boxes)

which corresponds to surface-adsorbed water and hydroxyl groups and surface vibrations of the Ti–O bonds, respectively.[39] For PFA-coated TiO_2, the absorption band at 2925 cm^{-1} responding to $–CH_2$ group between furan rings, 1025 and 1080 cm^{-1} responding to the =C–O–C= group of furan ring, 1570 and 1510 cm^{-1} responding to –C=C– of furan ring, and at the same time, a new absorption peak appears at 1700 cm^{-1} due to the –C=C– group in aromatic rings.[40] These characteristic peaks indicate the modification of TiO_2 is performed successfully.

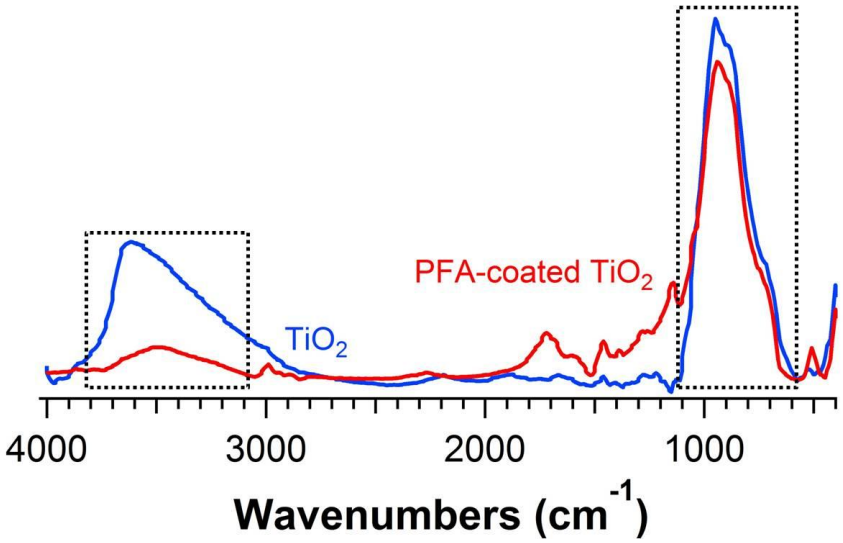

Figure 3.2. FT-IR spectra of as-synthesized (blue line) and PFA-coated TiO_2 (red line) nanoparticles.

Figure 3.3 illustrates the structure of these materials from the nanoparticles to the final porous carbon/TiO_2 composite material after pyrolysis. Figures 3.3A illustrates the as-synthesized anatase TiO_2 nanoparticles, which have a mean diameter of 40 ± 7 nm. The crystalline nature of these TiO_2 nanoparticles can be observed with high resolution TEM (see Figure 3.4). The exposure of these nanoparticles to dilute FA generates a shell of PFA around the TiO_2 particles that approximately doubles the particle size to 98 ± 30 nm (Figure 3.3B). Although a single TiO_2 nanoparticle in each composite particle is most common, particles containing two or three TiO_2 nanoparticles are also observed. Additional examples of these coated particles are shown in Figure 3.5. As shown in Figure 3.1, these coated nanoparticles are mixed with the PHBMA in FA. After polymerization of the FA, one polymer domain contains a majority of the TiO_2 as shown in Figure 3.3C. This morphology is consistent with the expected phase separation of components. There is sufficient electron contrast between PHBMA (low electron density, light regions), PFA (higher electron density, dark gray region) and TiO_2 nanoparticles (highest electron density, dark regions) to demonstrate that the TiO_2 particles are located in only PFA domain as expected on the basis of their surface chemistry. This structure can be transformed into a porous carbon composite through pyrolysis as shown in Figures 3.3D; this composite has a broad distribution of nanopores formed by the thermal decomposition of PHBMA, whereas the anatase nanoparticles are embedded in the carbon matrix. The role of these components can be confirmed by examining the binary mixtures of nanoparticles and FA or FA and PHBMA. Without PHBMA, the material does not contain large nanopores. Without the nanoparticle, large pores are still formed, which confirms the role of the PHBMA as the porogen.

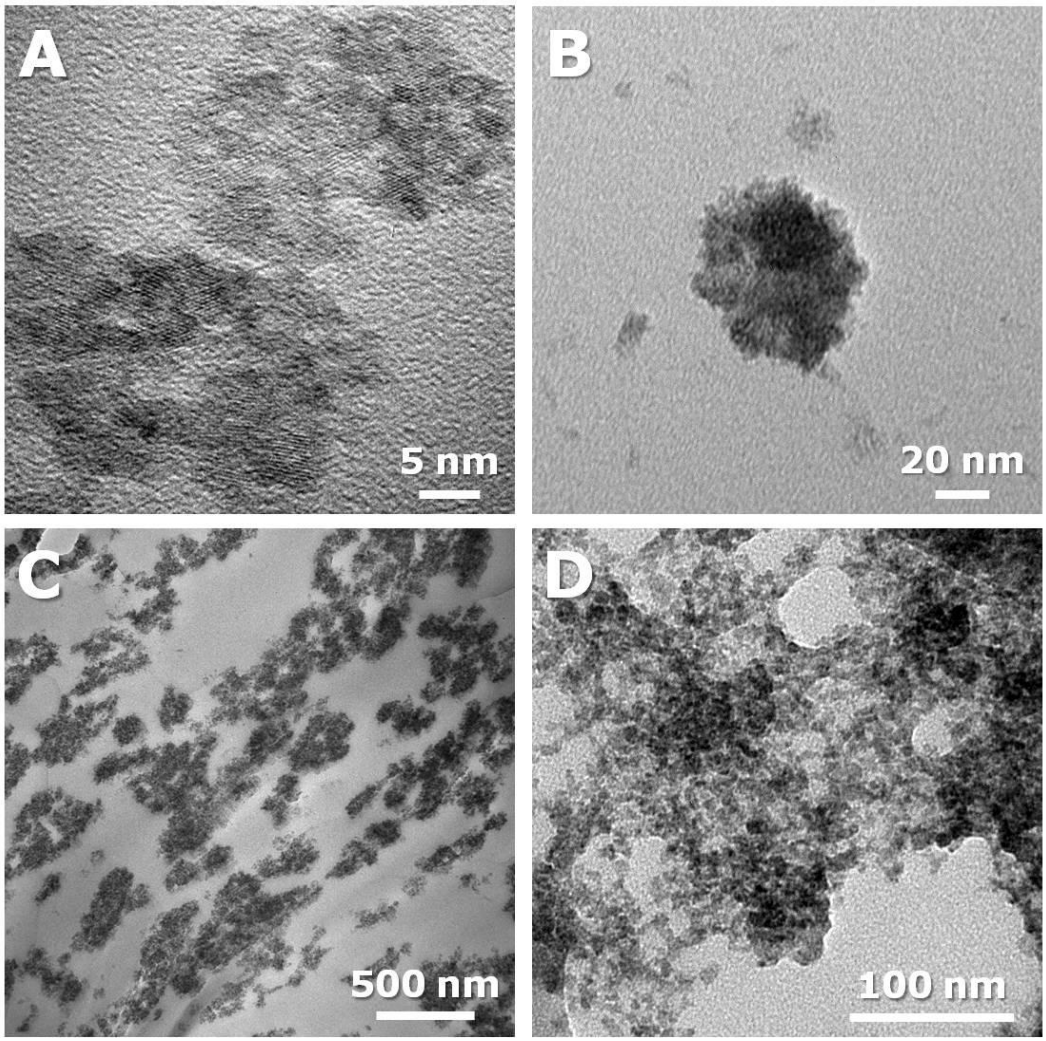

Figure 3.3. TEM images of (A) as-synthesized TiO_2 particles, (B) PFA-coated TiO_2 particles, and the cross-section specimens of (C) PHBMA/PFA polymer blend embedding PFA-coated TiO_2 and (D) the carbon/TiO_2 composite.

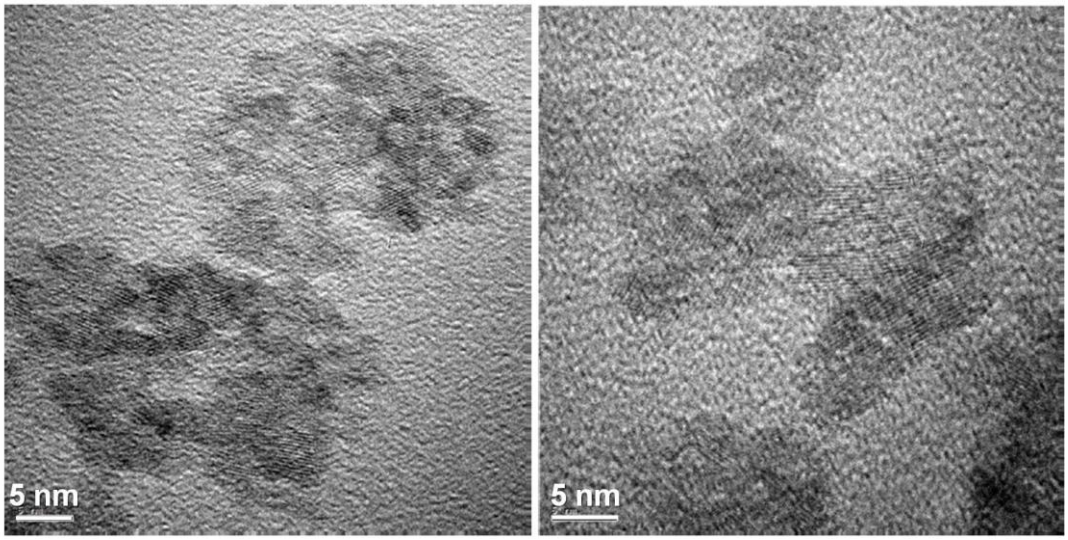

Figure 3.4. High resolution TEM micrographs of the as-synthesized nanoparticles. The crystalline nature of these nanoparticles can be assessed by the lattice fringes present.

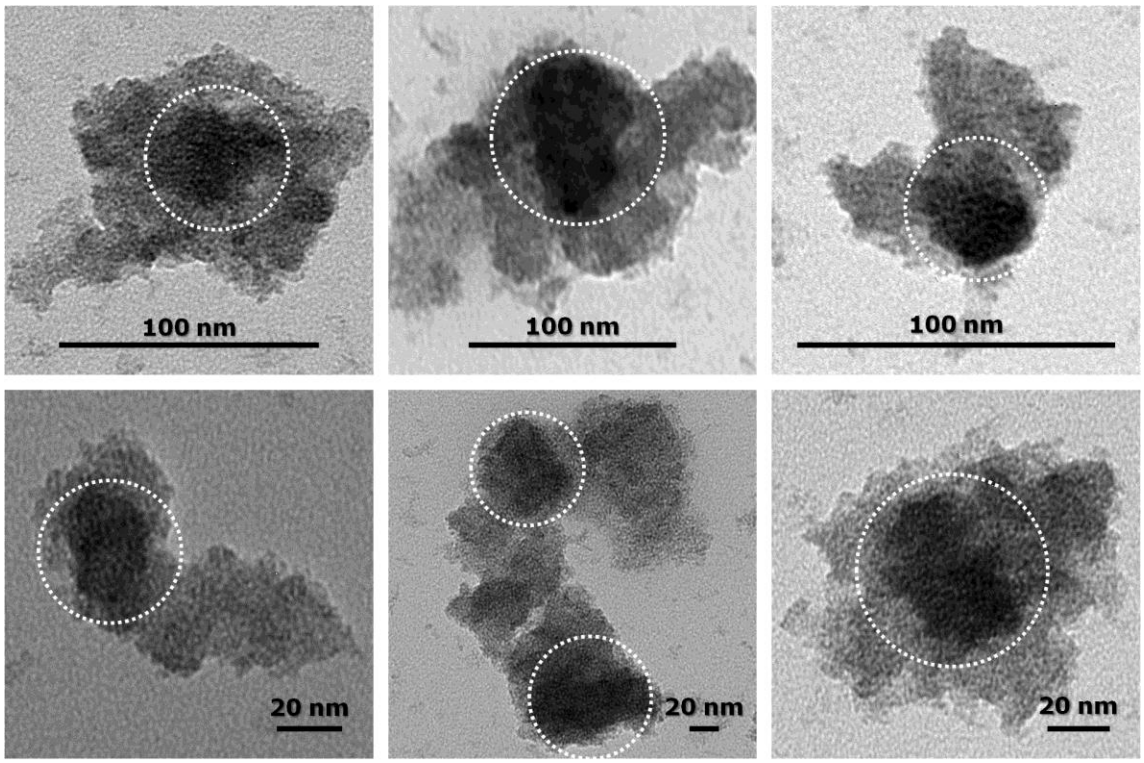

Figure 3.5. TEM images of the PFA-coated TiO_2 particles; the mean size of TiO_2 particles (white dashed-line circle) is approximately 40 ± 7 nm, and the PFA shell forms around TiO_2 particles to almost double size.

Figure 3.6 demonstrates that the carbonized composite still contains anatase TiO_2 nanoparticles from XRD with strong diffraction peaks at 25° and 48°. These peaks are in good agreement with the standard spectrum for anatase (JCPDS no.: 84−1286).[41] From TGA measurements (see Figure 3.7) in air, these composites contain 55 wt % titania. In comparison to many previous reports for hierarchical metal oxide-carbon composites for battery electrodes, the carbon content is high (ca. 45 wt%) as 15−30% carbon is typical.[42−44] As little as 3% carbon has been reported,[45] but similarly composites with 50−50 metal oxide-carbon have exhibited good performance as electrodes.[46, 47] One challenge associated with design of electrode materials is that the performance is driven by a plethora of both physical and chemical variables.

In addition to the chemical composition, the porous nature of the carbon composite is a key attribute. In comparing the BET sorption isotherms between the carbon coated TiO_2 nanoparticle and the composite obtained on polymerization induced phase separation (Figure 3.6B), there are several distinct features that demonstrate the difference in the morphology. First at low pressures, the sorbed volume is significantly greater for the composite. The BET surface area is 215 m^2/g (Figure 3.6B) for the carbon composite, whereas only 36.6 m^2/g for the carbon-coated TiO_2. This surface area is slightly larger than hierarchically templated composite electrodes with both macroand meso-pores (3DOM/m).[42] Second, the hysteresis loop at higher pressures associated with the emptying of the mesopores is not well-defined for the composite. As the hysteresis is associated with the “ink-bottle” effect[48] associated with connecting pores limiting the desorption, transport in the pores of the composite should be less hindered.

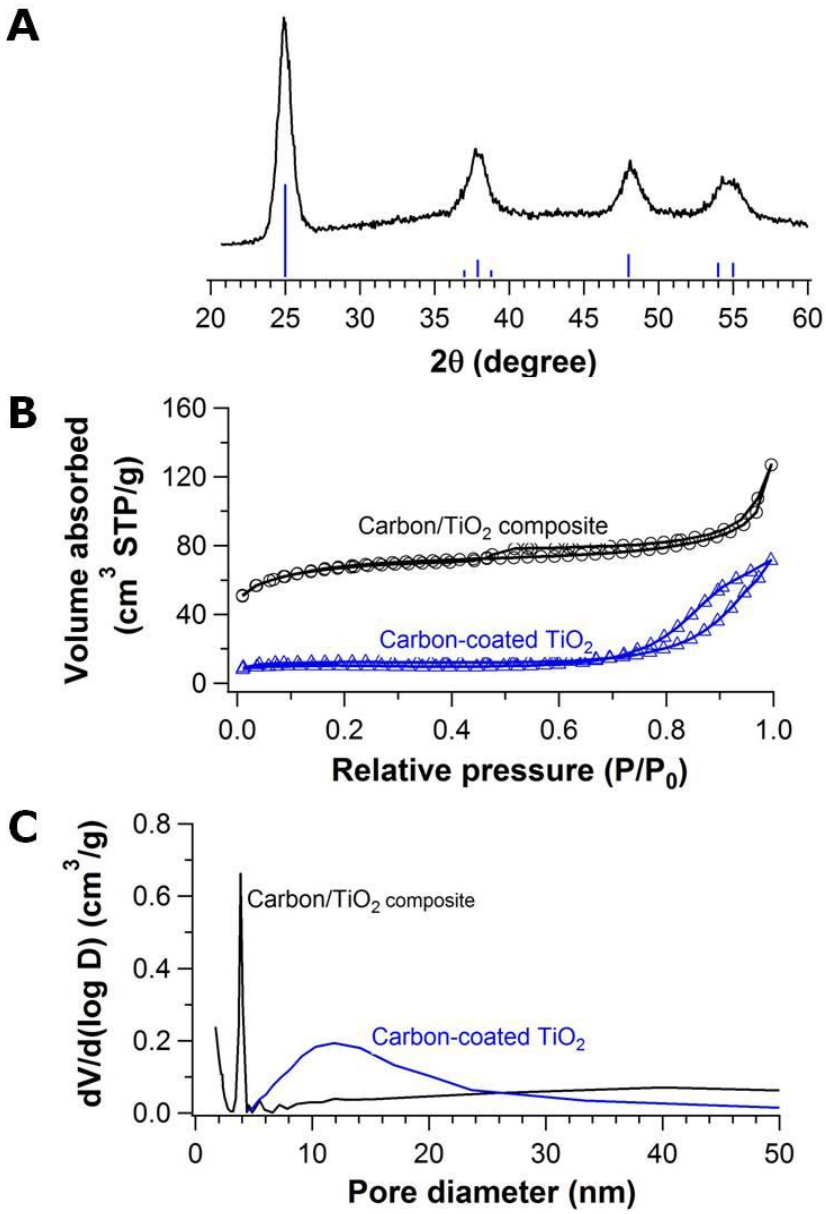

Figure 3.6. (A) XRD profile for the carbon/TiO_2 composite produced by carbonization of PHBMA/PFA polymer blend with embedded PFA-coated TiO_2 and the standard spectrum of anatase TiO_2 (JCPDS 84−1286, blue lines). (B) N_2 adsorption and desorption isotherms of this porous carbon/TiO_2 composite and the material formed by the carbon-coated TiO_2. (C) Pore size distributions for the two materials determined from the adsorption isotherms.

Figure 3.6C illustrates the pore size distribution calculated from the adsorption data. The hierarchical structure of the carbon composites derived from the polymerization induced phase separation is clearly shown with micropores, small (ca. 4 nm) mesopores, and a broad distribution of mesopores that extend into the macropore regime. This pore structure could provide a route for high-performance electrodes because of their relatively high surface area and lack of significant bottlenecks in the pore structure for the transport of ions.

To understand the impact of the hierarchical structure on the battery performance, we compared galvanostatic charge/discharge behavior of the carbon/TiO_2 composite to that of both porous carbon obtained from the polymerization of FA without the TiO_2 nanoparticles and carbon-coated TiO_2 without the additional FA and PHBMA. One significant difference is the carbon content between the carbon-coated TiO_2 (4 wt %) and the porous carbon/TiO_2 composite (45 wt %) as determined by TGA (see Figure 3.7).

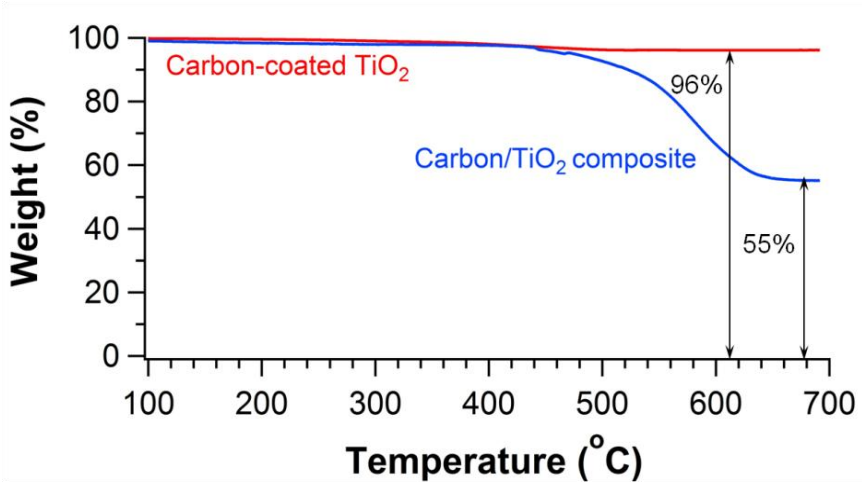

Figure 3.7. TGA curves to determine the carbon content by oxidation in air.

The general embedding of the TiO_2 nanoparticles within the carbon matrix is confirmed by XPS analysis of these two materials, which indicate larger carbon content on the surface (see Figure 3.8). As shown in Figure 3.9A, the porous carbon/TiO_2 composite anode produces nearly three times the storage capacity compared to the neat carbon and carbon-coated TiO_2 anodes. The small carbon content of the coated TiO_2 (4 wt %) should be sufficient for providing conductivity as only 3 wt % carbon previously was shown to be effective for battery electrodes,[45] so this poor performance is likely not attributable to poor electrical conductivity. This result indicates that the hierarchical porous structure of the carbonized PHBMA/PFA/TiO_2 blend and associated large surface area is likely responsible for the higher capacity of this anode material. The capacitance is relatively stable over the first 10 cycles for all three materials examined. For the composite electrode, the capacity was determined to be approximately 150 mAh/g at a rate of approximately 0.13 C. This capacity is similar to that obtained for hollow titania nanotubes,[22] but without the need to synthesize this specialty nanomaterial.

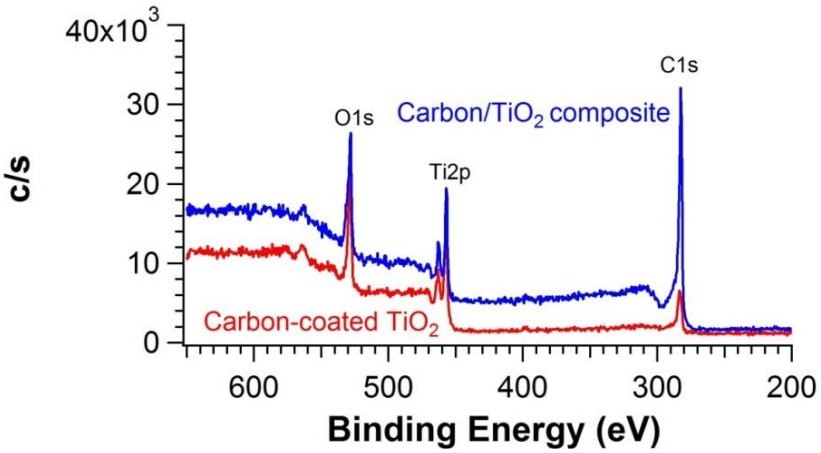

Figure 3.8. XPS spectra of carbon-coated TiO_2 and carbon/TiO_2 composite.

One potential route to increase the capacity is increasing the potential range for the cell. Previous work examining carbon and TiO_2 materials for Na ion batteries used half cells in ranges of either 0.01−2.0 V[21, 35] or 0.01−3.0 V[17, 36] vs Na/Na^+. Increasing the potential window provides the potential for energy gains, but also for parasitic faradaic reactions at the electrode to the detriment of performance. Figure 3.9B and 3.9C illustrate the difference in the typical Galvanostatic charge−discharge profiles of the carbon/TiO_2 composite for these two potential ranges at a current density of 21 mA/g (approximately 0.13 C). In both cases, there is a decrease in capacity after the first cycle, which is attributed to the side reactions of electrolyte and the formation of solid electrolyte interphase (SEI).[49]

On the basis of calculations, insertion of Na into TiO_2 at potentials greater than 2.5 V should not be reversible,[50] but high-capacity and high-rate sodium-ion batteries based on titania have been reported using a higher potential (3 V).[36] To investigate this behavior, we can examine the time dependence of the potential during charge and discharge: smooth increase and decrease in potential is found for the 0.01−2.0 V potential window, but there is a shoulder in the charging curve when using 0.01−3.0 V (see Figure 3.10). The nonideal behavior in these electrodes occurs at approximately 2.4 V, which agrees with the theoretical limit.[50] Interestingly, after 10 cycles, the discharge capacity is still enhanced for the larger potential range by nearly 15% (180 mAh/g and 156 mAh/g). This suggests that the enhanced capacity may originate from better wetted electrodes at high potential. Sodium-ion insertion into the nanopores does not appear to be a major charge storage mechanism with these materials, as no clear voltage plateau exists.[51]

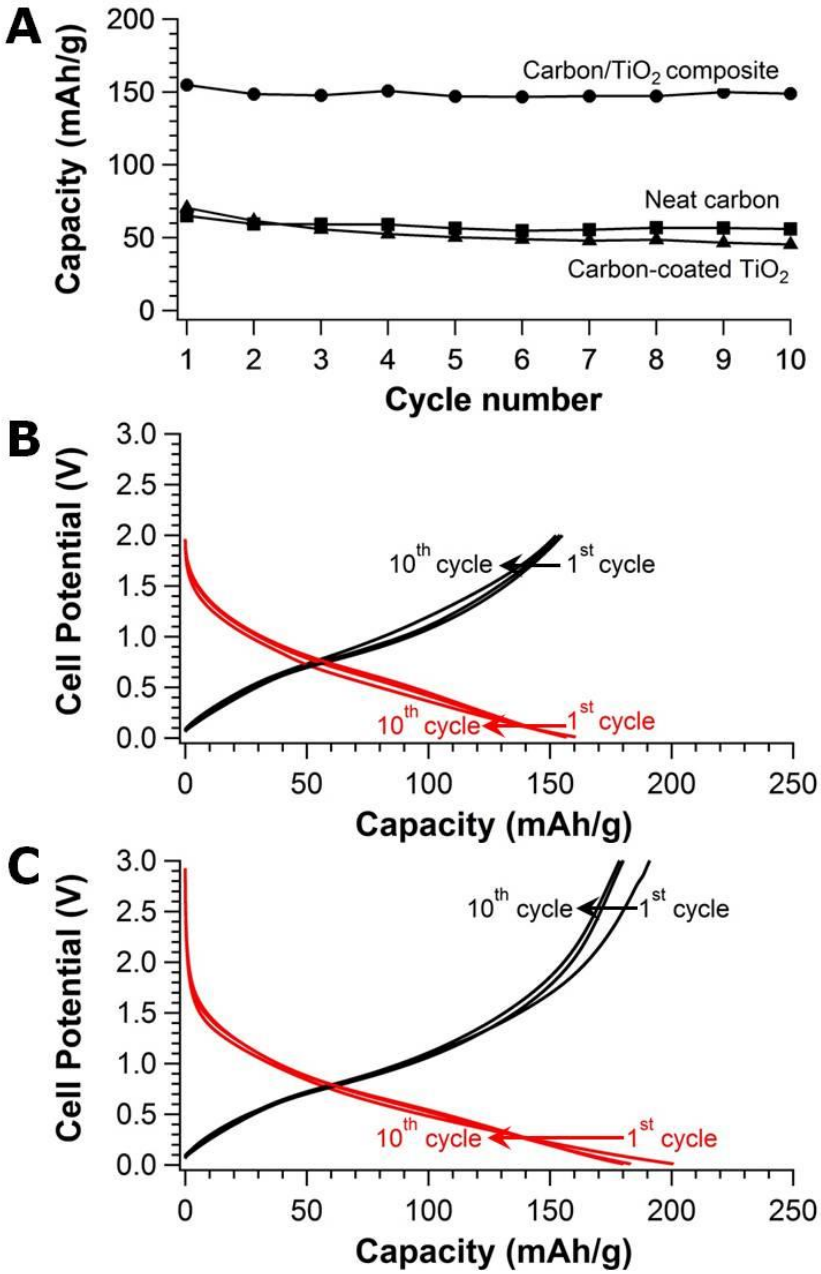

Figure 3.9. (A) Discharge capacity changes of neat carbon, carboncoated TiO_2, and carbon/TiO_2 composite during 10 cycles of galvanostatic charge−discharge behavior with a potential window of 0.01−2.0 V at a current density of 21 mA/g, and galvanostatic charge (black line)−discharge (red line) profiles of carbon/TiO_2 composite for selected cycles (1st, 5th, and 10th) with different potential ranges at a current density of 21 mA/g; (B) 0.01 to 2.0 V and (C) 0.01 to 3.0 V.

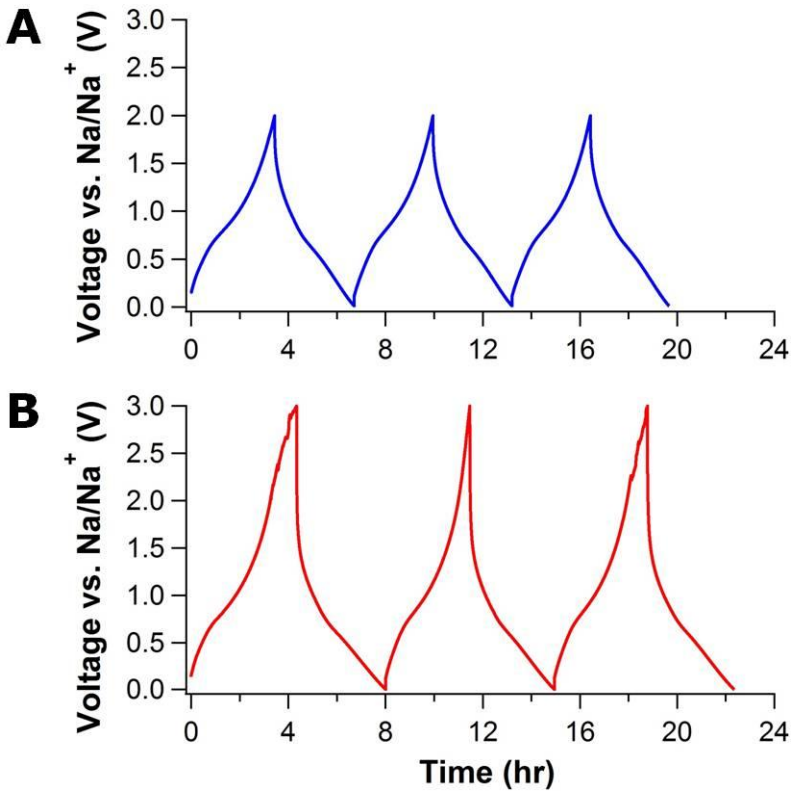

Figure 3.10. Galvanostatic charge/discharge behaviors of carbon/TiO_2 composites in different potential ranges of 0.01–2.0 V (A) and 0.01–3.0 V (B) at a current density of 42 mA/g.

To further investigate the capacitive stability and reproducibility of these composite electrodes, we fabricated and tested new electrodes at the current density of 42 mA/g (approximately 0.28 C) for 50 cycles (Figure 3.11A). The specific capacity is remains stable after 50 cycles, which indicates sodium ion uptake and release is highly reversible. The initial capacities are 155 and 133 mAh/g for 0.01−3 V and 0.01−2 V, respectively. These values are reduced from the prior electrodes, but this is expected as the current density is doubled. This difference in capacity is not due to reproducibility issues as will be discussed later. The high reversibility (>90%) of these composite materials and the limited decrease in capacity with increasing rate lend itself to examining the performance limits for these composite materials.

Figure 3.11B illustrates the impact of charge−discharge rate on the capacity of the carbon/TiO_2 composite anode. Increasing the current density from 21 mA/g (about 0.13 C) up to 440 mA/g (about 3.8 C) decreases the capacity of the material from 173 mAh/g to 68 mAh/g (for 0.01 to 3 V). With 10 cycles at each current density, it is clear that the reversible capacity is stable for both potential windows examined for current density ≤220 mA/g. Noticeable capacitance fade occurs at higher current densities. At 440 mA/g, the capacity for the two cells is indistinguishable despite the difference in the potential windows (see Figure 3.12). The capacity for the 0.01 to 3 V potential window fades faster than it does for the 0.01 to 2 V potential window at elevated current densities due to irreversible Na^+ insertion at potentials greater than 2.5 V. These data demonstrate that these composite materials are effective electrodes for sodium ion batteries even operating at high rates (~5 C).

The specific capacity of these composites (120 mAh/g at 110 mA/g using cutoff voltage between 0.01 and 2.0 V vs Na/Na^+) is 20% greater than that reported for TiO_2 nanocrystals intermixed with carbon (100 mAh/g at 100 mA/g using cutoff voltage between 0.01 and 2.5 V vs Na/Na^+).[52] Additionally, the high rate performance is typically hindered by the insertion and extraction of the large Na ions (1.02 Å) into the host structure.[36] Hard carbons exhibit high capacity (300 mAh/g) at low rate (0.1 C), but the capacity significantly drops by almost one-third at 2 C.[53] For the composite examined here, the capacity did not decrease by one-third until almost 5 C. Moreover, the Coulombic efficiency remains over 95% at all current densities and potential windows examined for the composites (Figure 3.11B). One final note is the recovery of the capacity at low rate after cycling at large current densities. Returning the current density to 21 mA/g after 60 cycles, the reversible capacities recover to 145 and 158 mAh/g, in comparison to the initial capacities of 150 and 173 mAh/g. The significantly greater decrease in capacity for the 0.01 to 3 V potential window is consistent with irreversible insertion at potential greater than 2.5 V.[50]

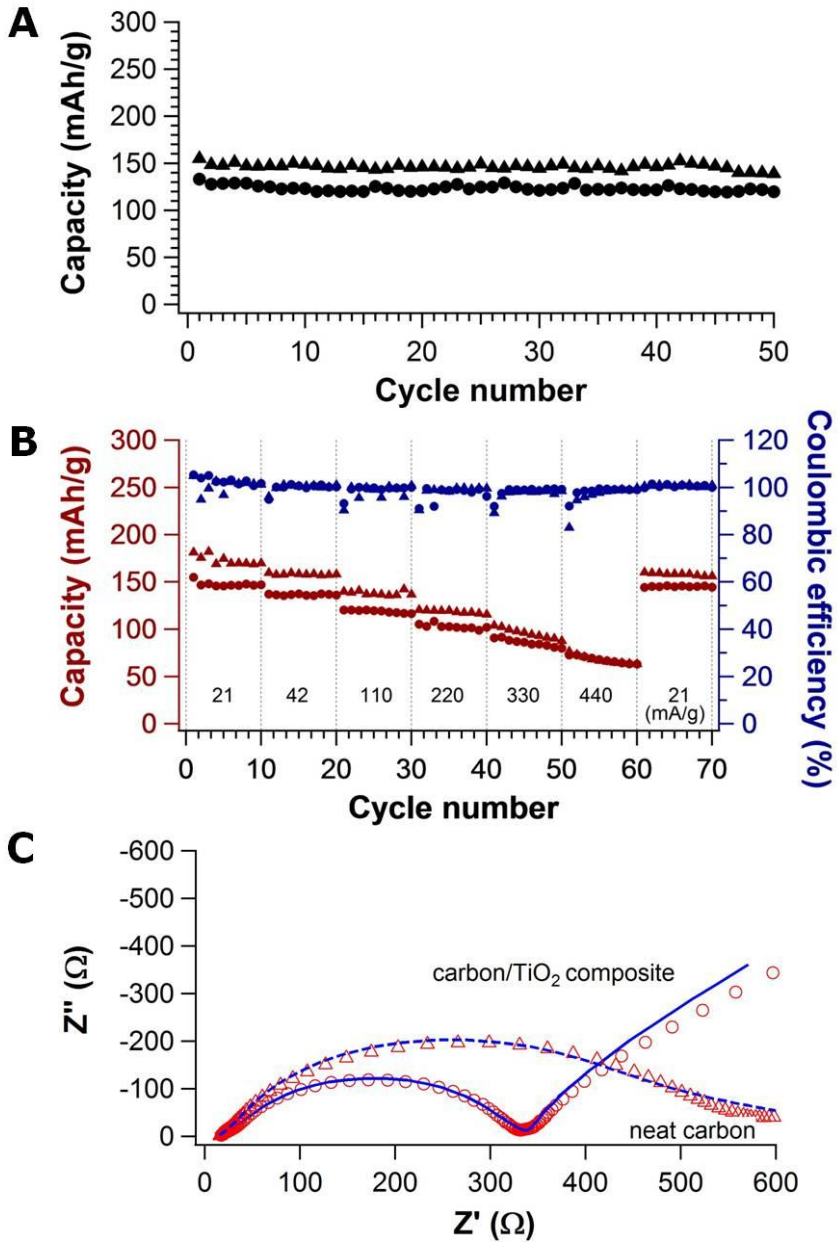

Figure 3.11. (A) Galvanostatic cycling at 42 mA/g of carbon/TiO_2 halfcells with different potential ranges: (●) 0.01 to 2.0 V and (▲) 0.01 to 3.0 V. (B) Galvanostatic cycling at elevated current densities with different potential ranges: (●) 0.01 to 2.0 V and (▲) 0.01 to 3.0 V. (C) Nyquist plot of the neat carbon (△) and carbon/TiO2 composite (○) electrode.

Figure 3.11C shows the EIS spectra of the neat carbon and carbon/TiO_2 composite electrode after 70 cycles. These spectra provide insight into the charge storage processes in terms of surface (ion adsorption and desorption) and bulk (ion diffusion) reactions.[54] The Nyquist plots are fit using the equivalent electric circuit based on the standard Randles circuit model[55] as shown in Figure 3.13. These fits provide evidence for two different SEI layers for the composite. These SEI layers are attributed to the carbon and titania surfaces in contact with the electrolyte. Interestingly if we compare the Nyquist plots for the carbon/TiO_2 composite and neat carbon electrode, the charge transfer resistance is significantly less for the composite. We attribute this behavior to the faster Na ion diffusion in the carbon/TiO_2 composite because of its hierarchical pore structure.

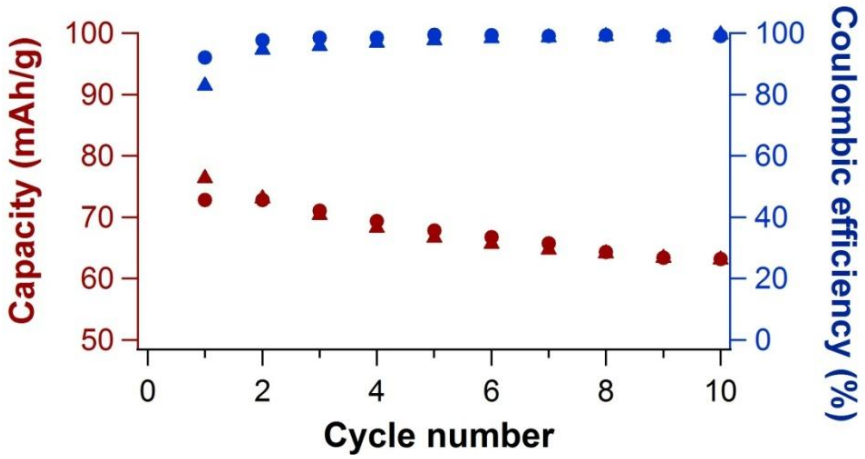

Figure 3.12. Galvanostatic cycling at 440 mA/g of carbon/TiO_2 half-cells with different potential ranges; (●) 0.01 to 2.0 V and (▲) 0.01 to 3.0 V.

Figure 3.13A shows an electric circuit model for the neat carbon electrode. The R_S indicates the bulk resistance of electrolyte, separator, and electrode. The semicircle in the high-frequency region is R_1//C circuits represented the SEI on carbon surface and the migration of Na ions through the passivation films.[56] The low frequency spectrum beyond the semicircle is attributed to an interfacial charge transfer of Na^+/Na with a resistance and double layer capacitance as well as Na ion diffusion impedance in active materials.[56] The capacitive component, denoted as a constant phase element (CPE, Q), takes into account the surface roughness or porous structure of the electrode materials. W is the Warburg impedance that corresponds to the solid-state diffusion of the Na ion into the bulk anode.

In common with the neat carbon electrode, an electric circuit model for the porous carbon/TiO_2 composite electrode is shown in Figure 3.13B. The basic concept of the circuit elements is not different from the model of the neat carbon electrode. However, this composite anode electrode consists of carbon and TiO_2 particles, and there are some TiO_2 particles protruded from carbon surface. Therefore, it leads to two different SEIs (C_1//R_1 and C_2//R_2) on carbon and TiO_2 surfaces. The interfacial charge transfer, Na ion diffusion impedance, and double layer capacitance for carbon and TiO_2 are also considered individually, and thus they are presented by a combination of Q_1//(R_3-W_1) and Q_2//(R_4-W_2) circuits in series. FD is the finite length diffusion impedance at low frequency.

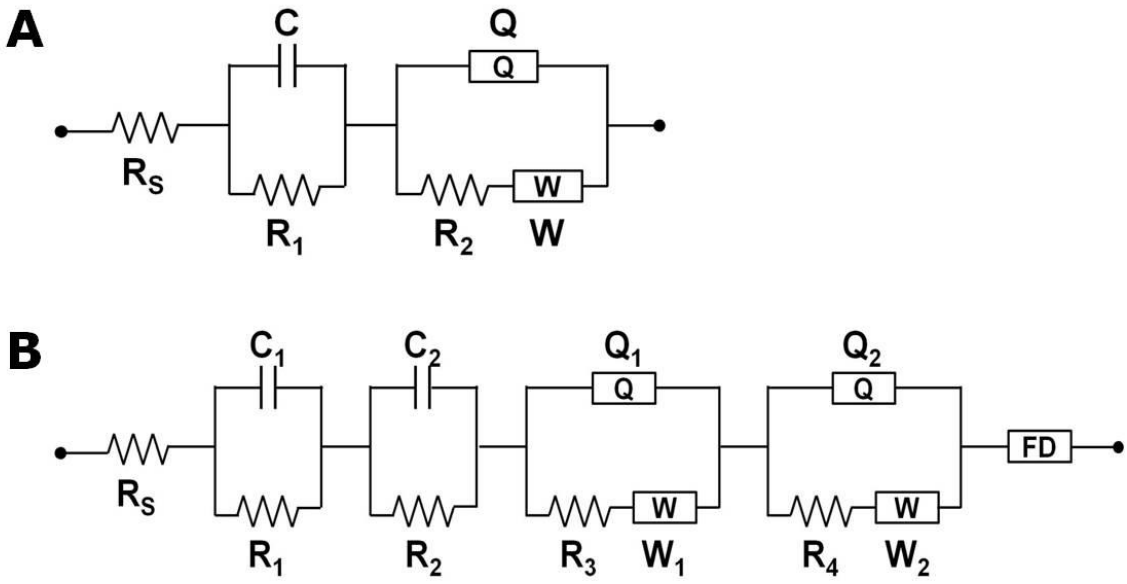

Neat carbon (A)			Carbon/TiO_2 composite (B)				
R_S	R_1	R_2	R_S	R_1	R_2	R_3	R_4
13.2	299.8	335.9	14.8	44.8	142.8	0.001	142.5

Figure 3.13. Equivalent circuit to fit the EIS data of (A) neat carbon and (B) carbon/TiO_2 composite electrodes.

3.4 Conclusions

Porous composites were fabricated via a simple polymerization induced phase separation process using a renewable carbon source (furfuryl alcohol) and an earth abundant, readily available metal oxide (TiO_2). This method provides a route to generate a low cost carbon/TiO_2 composite for the active component for the anode electrode of a sodium ion battery. The carbon/TiO_2 composite exhibited nearly 3-fold enhancement in capacity over porous carbon or carbon-coated TiO_2. The composite exhibits excellent cycle performance with less than 10% fade in capacitance observed even at high charge/discharge rates up to approximately 5 C (440 mA/g). The reversible capacity and excellent cycling stability of the carbon/TiO_2 electrode illustrates the potential of this simple polymerization induced phase separation method for the fabrication of functional materials.

CHAPTER IV

USING POLYMER BLENDS TO TUNE THE MORPHOLOGY OF NANOPOROUS CARBON/TIO_2 COMPOSITES FOR SODIUM ION BATTERIES

4.1 Introduction

In these days, lithium ion batteries have reigned over energy storage devices due to their high energy density and capacity, which come from the lightweight and low redox potential of lithium.[1-4] However, the high extraction costs and limited reserves of lithium bring one of the critical challenges for lithium ion batteries.[5-7] Unlike lithium, sodium is the 6th most abundant element estimated to be 3 orders of magnitude greater than lithium.[7] Owing to the abundance of sodium, sodium ion batteries have been spotlight recently as an alternative to lithium ion batteries, even though the sodium has two major drawbacks compared to lithium. First, the larger size of sodium (1.06 Å) compared to lithium ion (0.76 Å) hinders the intercalation and diffusion of Na^+ into electrodes.[8] Second, the sodium has 3 times heavier molar mass (23 g/mol) compared to lithium (6.9 g/mol), which produces the decrease of the specific capacity.[7] However in applications where cost dominates weight restrictions, such as grid energy storage, and in emergent markets, sodium ion batteries provide significant promise for energy storage.

Due to its low cost and abundance, hard carbon is a commonly used anode materials for sodium ion batteries.[9-11] A rate capacity between 100 and 300 mAh/g has been generally obtained for hard carbons, with the capacity dependent on both the allotrope and morphology,[7, 12-14] although Ponrouch *et al.*[11] have recently demonstrated a hard carbon anode with capacity surpassing 320 mAh/g. One intrinsic limitation associated with carbon is its limited charge storage on a volumetric basis (low mass density). Therefore, alternative materials for sodium ion battery anodes have been examined to obtain higher capacity. In particular, titanium dioxide (TiO_2) has been studied as an anode material in sodium ion batteries[8,15-19] due to its high power density compared to carbon materials, low cost, long cycle life, and ecofriendliness.[8, 15-19] However, the electrical conductivity of TiO_2 is low. Therefore, composite anode materials for sodium ion batteries that combine the merits of carbon and TiO_2 have been extensively investigated.[20, 21] For example, Yang *et al.*[22] fabricated N-doped TiO_2 nanorods decorated with carbon dots with capacity of ~250 mAh/g, and carbon-coated TiO_2 nanoparticles by Jiang *et al.*[23] exhibited a capacity of ~240 mAh/g. Alternative composites based on nanosized binary elemental alloys such as SnSb/C (435 mAh/g)[24] and Sn–SnS–C (664 mAh/g)[25] can provide further improvements in the capacity, but at the expensive of cost and environmental impact.

A significant challenge with the development of high performance composite electrodes for sodium ion batteries is to understand how the morphology impacts the performance.[26] Ionic and electronic conduction pathways are critical to develop to enable high performance, while high surface area electrodes imply a high contact area with the electrolyte, which should ease the ions flux across the electrode/electrolyte interface.[27, 28]

However, the long term performance of high surface area electrodes is limited in many cases by the generation of the solid electrolyte interphase (SEI) layer. The SEI layer formation consumes electrolyte and alkali metal ions[29] and tends to result in an irreversible capacity loss during the initial charge cycle. However, the SEI layer is generally electronically insulating and ionically conducting to protect the electrolyte from further decomposition if the SEI is stable.[30] Agubra *et al*. have demonstrated that the electrolyte decomposition and subsequent SEI layer formation on an anode electrode increases the impedance in lithium ions.[31] Recently, analysis of the SEI formation on $Na_2Ti_3O_7$ anodes revealed the reaction between a standard binder (polyvinylidene difluoride) and the electrolyte that leads to an unstable SEI layer.[32] However, the interplay between morphology and SEI layer formation in composite electrodes has not been thoroughly investigated for sodium ion batteries.

Here, we investigate the interplay between morphology, SEI formation and performance for carbon/TiO_2 composite anode electrodes for sodium ion batteries. The reversible capacity of these anodes for sodium ion batteries(< 130 mAh/g) is inferior to the state-of-the-art for carbon/TiO_2 (e.g. 155 mAh/g for microsphere C-TiO_2[33] and 242 mAh/g for carbon-coated TiO_2 nanoparticles[23]), but the fabrication of these composites is simple and tunable, based on polymerization-induced phase separation using inexpensive and commercially available materials. This method enables identification of key morphological aspects that impact the performance of the composites. In this case, commercial TiO_2 nanoparticles are dispersed in furfuryl alcohol solution containing poly(hydroxyethyl methacrylate), PHEMA, and a photoacid generator (PAG). UV exposure generates a superacid to induce polymerization to poly(furfuryl alcohol), PFA;

PFA provides the carbon matrix of non-graphitizing char,[34] while PHEMA fully decomposes to yield pores during carbonization. The morphology of these porous carbon/TiO_2 composites can be readily controlled using the molecular weight of the PHEMA and relative concentration of components. This simple route to modulate the morphology enables improved understanding of the SEI formation in these composites for sodium ion batteries.

4.2 Experiment

Materials. Furfuryl alcohol (FA, 98%), ethyl alcohol (EtOH, ≥ 99.5%), *N*-methyl-2-pyrrolidone (NMP, 99.5%), and poly(vinylidene fluoride) (PVDF, M_n = 107 kDa) were obtained from Sigma-Aldrich and used as received without further purification. Poly(2-hydroxyethyl methacrylate) (PHEMA) with nominal M_w = 20 kg/mol (20K), 300 kg/mol (300K), and 1000 kg/mol (1000K) was purchased from Scientific Polymer Products, Inc. (Ontario, NY) and used as received. Titanium oxide (TiO_2, anatase, 15 nm) was purchased from Nanostructured & Amorphous Materials, Inc. The TiO_2 particles were separated from water by centrifugation (accuSpin™400, Fisher Scientific) at 7000 rpm for 5 min, and the highly concentrated TiO_2 slurry was re-dispersed into deionized water and EtOH using an ultrasonic cleaner (VWR® symphony™, operating frequency: 35 kHz, VWR International) to remove the surfactant dispersant and then collected again by centrifugation. This washing process was repeated 3 times. Rhodorsil PI2074 (CAS#: 178233-72-2) was obtained from Promerus, LLC (Brecksville, OH) and used as the photoacid generator. Sodium perchlorate ($NaClO_4$, 98%, Sigma Aldrich) dissolved in a 1:1 (v/v) mixture of ethylene carbonate (EC, 99%, Sigma Aldrich) and propylene carbonate (PC, 99.7%, Sigma Aldrich) was used as an electrolyte for battery testing. Na metal (99.8%, Acros Organics) was used as the counter electrode and copper foil (0.025 mm thick, Puratronic®) was used as a current collector of the anode electrode in the coin cells.

Fabrication of PHEMA/PFA/TiO_2 composites. In order to fabricate the composites, 0.35 g of PHEMA was dissolved in a mixture of FA (0.2, 0.3, 0.5, or 0.7 g) and 0.2 g EtOH. 0.3 g of TiO_2 was ultrasonically dispersed in 0.3 g EtOH and 1.5 mg of

Rhodorsil PI2074 was dissolved in this suspension. This mixture was combined with the polymer solution and cast into a PTFE petri dish to a thickness of ~0.2 mm. FA polymerization was induced by broadband UV (Spectroline, 4500 μW/cm) exposure and polymerization was carried out at 60 ºC for 10 min. The composite was pyrolysed at 900 ºC in N_2 at 1 ºC/min to 650 ºC with 3 h hold at 650 ºC, 1 ºC/min to 900 ºC, and then hold at 900 ºC for 1 h. The temperature was then decreased at 3 ºC/min to room temperature.

Characterization. The morphology was characterized by transmission electron microscopy (TEM, JSM-1230, 120 kV, JEOL). Cross-sections of the composites, approximately 70 nm thick, were prepared by ultramicrotome (PT-PC PowerTome, RMC) using a diamond knife. To enable microtomed samples, the composite was embedded in epoxy resin (Embed-812 Resin, Electron Microscopy Sciences) that was hardened at 60 ºC for 12 h. The specimens were supported on a 3.05 mm diameter Cu grid (01753-F, TED PELLA, Inc.). The mobility of precursor during FA photopolymerization is characterized by a viscometer (Rotonetic™ 2 drive, Bohlin Gemini). During the measurement of viscosity, the OmniCure® S2000 (200 W Mercury Arc, Lumen Dynamics) is used as the UV light source for FA photopolymerization. The pore texture was elucidated by Nitrogen adsorption/desorption isotherms (Micromeritics TriStar II instrument) at 77 K to determine the specific surface area by the Brunauer-Emmett-Teller (BET) method. The composition of the composite was estimated from thermogravimetric analysis TGA Q50 (TA Instrument) with a heating rate of 20 ºC/min to 700 ºC in air. To avoid excess water in the sample, the composite materials were dried overnight under vacuum at 85 ºC. All mass loss was attributed to removal of carbon. Powder X-ray diffraction was used to confirm the crystal structure of TiO_2 particles by Ultima IV

(Rigaku, Japan) (operating at 40 kV and 35 mA, Cu K_α radiation) with scanning range 20°-60°, a step size of 0.04° and a rate of 1°/min. To conduct quantitative XRD, relative intensity ratio (RIR) method was used. The RIR values are determined by the following equation

$$\frac{I_\alpha}{I_\beta} = K\frac{W_\alpha}{W_\beta}$$

where, I_α and I_β are characteristic peak intensities of α and β phases, W_α and W_β are weight fractions of α and β respectively. K is a constant determined by calibration curve with known samples.[35] The chemical composition of the neat and charge-discharge cycled carbon/TiO_2 composite anodes was probed with X-ray photoelectron spectroscopy (XPS, PHI 5000 Versa probe II scanning XPS microprobe, ULVAC-PHI, Inc.) at a takeoff angle of 45 using pass energy of 11.75 eV at 2×10^{-6} Pa. High resolution scans at energies associated with C1s and O1s were performed to understand differences in the oxidation states. Each spectrum was collected using a monochromatic (Al Kα) x-ray beam (1486 eV) over a 200 μm diameter probing area. The peaks in the XPS spectra were fit using PHI MultiPak software.

Battery fabrication and testing. The carbonized composite materials were ground by mortar and pestle into a powder and mixed with carbon black (N330, Sid Richardson Co.), and PVDF (binder) at 85:5:10 (w/w/w) ratio for solids. A small amount of NMP (~0.03 g) was added to generate a concentrated slurry. The slurry was coated onto 13 mm (diameter) punched copper foil using a Mayer rod (RDS 22) and the coated foil was dried overnight in vacuum at 80 ºC. Representative anodes contained approximately 1.5 mg of active material. CR2032 coin cells (MTI Corporation) were

assembled in an Ar-filled glove box (O_2 < 0.5 ppm, H_2O < 0.5 ppm) using the composite on copper foil as the anode electrode, Na metal as the cathode electrode, Celgard® 3501 (Celgard, LLC.) as the separator, and 1 M solution of $NaClO_4$ in EC and PC (1:1 v/v) as the electrolyte.

The performance of the coin cells was determined using galvanostatic charge and discharge experiments with a battery tester (BST8-WA, MTI) at current densities between 10 and 50 mA/g. The potential window used was 0.01 - 2.0 V vs. Na/Na^+, consistent with prior studies for Na-ion batteries using TiO_2 as the active anode.[7, 16, 21] Cyclic voltammetry (CV) and electrochemical impedance spectroscopy (EIS) analysis were carried out in CR2032 coin cells using an electrochemical workstation CHI660D (CH Instruments). The CV was done in a potential range of 0.01 - 2.0 V at a scan rate of 0.1 mV/s, and the EIS was conducted with applied amplitude of 5 mV in the range of 100 kHz to 0.01 Hz after operating the electrodes for 30 or 40 cycles.

For the SEI layer characterization, the cycled coin cells were carefully opened using a disassembling machine (MSK-110D, MTI), and the carbon/TiO_2 composite electrodes were briefly rinsed by propylene carbonate and subsequently ethanol. The rinsed electrodes were dried and stored in a vacuum oven at 80 ºC before analyses. The electrodes compared with the cycled electrodes are also produced using the concentrated slurry with carbon/TiO_2 composite, carbon black, PVDF, and NMP. And then they were assembled as coin cells with sodium metal, separator, and electrolyte. These control coin cells also were disassembled, and then the control electrodes were rinsed, and dried.

4.3 Results and discussion

Figure 4.1A illustrates the N_2 adsorption–desorption isotherms for the carbon/TiO_2 composites fabricated with varying molecular weight of PHEMA. These materials all exhibit type IV isotherms with a hysteresis loop at high relative pressures, P/P0.[35] For the small molecular weight PHEMA, the hysteresis loop closes near P/P_0 ~ 0.9, which suggests the primary pores are connected by large mesopore windows. Conversely, the composite fabricated with the high molecular weight (1000K) PHEMA exhibits a much broader hysteresis loop that does not close until P/P_0 ~ 0.4. This suggests a broad distribution in window size between primary pores with small mesopores connecting the larger pores. The surface area of these composites increases with the molecular weight of PHEMA from 43.03 (20K) to 63.83 m^2/g (1000K), which corresponds with changes in morphology of the carbon/TiO_2 composites (Figure 4.2). The pores of the carbon/TiO_2 composite are significantly larger for the composite produced using 20K PHEMA (Figure 4.2A) than the carbon/TiO_2 composites from 300K (Figure 4.2B) and 1000K PHEMA (Figure 4.2C). The morphology of porous carbon/TiO_2 composites pyrolyzed from PHEMA/FA/TiO_2 appears to be controlled by the mobility of the precursor suspension that decreases as the molecular weight of PHEMA increases. The mobility of precursor is estimated through a viscosity of the solution, and is measures by a viscometer during FA polymerization. The results are shown in Figure 4.3. The viscosity of all solutions increases in process of the polymerization time. Especially, higher viscosity is shown at the solution using higher molecular weight of PHEMA. It indicates that the mobility of the precursor is hindered more by higher molecular weight of PHEMA. Additionally, agglomeration of the TiO_2 nanoparticles increases as the

molecular weight of PHEMA increases. In these cases, the nanoparticles appear to be pushed towards pore interface in the carbon matrix.

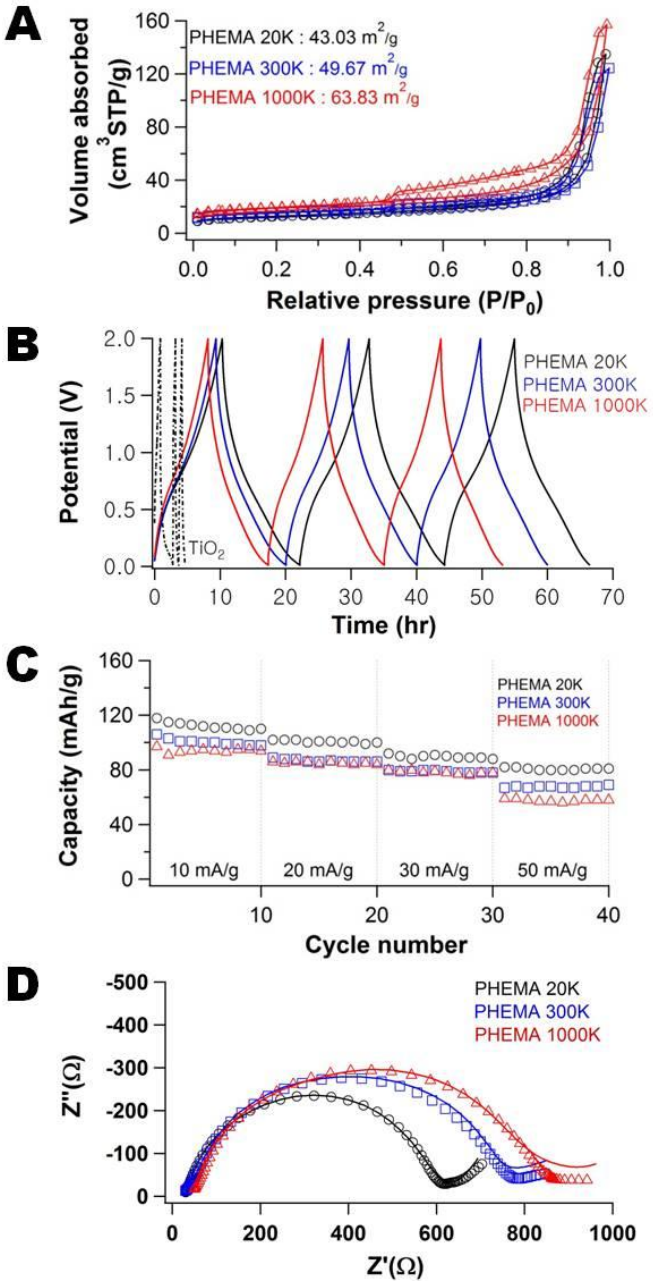

Figure 4.1. (A) N_2 adsorption and desorption isotherms, (B) Galvanostatic charge/discharge behavior of neat TiO_2 and porous carbon/TiO_2 composites from 20K, 300K, and 1000K PHEMA in a potential range of 0.01–2.0 V at a current density of 10 mA/g, (C) Galvanostatic cycling, and (D) Nyquist plots of the porous carbon/TiO_2 composite fabricated using 0.35 g PHEMA/0.3 g FA/0.3 g TiO_2 as a function of molecular weight of PHEMA: 20K (○), 300K (□), and 1000K (△).

Figure 4.1B is the galvanostatic charge-discharge behavior of the neat TiO_2 and carbon/TiO_2 composites from 20K, 300K, and 1000K of PHEMA. The porous carbon/TiO_2 composite anodes provide much more stable glavanostatic charge-discharge behavior and higher capacity value compared to TiO_2 anode produced with carbon black, PVDF, and NMP as shown in Figure 4.4. The poor cycling performance of the TiO_2 anode is caused by the structural changes during the insertion/desertion of sodium.[37] Especially, the profiles of TiO_2 anode during charging (Figure 4.4A) are rough compared to those of carbon/TiO_2 composite anode (Figure 4.4B). It suggests that insertion of Na into TiO_2 should not be reversible.

Figure 4.1C illustrates the impact of molecular weight of PHEMA used in the fabrication of the anode on the capacity of the porous carbon/TiO_2 composite anodes for a range of charge−discharge rates. Although high surface area generally improves the capacity by increasing the flux across the electrode/electrolyte interface,[27] the capacity of these porous carbon/TiO_2 composite anodes decreases with increasing surface area. This behavior is somewhat surprising as the capacitive fade on cycling is quite small as shown in Figure 4.1B. The capacity is stable for all materials examined after approximately 10 cycles. Increasing the current density from 10 mA/g (about 0.1 C) up to 50 mA/g (about 0.8 C) decreases the capacity for all samples; however, the highest capacity is always found for the composite fabricated with the lowest molecular weight PHEMA.

Figure 4.1D shows the EIS spectra of the carbon/TiO_2 composite electrodes after 40 charge-discharge cycles as a function of the molecular weight of PHEMA used in their fabrication. These spectra provide insight into the surface (ion adsorption and desorption) and bulk (ion diffusion) processes associated with charge storage.[38] Nyquist plots for

these electrodes exhibit a semi-circle at high frequency and then a linear increase at low frequency associated with the Na^+ ion diffusion in the anode material (Warburg impedance).[39] As the molecular weight of PHEMA increases, the diameter of semi-circle increases (increased the charge transfer resistance[9]). Additionally, the ohmic resistance, R_Ω, associated with the bulk carbon, grain boundary and interface resistances determined at high frequency (Z' ~ tens of Ω) increases slightly as the molecular weight of the PHEMA used in the fabrication increases. This behavior is somewhat unexpected as the composition for the electrodes are identical. This increased R_Ω suggests that the extent of the SEI formation is dependent on the pore morphology. The higher surface area electrodes exhibit increased resistance from both R_Ω and the SEI layer. At low frequency after the semi-circle, the impedance is associated with the semi-infinite diffusion of the Na^+ ions. However, the impedance for the composite fabricated with the highest molecular weight PHEMA behaves unexpectedly with Z'' nearly independent of Z'. This decrease of Warburg slope (semi-infinite diffusion) as a function of the molecular weight of PHEMA is directly to the diffusion limitations of the system.[40]

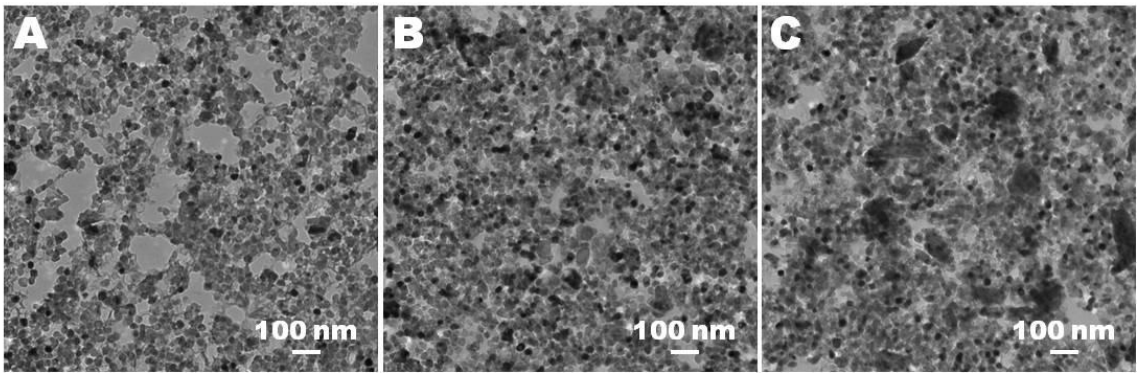

Figure 4.2. TEM micrographs of porous carbon/TiO_2 composites fabricated with (A) 20K, (B) 300K, and (C) 1000K PHEMA using 0.35 g PHEMA/0.3 g FA/0.3 g TiO_2 for the precursor.

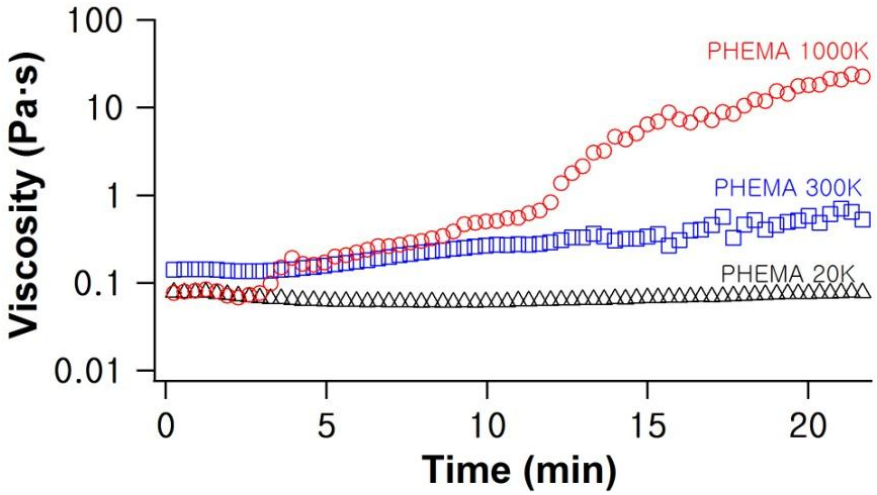

Figure 4.3. Viscosity variation of FA/PHEMA solutions with different molecular weight of PHEMA during FA polymerization.

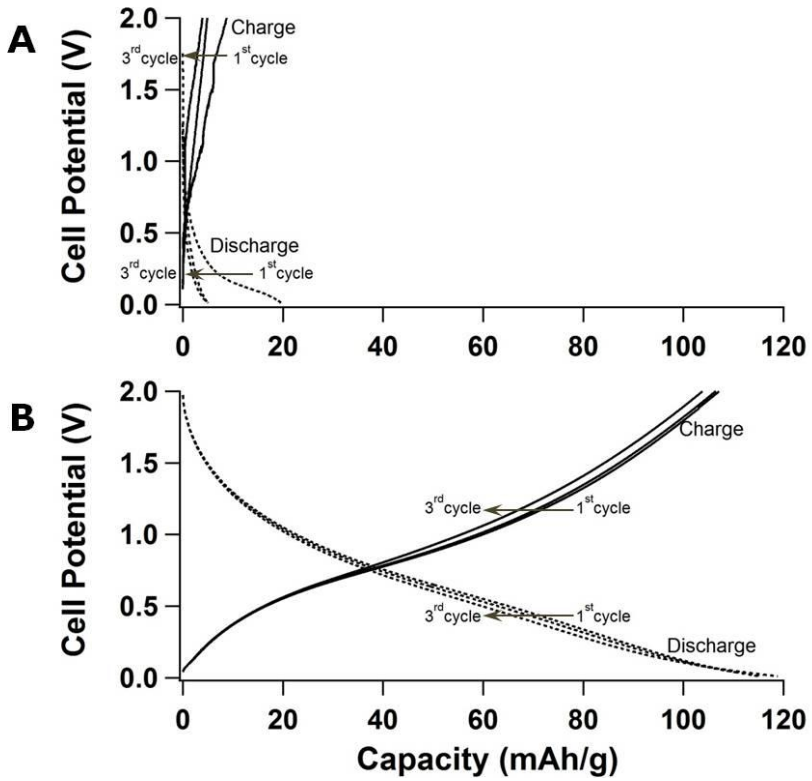

Figure 4.4. Galvanostatic charge/discharge behavior of (A) TiO_2 and (B) carbon/TiO_2 composites from 20K of PHEMA and 0.3 g of FA in a potential range of 0.01–2.0 V at a current density of 10 mA/g.

An electric circuit model for the porous carbon/TiO_2 composite electrode is shown in Figure 4.5. R_S indicates the bulk resistance of electrolyte, separator, and electrode. These composite anode electrodes consist of carbon and TiO_2 particles. According to the previous study,[7] the carbon and TiO_2 particles lead to two different SEIs ($C_1//R_1$ and $C_2//R_2$). In addition, the interfacial charge transfer, Na ion diffusion impedance, and double layer capacitance for carbon and TiO_2 are considered individually, and thus they are presented by a combination of $Q_1//(R_3\text{-}W_1)$ and $Q_2//(R_4\text{-}W_2)$ circuits in series. FD is the finite length diffusion impedance.

The formation of SEI layer is further investigated through cyclic voltammetry as shown in Figure 4.6. The redox peaks were observed between 0.01 and 1.0 V owing to the insertion and extraction of sodium ion at the carbon/TiO_2 composite.[41] In the first cathodic scan, the current peaks at over 1.0 V are observed, whereas these peaks disappear in the second scan. This is attributed to the irreversible formation of the SEI layer at the first cycle.[41] The peaks fade away with increasing the charge/discharge cycle numbers, and the charge/discharge cycles have stabilized after 10 cycles.

To confirm the change of TiO_2 polymorphs during carbonization, XRD was used as shown in Figure 4.7. It demonstrates that the carbonized composite still contains anatase TiO_2 nanoparticles from XRD with strong diffraction peaks at ~26° and ~48°. These peaks are in good agreement with the standard spectrum for anatase (JCPDS no.: 84−1286).[42] Although the content of rutile TiO_2 increases from 1.7 % to 10.4 % after carbonization of PFA/PHEMA/TiO_2 composite, over 91 % of anatase-TiO_2 remains without transformation. The Rutile TiO_2 has strong diffraction peaks at ~28°, ~36° and ~54° (JCPDS no.: 76-1940).[43]

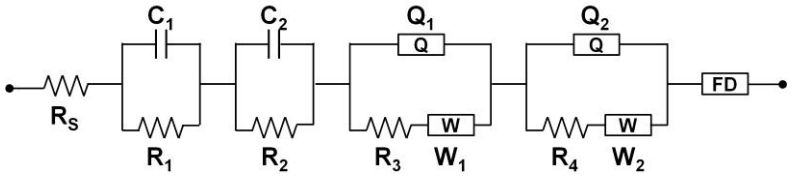

	R_S (Ω)	R_1 (Ω)	R_2 (Ω)	R_3 (Ω)	R_4 (Ω)	C_1 (F)	C_2 (F)	Q_1 ($S \cdot s^n$)	Q_2 ($S \cdot s^n$)	W_1 ($S \cdot s^{1/2}$)	W_2 ($S \cdot s^{1/2}$)
PHEMA 20K	3.9	3.0×10	4.1×10^{2}	2.1	1.8×10	3.6×10^{-1}	7.0×10^{-6}	1.3×10^{-5}	4.3×10^{-3}	4.3×10^{-2}	4.2×10^{-4}
PHEMA 300K	1.5×10	3.5×10^{2}	4.2×10^{2}	4.7×10^{2}	9.3	3.0×10^{-5}	9.2×10^{-6}	2.6×10^{-4}	1.8×10^{-2}	1.8×10^{5}	4.5×10^{-12}
PHEMA 1000K	2.5×10	3.9×10^{2}	2.3×10^{2}	2.9×10^{2}	3.4×10	1.5×10^{-5}	6.4×10^{-6}	8.9×10^{-4}	9.7×10^{-5}	2.1×10^{-2}	1.3×10^{4}
FA 0.2 g	3.4	2.4×10^{2}	2.0×10^{2}	1.0×10^{-1}	1.2×10	1.1×10^{-5}	4.0×10^{-5}	1.0×10^{-12}	5.3×10^{-3}	1.6×10^{-2}	2.0×10^{2}
FA 0.3 g	3.9	3.0×10	4.1×10^{2}	2.1	1.8×10	3.6×10^{-1}	7.0×10^{-6}	1.3×10^{-5}	4.3×10^{-3}	4.3×10^{-2}	4.2×10^{-4}
FA 0.5 g	1.1×10	1.8×10^{2}	2.1×10^{2}	1.3×10^{2}	4.7×10^{2}	2.7×10^{-5}	7.3×10^{-6}	3.5×10^{-4}	4.9×10^{-3}	2.6×10^{-2}	1.1×10^{5}
FA 0.7 g	1.2×10	2.1×10^{2}	5.0×10	1.9×10^{2}	1.7×10^{3}	8.9×10^{-6}	1.5×10^{-5}	3.4×10^{-4}	7.1×10^{-3}	1.0×10^{5}	4.2×10^{9}

Figure 4.5. Equivalent circuit to fit the EIS data of porous carbon/TiO_2 composite electrodes and numerical values of the equivalent circuit components obtained for the impedance data.

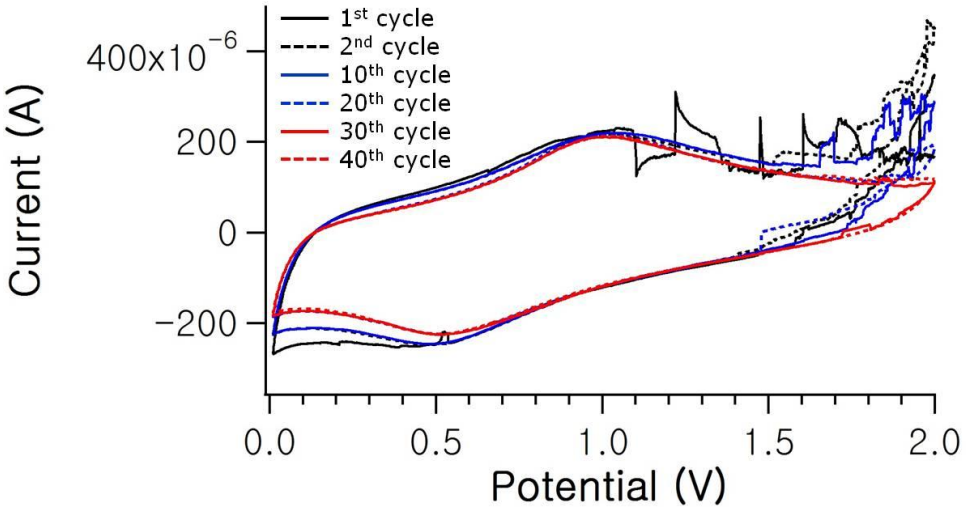

Figure 4.6. Cyclic voltammetry of the carbon/TiO_2 composite from 20K of PHEMA at a scan rate of 0.1 mV/s with sodium metal as both counter and reference electrodes.

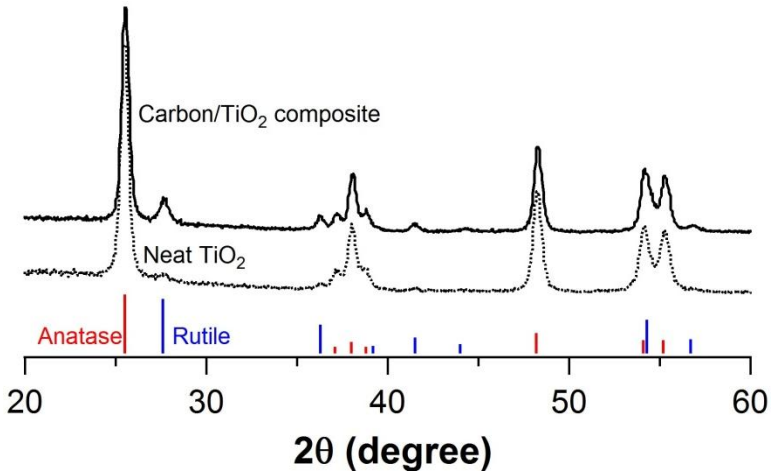

	Anatase	Rutile
Neat TiO_2	98.3 %	1.7 %
Carbon/TiO_2 composite	89.6 %	10.4 %

Figure 4.7. XRD profiles for the neat TiO_2 and carbon/TiO_2 composite produced by carbonization of PHBMA/PFA polymer blend with TiO_2 and the standard spectrum of anatase TiO_2 (JCPDS 84−1286, red lines) and rutile TiO_2 (JCPDS 75-1753, blue lines).

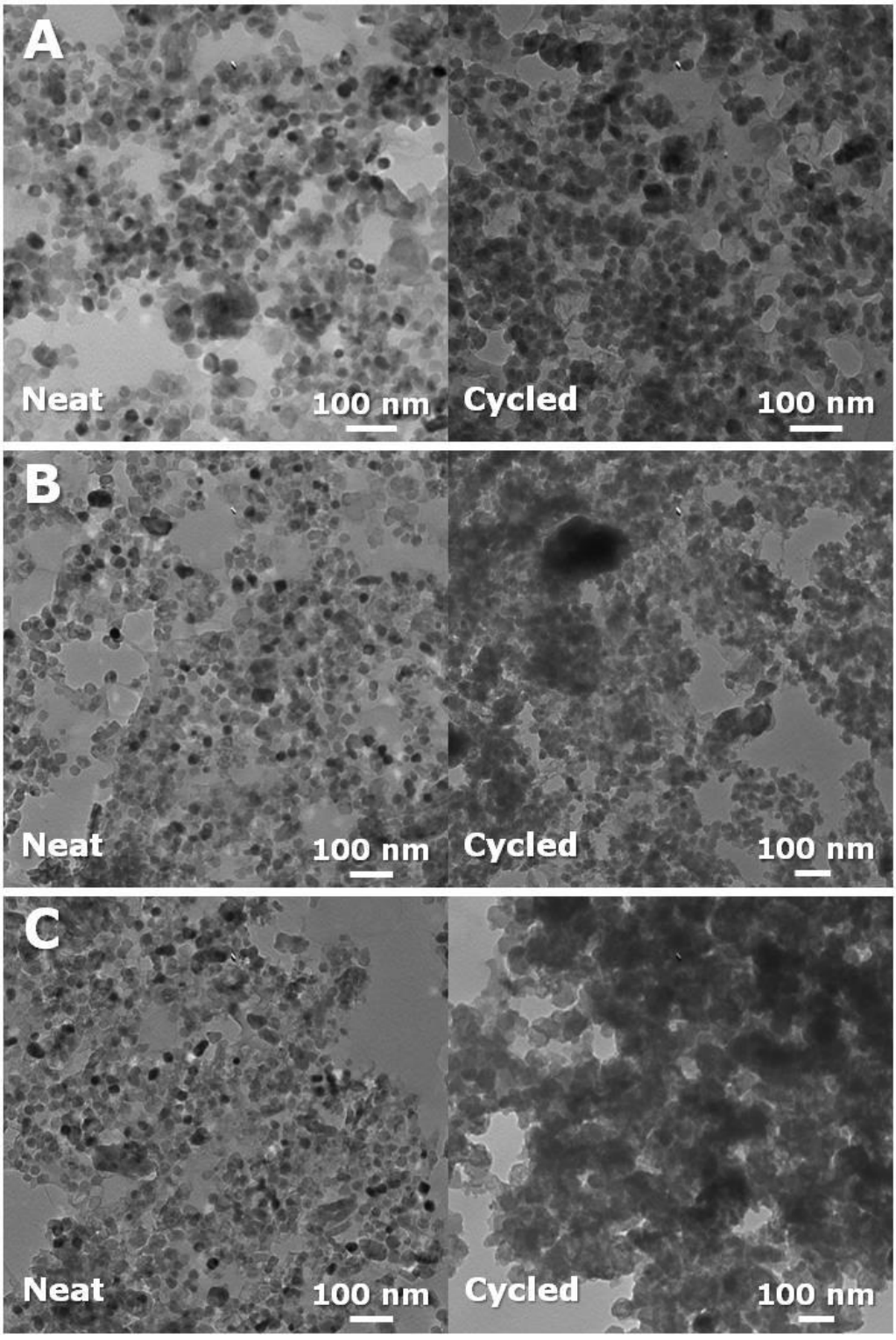

Figure 4.8. TEM images of carbon/TiO_2 composite anodes as-produced (left) and after 40 charge-discharge cycles (right) fabricated with (A) 20K, (B) 300K, and (C) 1000K PHEMA using 0.35 g PHEMA/0.3 g FA/0.3 g TiO_2 for the precursor.

To better understand the origins of the differences in impedance, Figure 4.8 illustrates the morphology of the neat composite anodes (left) and after 40 charge-discharge cycles (right) as a function of molecular weight of PHEMA used in the fabrication. Consistent with the N_2 sorption isotherms, the neat composite anodes contain smaller pores as the molecular weight of PHEMA used in their fabrication increases (as shown in Figure 4.9). We attribute this pore size dependence to the mobility during the FA polymerization. These differences in the morphology significantly impact the SEI layer thickness from the decomposition of electrolyte as shown in Figure 4.8 with the smaller pore sizes leading to greater changes in the morphology observed by TEM. This behavior is consistent with SEI formation in lithium ion electrodes where the decomposition is proportional to the surface area of the carbon electrode.[44] In examining the morphology after cycling, increased in dark spots in the TEM micrographs are attributed to the SEI layer due to its high electron density oxygen-rich substances, such as Na_2CO_3, R-OCO_2Na, and R-CH_2ONa.[45, 46] As shown on right side panels in Figure 4.8, the density of these dark spots increases with increasing surface area. The thick SEI layer associated with the composite fabricated with high molecular weight PHEMA likely leads to the high impedance of the electrodes as shown in Nyquist plots (Figure 4.1D).

In order to obtain complementary information about the SEI layer, XPS spectra are obtained after 40 charge-discharge cycles (as shown in Figure 4.10). The results from the XPS analysis are shown in Table 4.1 and the composition changes of C, O and Na between as-produced and cycled electrodes occur significantly due to the formation of SEI layer on the surface of electrodes at the first charge-discharge cycle. As a result, the molar ratio of O and Na to C after 40 charge-discharge cycles increases; for instance, the

molar ratio of C : O : Na for the composite anode fabricated with 20K PHEMA changes from 1 : 0.3 : 0 to 1 : 1.6 : 1.1 because of the decomposition of the electrolyte (a solution of $NaClO_4$ in EC and PC) and the formation of the passivating SEI layer from the breakdown of the electrolyte on the surface of the electrodes.

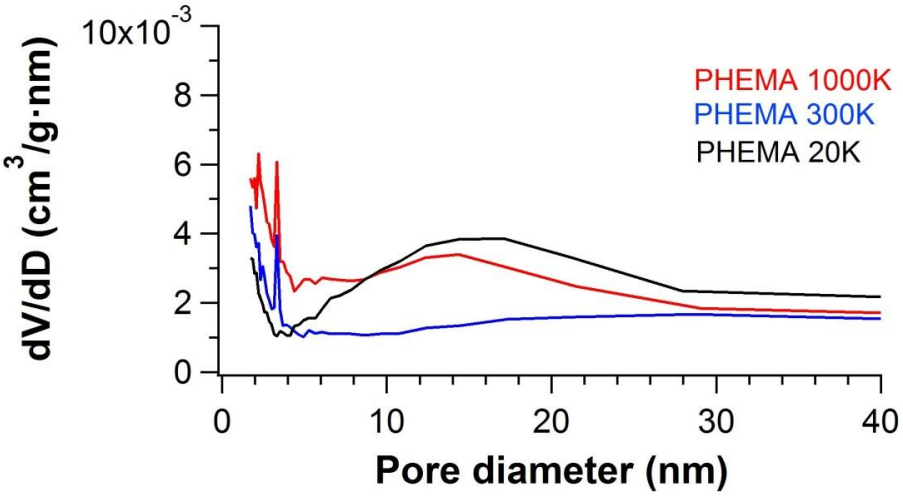

Figure 4.9. Pore size distribution of carbon/TiO_2 composites fabricated with 20K, 300K, and 1000K PHEMA using 0.35 g PHEMA/0.3 g FA/0.3 g TiO_2 for the precursor.

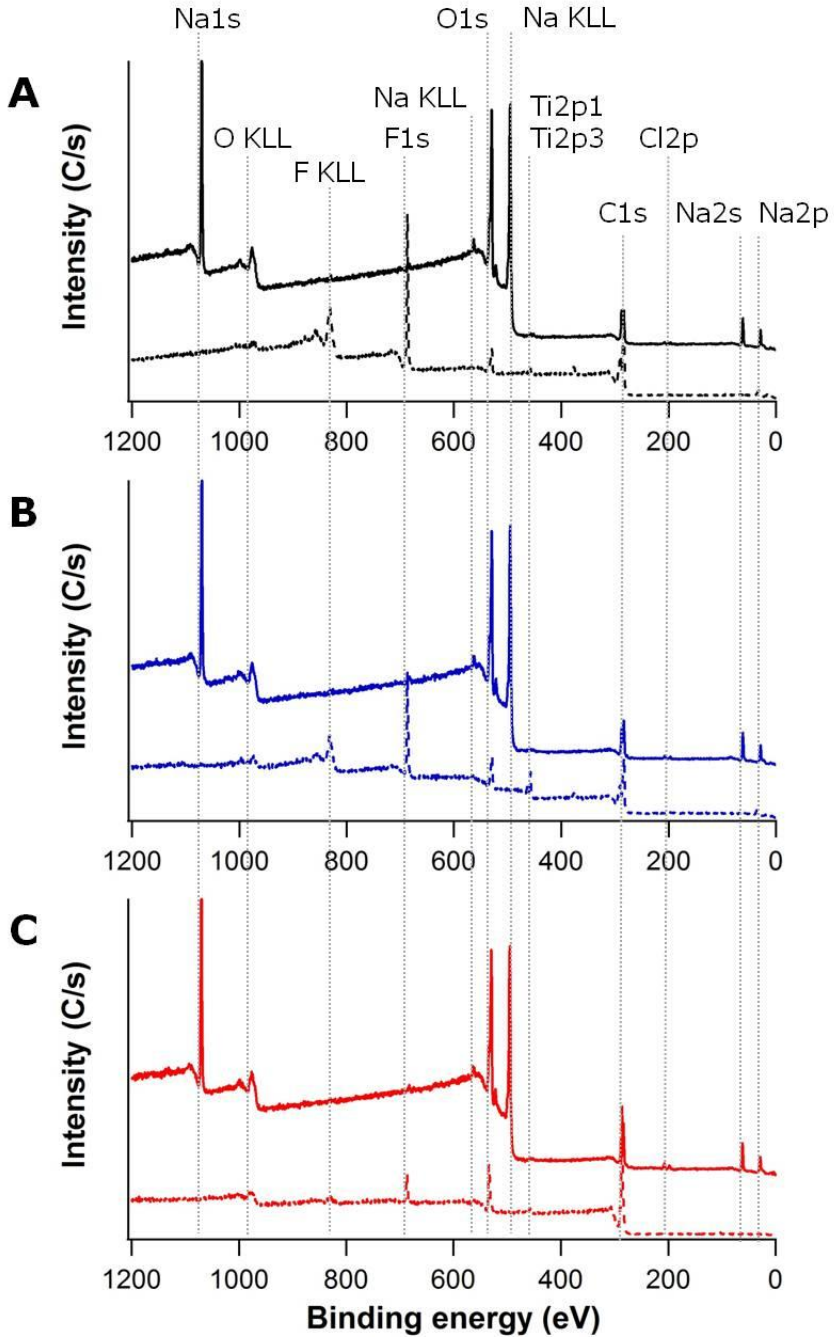

Figure 4.10. XPS spectra of neat (dash line) and 40 charge-discharge cycled (solid line) carbon/TiO_2 composite anodes fabricated with (A) 20K, (B) 300K, and (C) 1000K PHEMA using 0.35 g PHEMA/0.3 g FA/0.3g TiO_2 for the precursor.

Table 4.1. Surface elemental composition from XPS of carbon/TiO_2 composite anodes fabricated with 20K, 300K, and 1000K PHEMA using 0.35 g PHEMA/0.3 g FA/0.3 g TiO_2 for the precursor for the as-produced composite and after 40 charge-discharge cycles

PHEMA	As-produced						Cycled					
	C%	O%	Na%	Ti%	Cl%	F%	C%	O%	Na%	Ti%	Cl%	F%
20K	64.3 ± 1.7	20.1 ± 7.2	0	4.6 ± 2.1	0	16.7 ± 0.5	27.1 ± 1.1	42.7 ± 0.9	29.3 ± 1.0	0.1 ± 0.04	0.7 ± 0.04	0.2 ± 0.1
300K	70.8 ± 4.8	16.3 ± 4.8	0	2.1 ± 0.2	0	10.2 ± 8.9	28.2 ± 0.8	43.9 ±1.6	26.5 ± 0.5	0.1 ± 0.03	0.9 ± 0.1	0.4 ± 0.1
1000K	82.7 ± 1.3	13.6 ± 0.2	0	1.2 ± 1.2	0	2.3 ± 1.4	36.7 ± 4.1	40.5 ± 1.0	22.0 ± 2.0	0.1 ± 0.04	0.5 ± 0.4	0.3 ± 0.2

To better understand the composition of the SEI layers, high-resolution XPS is used to investigate the 1s binding of C as shown in Figure 4.11. The strong C1s peak at ~284.6 eV is assigned to C-C bonds in the electrode and the C-C bonds are expected to be present in the carbon component of the neat composite. The oxygen-rich components associated with the SEI layer formed by electrolyte (EC and PC) decomposition are associated with the C-O-C bonds at ~286.2 eV and O-C=O bonds at ~289 eV.[47, 48] Intriguingly, as a function of the molecular weight of PHEMA used (20K vs. 1000K) in their fabrication, the peak intensity and peak area of O-C=O decrease from 521 C/s (44 % of C area) to 330 C/s (26.2 % of C area), whereas the peak intensity and peak area of C-O-C increase from 212 C/s (17.8 % of C area) up to 274 C/s (24.0 % of C area). The increases of C-O-C peak intensity and area are attributed to the electrolyte (EC and PC) decomposition, where the C=O bonds in EC and PC are reduced to C-O.[49] The enhanced C-O-C bonds when the electrode is fabricated with higher M_n PHEMA is expected based on the TEM micrographs that illustrate the increased SEI formation for composites fabricated with the higher M_n PHEMA.

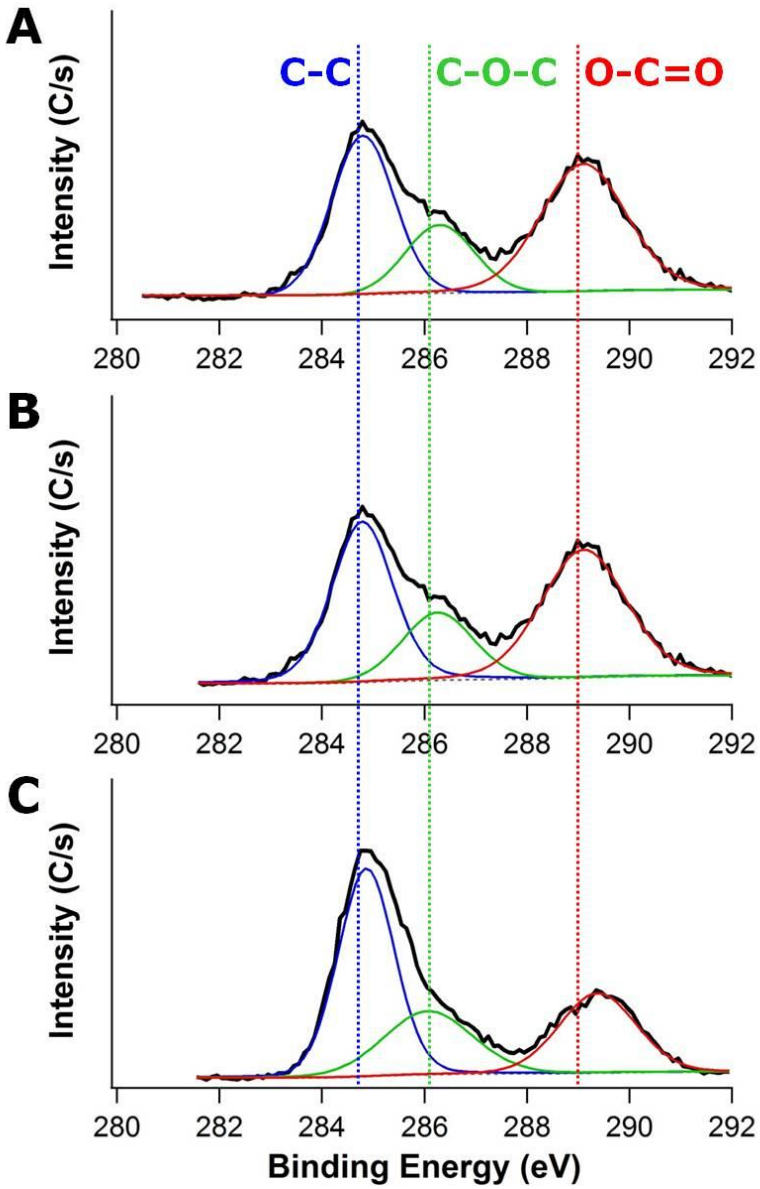

Figure 4.11. XPS spectra of carbon/TiO_2 composite anodes after 40 charge-discharge cycles fabricated with (A) 20K, (B) 300K, and (C) 1000K PHEMA using 0.35 g PHEMA/0.3 g FA/0.3g TiO_2 for the precursor.

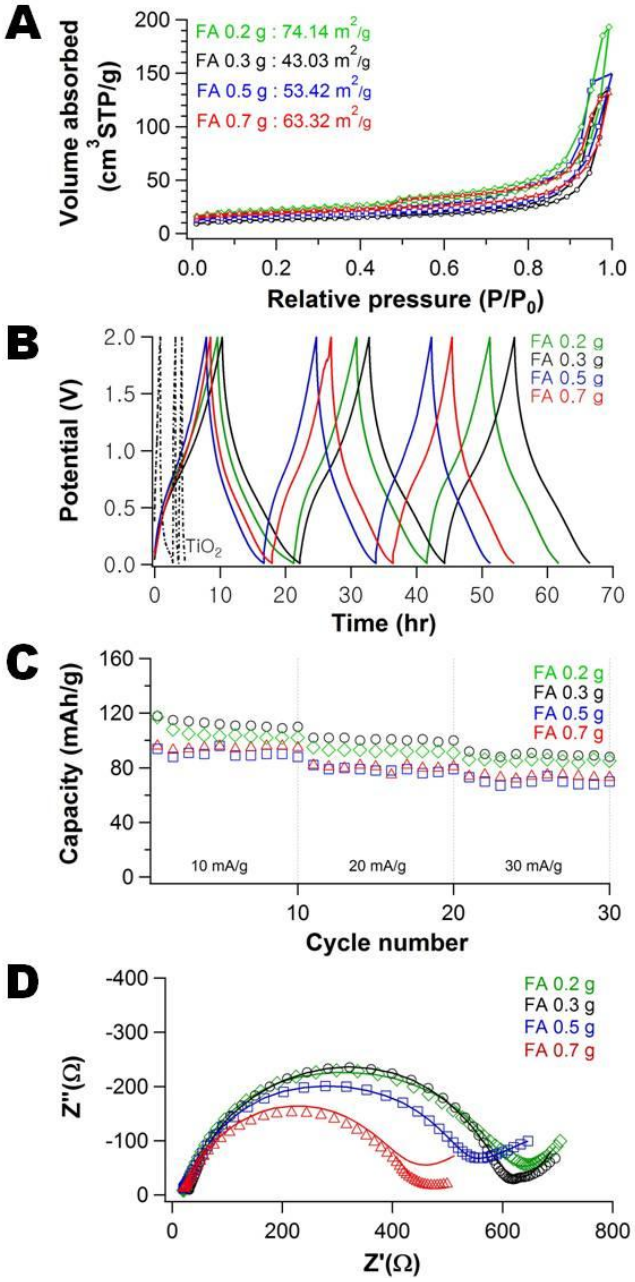

Figure 4.12. (A) N_2 adsorption and desorption isotherms, (B) Galvanostatic charge/discharge behavior of neat TiO_2 and porous carbon/TiO_2 composites from 0.2, 0.3, 0.5, and 0.7 g FA in a potential range of 0.01–2.0 V at a current density of 10 mA/g, (C) Galvanostatic cycling, and (D) Nyquist plots of the porous carbon/TiO_2 composite fabricated using 0.35 g PHEMA (20K)/FA/0.3 g TiO_2 as a function of amount of FA: 0.2 (◇), 0.3 (○), 0.5 (□), and 0.7 g (△).

As the best performance is found using the 20K PHEMA, which has the largest pore size, the mobility of the PHEMA appears to be the controlling factor for determining the morphology of the composites and thus 20K PHEMA is used for examining composition effects on performance. The carbon:TiO_2 ratio can be easily modulated by the FA concentration in the precursor suspension. Figure 4.12A illustrates how the N_2 adsorption–desorption isotherms for the carbon/TiO_2 composites are impacted by the concentration of FA used in their fabrication. At low concentration of FA (0.2 g), the surface area is at a maximum (74.1 m^2/g), but then the surface area increases with increasing amount of FA in the precursor from a minimum of 43.0 (0.3 g) to 63.3 m^2/g (0.7 g). The increase in surface area can be rationalized from the changes in morphology of the carbon/TiO_2 composites (Figure 4.13), where the pore size generally decreases as the FA concentration increases. To explain the maximum in surface area at the lowest FA loading, Figure 4.13A illustrates that the carbon does not fully cover the nanoparticles; these exposed nanoparticles provide significant roughness that increases the surface area. Additionally, the porosity of this sample appears to be larger as evidenced by the enhanced N_2 sorption in the isotherm at high P/P_0. The pores of the carbon/TiO_2 composite are significantly larger for the composite produced using 0.3 g FA (Figure 4.13B) than the carbon/TiO_2 composites from 0.5 g FA (Figure 4.13C) and 0.7 g FA (Figure 4.13D). The Barrett-Joyner-Halenda (BJH) average pore sizes of the different composites using 0.3 g, 0.5 g, and 0.7 g of FA are ~24 nm, ~16 nm, and ~14 nm, respectively. For this series of samples, the TiO_2 nanoparticles are mostly covered by the carbon produced from the FA and thus the surface area scales inversely with pore size as expected (as the volume adsorbed is similar between the samples from Figure 4.12A).

Thus, the morphology of porous carbon/TiO_2 composites pyrolyzed from PHEMA/FA/TiO_2 can also be controlled by the amount of FA used in the synthesis, in addition to the PHEMA molecular weight.

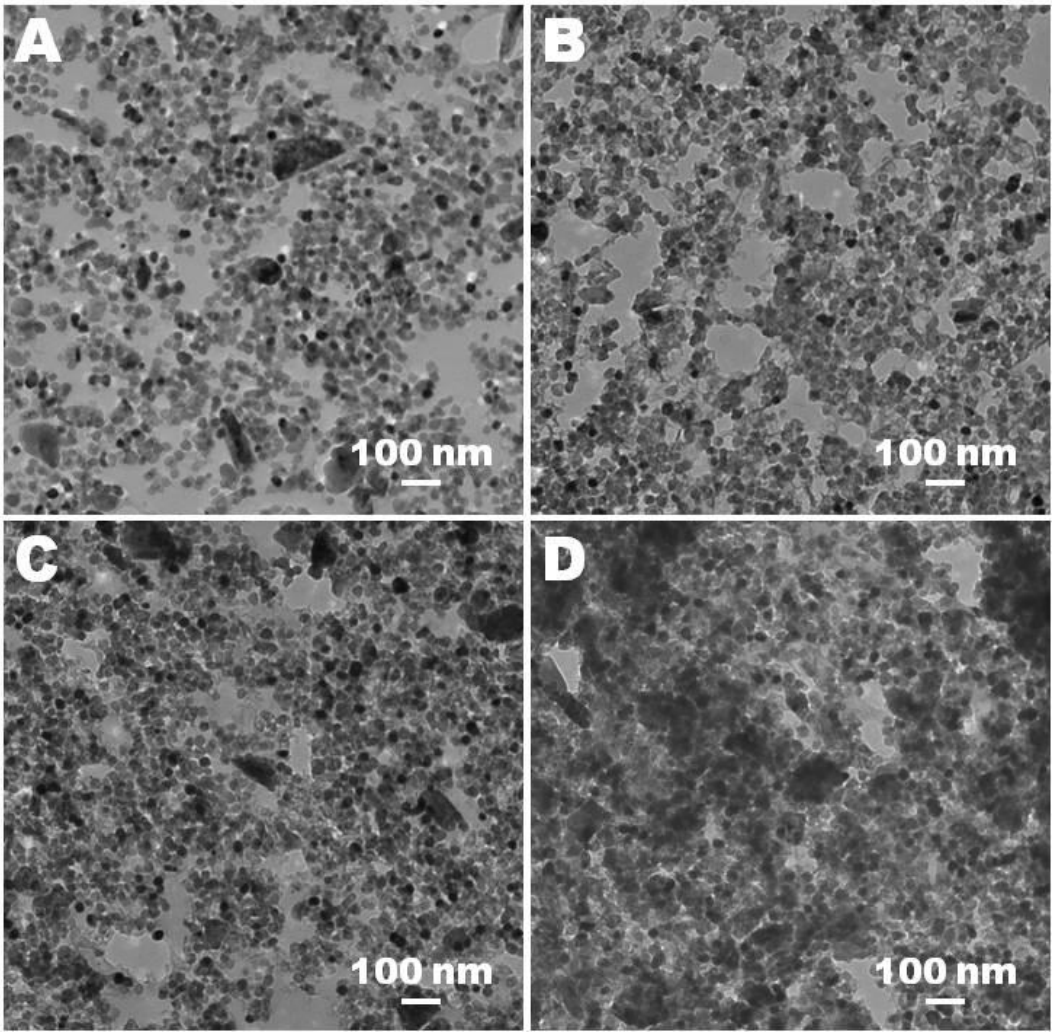

Figure 4.13. TEM micrographs of porous carbon/TiO_2 composites fabricated with 0.35 g PHEMA (20K)/0.3 g TiO_2/FA of (A) 0.2, (B) 0.3, (C) 0.5, and (D) 0.7 g for the precursor.

The galvanostatic charge-discharge curves of porous carbon/TiO_2 composites produced from 0.2, 0.3, 0.5, and 0.7 g of FA are shown in Figure 4.12B with that of neat TiO_2 anode. As with the composite anodes fabricated from different molecular weight of PHEMA, the carbon/TiO_2 composites provide much more stable charge-discharge behavior and higher capacity value compared to neat TiO_2 anode. From this galvanostatic behaviour, the discharge capacity of the porous carbon/TiO_2 composite anodes is obtained.

The change in both the composition of the active carbon/TiO_2 composite anodes and the morphology impacts the capacity as illustrated in Figure 4.12C. As the current density increases from 10 mA/g (about 0.1 C) up to 30 mA/g (about 0.4 C), there is a decrease in the capacity by approximately 25%, irrespective of the composition of the composite. As the theoretical capacity for TiO_2 is greater than that for carbon, increasing the FA content, which provides the carbon yield, generally leads to a decrease in performance. The difference in carbon content is relatively small with the carbon content increasing from 12 to 18 wt% for the composites using 0.2 and 0.7 g FA (see Figure 4.14); there is only a 1 wt% difference in the carbon content between the composite using 0.3 g FA (15 wt% carbon) and 0.5 g FA (16 wt% carbon), but the capacity is significantly different at 10 mA/g (115 mAh/g and 90 mAh/g, respectively). However, there is also a concurrent increase in surface area, which is consistent with the decreased capacity from the molecular weight series (Figure 4.1C). The one exception is for the lowest FA content composite (0.2 g FA), which exhibits slightly lower capacity than the composite fabricated with 0.3 g FA; this material has the lowest carbon

content (12 wt%) and the highest surface area. Two probable reasons for the anomalous performance for this low carbon material are the limited carbon content leads to poor electrical conductivity, which limits the performance, and/or the difference in surface chemistry where more TiO_2 nanoparticles are exposed, which could lead to a different SEI layer that limits Na^+ transport.

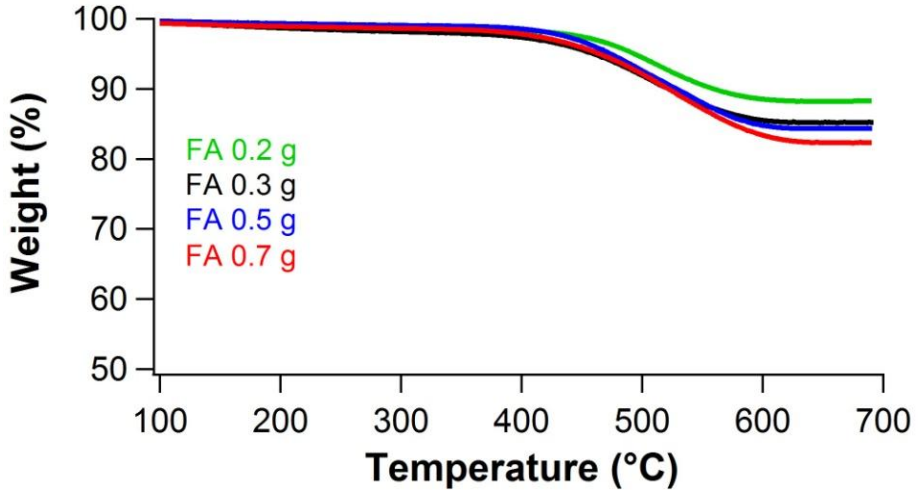

Figure 4.14. TGA curves of carbon/TiO_2 composites with different amount of FA to determine the carbon content by oxidation in air.

To better understand these differences in performance, the EIS spectra of the carbon/TiO_2 composite electrodes after 30 charge-discharge cycles are examined (Figure 4.12D). As the carbon content increases, the impedance decreases at high frequency. The electrode resistance decreases as evidenced by the decrease in the diameter of semi-circle. As the carbon content increases, the slope of the linear regions decreases at low frequencies. It indicates that the Na^+ ion diffusion into the electrode is significantly hindered and the Na^+ ion diffusion path in the electrode becomes longer at the higher carbon content. An electric circuit model for these porous carbon/TiO_2 composite electrodes and numerical values of the equivalent circuit components obtained for the

impedance data are shown in Figure 4.5. To understand the origins for this behavior, the morphology and chemical changes of the cycled composite anodes are investigated by TEM and XPS.

The change of morphology between neat and cycled composites is shown in Figure 4.15. The neat composite anodes (left side in Figure 4.15) contain smaller pores as the amount of FA used in their fabrication increases (as shown in Figure 4.16). The FA content controls the amount of carbon in the composites after pyrolysis of PHBMA/PFA/TiO_2. From the TEM micrographs (right side in Figure 4.15), it is possible to distinguish the low electron density carbon (light), the oxygen-rich SEI layers (darker regions) and the TiO_2 nanoparticles (almost black). Thus generally, the SEI layer content increases as the carbon content of the composite materials increases. However, the lowest carbon content composite anode (Figure 4.15A) appears to exhibit an increased SEI layer (dark spots) like composite anodes with higher carbon loading. We hypothesize that the exposed TiO_2 nanoparticles lead to this increased SEI content. This is consistent with the slight decrease in the slope of the impedance curve for this sample (0.2 g FA) compared to the one with slightly more carbon (0.3 g FA).

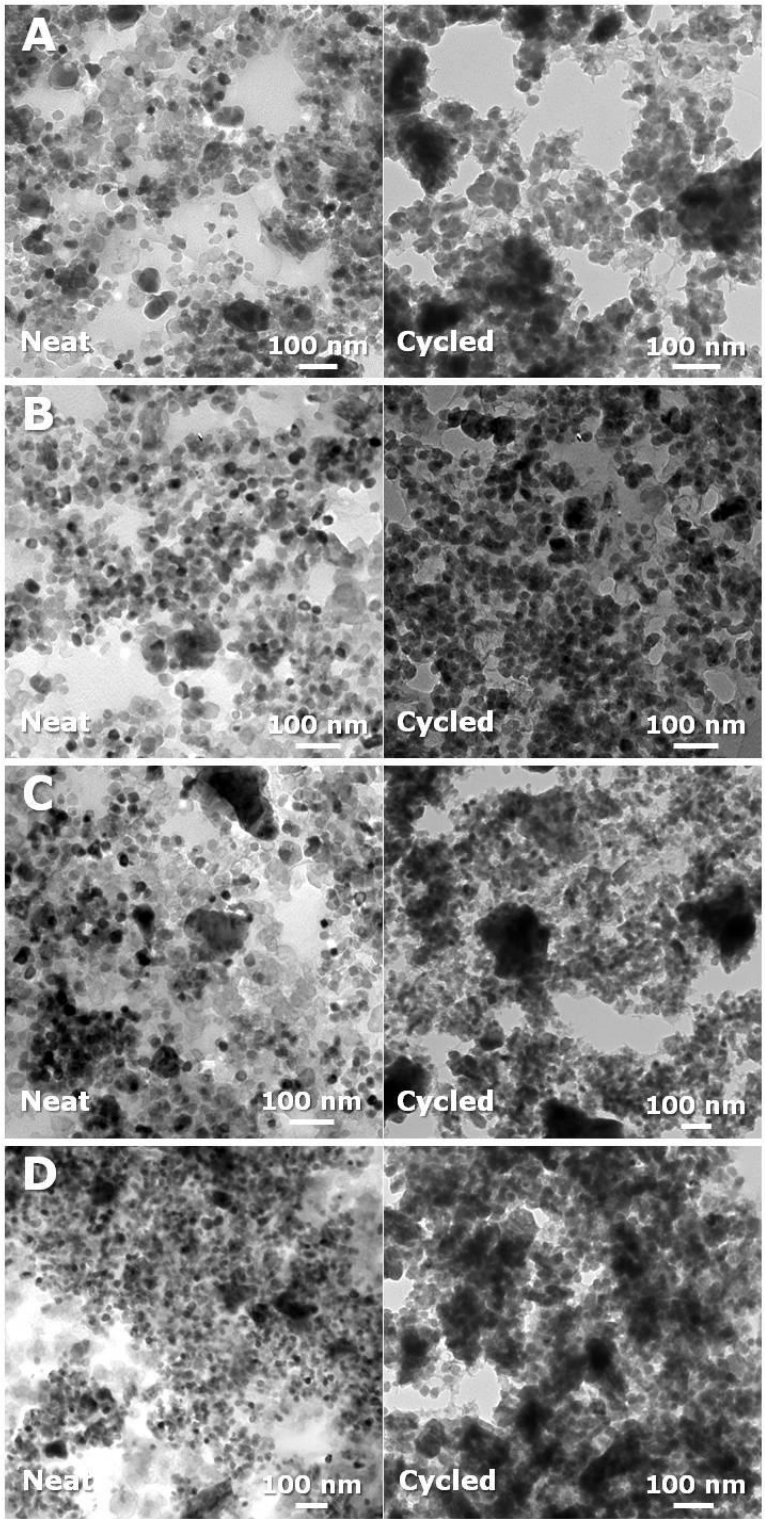

Figure 4.15. TEM images of carbon/TiO_2 composite anodes as-produced (left) and after 30 charge-discharge cycles (right) fabricated with 0.35g PHEMA (20K)/0.3g TiO_2/FA of (A) 0.2 g (12 wt% C), (B) 0.3 g (15 wt% C), (C) 0.5 g (16 wt% C), and (D) 0.7 g (18 wt% C).

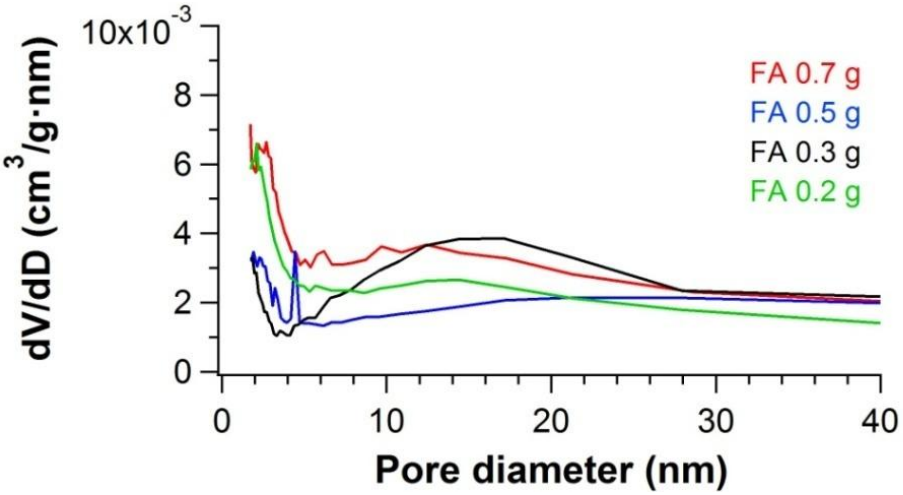

Figure 4.16. Pore size distribution of carbon/TiO_2 composites fabricated with 0.35 g PHEMA (20K)/0.3 g TiO_2/different amount of FA for the precursor.

To further investigate the SEI layer formation, XPS spectra are obtained for the as-produced electrodes and after 30 charge-discharge cycles (as shown in Figure 4.17). Table 4.2 illustrates how the composition changes during cycling due to the formation of SEI layer. The molar ratio of O and Na to C after 30 charge-discharge cycles increases because of the decomposition of a solution of NaClO4 in EC and PC that leads to the SEI layers. Although, at low carbon content (12 wt%), the molar ratio of O and Na to C after 30 charge-discharge cycles increases from 1 : 0.2 : 0 to 1 : 0.9 : 0.5, the change of the O ratio is small compared to other three anodes with 15, 16, and 18 wt% carbon in the anodes. We attribute this difference in the surface composition to the presence of exposed TiO_2 nanoparticles in this low carbon content sample that leads to a different SEI layer, which is consistent with our hypotheses regarding the performance and impedance data for this sample.

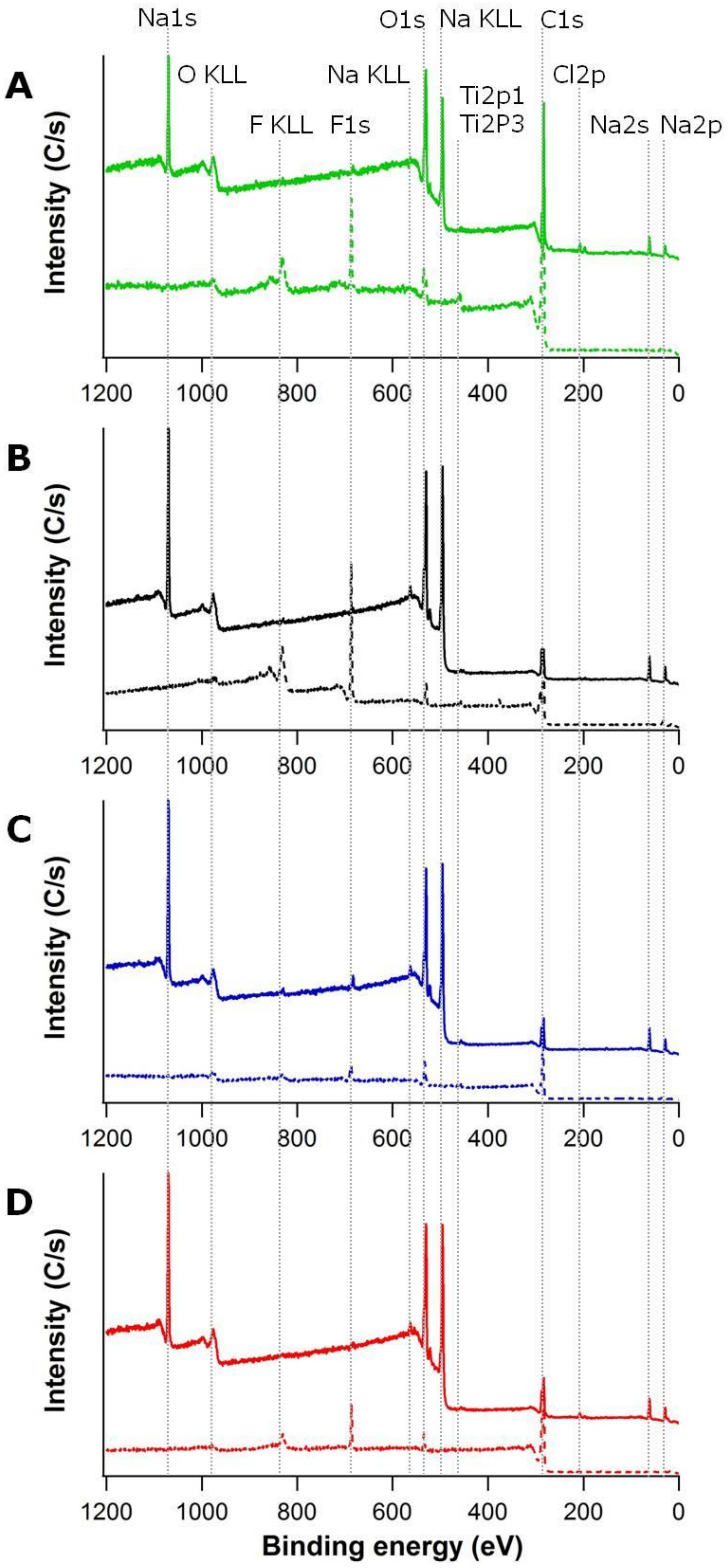

Figure 4.17. XPS spectra of the neat (dash line) and 30 charge-discharge cycled (solid line) composite anodes fabricated with different carbon contents of carbon/TiO_2 composite: (A) 12 wt%, (B) 15 wt%, (C) 16 wt%, and (D) 18 wt%.

Table 4.2. Surface elemental composition from XPS of anodes as-produced and after 30 charge-discharge cycles fabricated with different carbon contents of carbon/TiO_2 composites

Carbon content	As-produced						Cycled					
	C%	O%	Na%	Ti%	Cl%	F%	C%	O%	Na%	Ti%	Cl%	F%
12 wt%	75.8 ± 0.9	17.8 ± 0.6	0	6.4 ± 0.3	0	0.2 ± 0.3	40.6 ± 10.2	35.6 ± 3.9	20.8 ± 6.2	0.1 ± 0.02	2.7 ± 0.6	0.2 ± 0.08
15 wt%	64.3 ± 1.7	20.1 ± 7.2	0	4.6 ± 2.1	0	16.7 ± 0.5	27.1 ± 1.1	42.7 ± 0.9	29.3 ± 1.0	0.1 ± 0.04	0.7 ± 0.04	0.2 ± 0.1
16 wt%	71.5 ± 7.8	20.6 ± 7.5	0	4.1 ± 3.1	0	6.8 ± 2.7	23.5 ± 2.7	41.4 ± 1.1	30.7 ± 1.9	0.2 ± 0.05	0.5 ± 0.4	0.6 ± 0.05
18 wt%	75.2 ± 12.2	15.9 ± 11.2	0	4.8 ± 2.5	0	4.2 ± 3.1	37.7 ± 6.5	39.8 ± 2.7	21.2 ± 3.6	0.1 ± 0.01	1.2 ± 0.05	0.3 ± 0.1

For more study of the SEI layers, high-resolution XPS spectra are used to investigate the 1s binding of C and O, and the resulting spectra of C1s (280-292 eV, left) and O1s (527-539 eV, right) are shown in Figure 4.18. The strong C1s peak at ~284.6 eV is assigned to C-C bonds in SEI layer and the carbon of the electrode composite. The oxygen-rich SEI layer is clearly identified with strong peaks at ~286.2 eV and ~289 eV associated with C-O-C and O-C=O bonds, respectively.[47, 48] The area ratio of C-C bond to carbon-oxygen bonds (C-O-C and O-C=O) decreases from 1 : 1.51 to 1 : 0.78 as the FA content increases, which corresponds to an increase in the carbon content of the anode from 15 wt% to 18 wt% (as shown in Table 4.3). This is unusual as the SEI layer appears to be more prevalent for the higher carbon content anodes from the TEM micrographs (Figure 4.15), but there are less carbon-oxygen bonds near the surface relative to C-C bonds for the high carbon content anodes. This is counter to expectations based on the survey scan (Table 4.2).

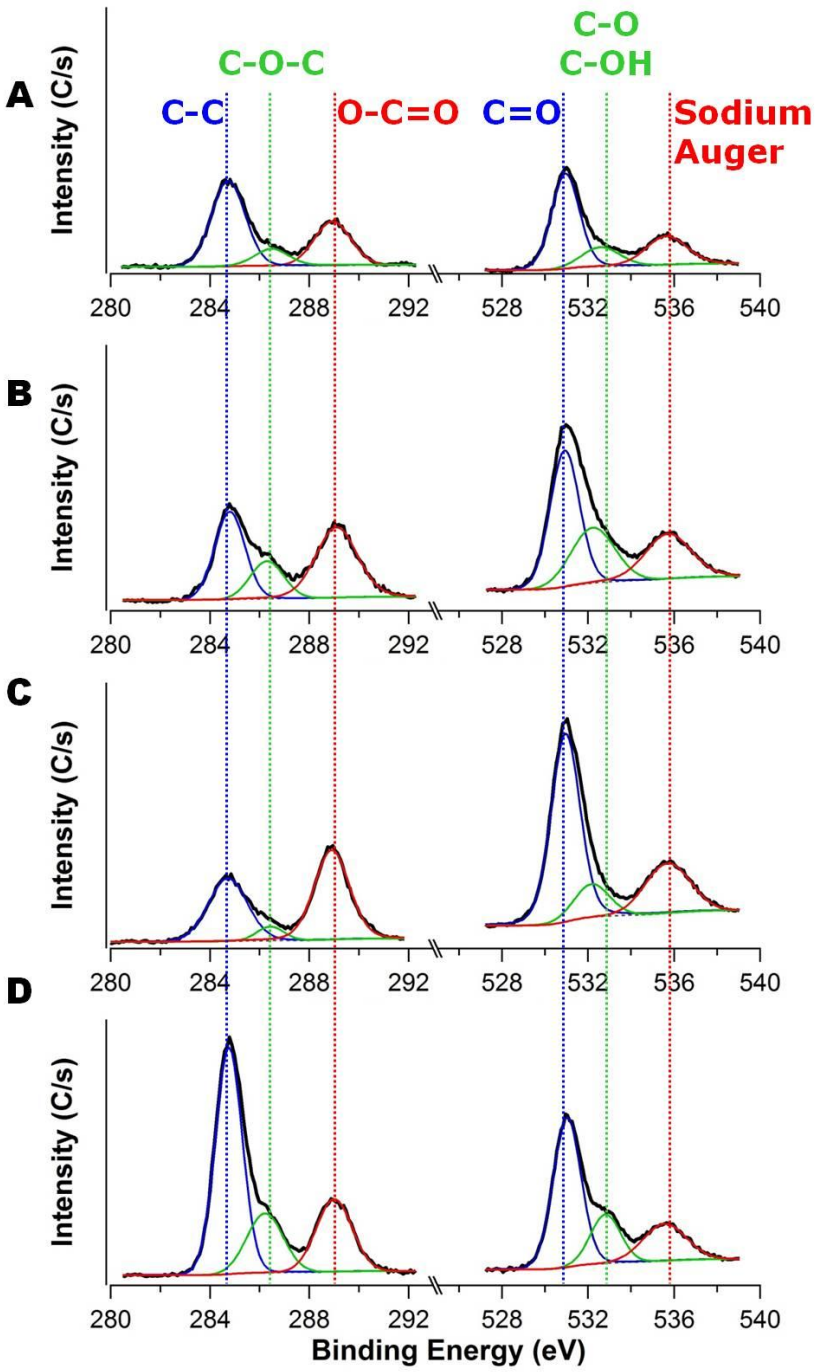

Figure 4.18. XPS spectra examining C1s (left) and O1s (right) for the anodes after 30 charge-discharge cycles fabricated with different carbon contents of carbon/TiO_2 composite: (A) 12 wt%, (B) 15 wt%, (C) 16 wt%, and (D) 18 wt%.

Table 4.3. The changes of peak areas from high resolution XPS spectra as a function of carbon contents in the composite anodes

C1s / Carbon Content	C-C (~284.6 eV)	C-O-C (~286.2 eV)	O-C=O (~289 eV)	C-C : (C-O-C + O-C=O)
12 wt%	57.8 ± 0.6 %	11.1 ± 0.5 %	31.1 ± 0.1 %	1 : 0.73
15 wt%	39.9 ± 2.2 %	21.4 ± 3.6 %	38.7 ± 1.5 %	1 : 1.51
16 wt%	40.6 ± 0.5 %	6.3 ± 0.02 %	53.1 ± 0.5 %	1 : 1.46
18 wt%	56.3 ± 0.01 %	19.5 ± 0.1 %	24.2 ± 0.01 %	1 : 0.78
O1s / Carbon Content	C=O (~531 eV)	C-O, C-OH (~532.8 eV)	Na Auger (~535.5 eV)	(C=O + C-O, C-OH) : Na Auger
12 wt%	58.8 ± 1.2 %	14.8 ± 1.6 %	26.5 ± 0.3 %	1 : 0.37
15 wt%	64.6 ± 0.4 %	10.9 ± 1.0 %	24.4 ± 0.6 %	1 : 0.32
16 wt%	63.9 ± 1.3 %	11.0 ± 2.1 %	23.6 ± 1.3 %	1 : 0.31
18 wt%	52.1 ± 2.7 %	27.1 ± 3.2 %	20.9 ± 0.5 %	1 : 0.26

However, the lowest carbon content anode with exposed TiO_2 also exhibits a low concentration of oxygenated compounds relative to C-C bonds (Table 4.3), but the oxygen content from the survey scan is the lowest of the composites examined (Table 4.2). To better understand this behavior, high-resolution XPS spectra for O1s is investigated between 530 and 534 eV to identify C=O (~531 eV), C-O (~532.5 eV), and C-OH (~533 eV).[50] As the carbon content increases (except for the low carbon, 12 wt%, outlier), the peak area of C=O decrease from 64.6% to 52.1%, whereas the peak areas of C-O and C-OH increase from 10.9% to 27.1%, all on the basis of the total area for the oxygen peaks. These data are consistent with the increased decomposition of the electrolyte (EC and PC) for the higher carbon content specimens as the C=O bonds in EC and PC are reduced to C-O.[49] These XPS data focused on O1s provide an additional advantage to understand the SEI layer formation as the Na auger is visible in the energy window examined. The nature of the SEI layer formed on carbons depends on the location: the basal plane, which consists of sp^2 carbon atoms (C-C bonds), typically generates SEI that is rich in organic compounds, whereas the edge sites, which contain

dandling bonds and various capping moieties (e.g., hydrogen, hydroxyl, carbonyl and carboxyl groups), typically generates SEI that is rich in inorganic compounds.[51, 52] Table 4.3 illustrates the change of the ratio between oxygen-rich substances (C=O, C-O, and C-OH peaks) and sodium (Na Auger peak) as a function of the carbon content after 30 charge-discharge cycles. This ratio is the largest for the lowest carbon content (1:0.37) and decreases to a minimum at the highest carbon content (1:0.26). We attribute this difference to the propensity of organic-rich SEI to form on the basal plane of carbon, so the higher carbon content (18 wt%) should lead to additional SEI.

These results illustrate the interplay between surface area, composition, surface chemistry and pore size on determining the performance of anatase TiO_2-carbon composite anodes for sodium ion batteries. In particular, these factors impact the SEI layer formation. Higher surface areas of the composite materials lead to thicker SEI layers, while increasing the carbon content of the composite also generates thicker SEI layers. The SEI layer thickness can adversely impact the long-term performance of the anodes with a decrease in capacity and an increase in impedance.

4.4 Conclusions

The morphology of porous carbon/TiO_2 composites was tuned using the composition and molecular weight of the porogen in the precursor via a simple polymerization induced phase separation process using a renewable carbon source (furfuryl alcohol). The SEI layer formation increases on the anode having larger surface area, but the nature of the SEI appears to depend on minor perturbations in the composition of the anode. The composite with high carbon content has more sp^2 carbon atoms (C-C bonds) and tends to produce a thick SEI layer that consists of primarily organic compounds (oxygen-rich substances). This thick SEI layer limits sodium ion diffusion and impacts performance with an increase in the impedance and decreases in capacity as the carbon content in the composites increases. This simple polymerization induced phase separation method provides a facile route to teasing out how seemingly minor changes in composition and morphology impact the performance. This method could provide a route to help to better design electrode materials for sodium ion batteries by understanding interplay between structure and performance.

CHAPTER V

GENERAL CONCLUSIONS AND SUGGESTIONS FOR FUTURE STUDY

5.1 Conclusions

During this Ph.D. period, my studies were focused on fabrication and characterization of polymer/metal oxide nanocomposite materials through polymerization-induced phase separation. The nanocomposite materials were studied their mechanical properties depending on their morphology, and they were pyrolyzed to fabricate porous carbon/metal oxide for application to anode electrodes of sodium ion batteries.

The dispersion state of Al_2O_3 in the PEA/PMMA blend matrix has a decisive effect on mechanical properties of PEA/PMMA/Al_2O_3 composite materials. The small-sized clusters and individual clusters of Al_2O_3 into the composites improve the tensile strength as compared with neat PEA/PMMA blend due to interactions between the polymer chains and Al_2O_3 nanoparticles. On the other hand, the larger and interconnected clusters of Al_2O_3 bring several partial failures under relatively low strain as the polymer matrix separates along Al_2O_3 clusters because of the severe modulus mismatch between polymer and Al_2O_3 nanoparticles, and thus they cause the reduction of ductile behavior.

The method used to fabricate porous carbon/TiO_2 composite provides a route to generate a low cost carbon/TiO_2 composite for the active component for the anode electrode of a sodium ion battery. The composite exhibits excellent cycle performance with less than 10% fade in capacitance observed even at high charge/discharge rates up to approximately 5 C (440 mA/g). This simple phase separation method for generating controlled porosity in carbon composites may be applied to other nanoparticle/polymer systems to generate materials for sodium-ion battery electrodes.

The morphology of porous carbon/TiO_2 composites was tuned using the composition and molecular weight of the porogen in the precursor via a simple polymerization induced phase separation process using a renewable carbon source (furfuryl alcohol). The porous carbon/TiO_2 composites were investigated to confirm the interplay between their morphology, SEI formation and performance for the composite anode electrodes for sodium ion batteries. The SEI layer formation increases on the anode having larger surface area, but the nature of the SEI appears to depend on minor perturbations in the composition of the anode.

5.2 Future studies

Surface area of carbon materials is generally increased by the development of porosity in the bulk of carbon materials, leading to a porous network inside the carbon particle. The controls of the pore size and the pore size distribution (PSD) are important because they have a great impact on the carbon capacitance. Therefore, polymer fibers with co-continuous phase morphology between carbon precursor and thermally decomposable polymers are at the center of attention in future study because they can

turn into carbon fibers with large surface area after carbonization. Carbon precursor polymers such as polyacrylonitrile (PAN), poly(vinyl alcohol) (PVA), and polyimide (PI) will be applied to the electrospinning system with various ratios to poly(methyl methacrylate) (PMMA, a thermally decomposable polymer) to find co-continuous morphology as shown in Figure 5.1.

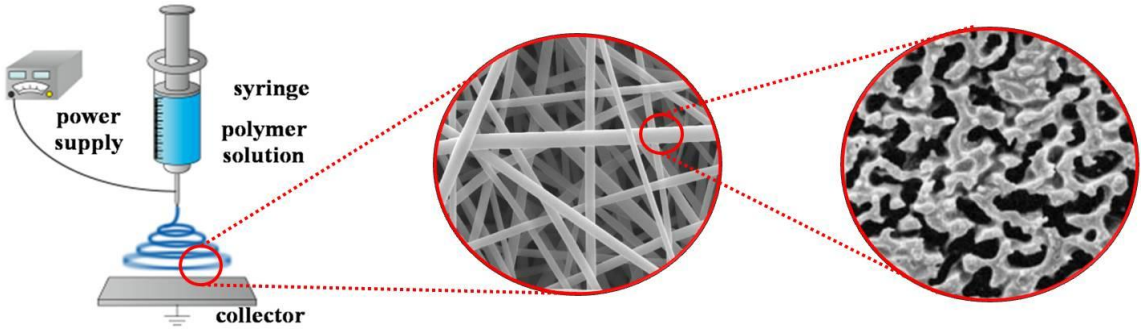

Figure 5.1. A concept image of carbon fiber with co-continuous phase morphology.

Metal oxides are considered to be good candidates as electrode materials in energy storage devices due to their large theoretical capacity (500-1000 mAh/g), which may dramatically improve the energy density for the devices compared to carbon materials. Therefore, hybrid composite electrode systems combining nanostructured carbons with metal oxides can achieve the high performance (high energy and power densities) of electrodes. Among metal oxides, Co_3O_4, SnO_2, V_2O_5, and Fe_3O_4 are attracting attention in future study because of their relatively low cost, ease of synthesis and their different capacitances (shown in Figure 5.2). The difference of their capacitances provides that we can compare the effect the capacitance on the performance of electrodes.

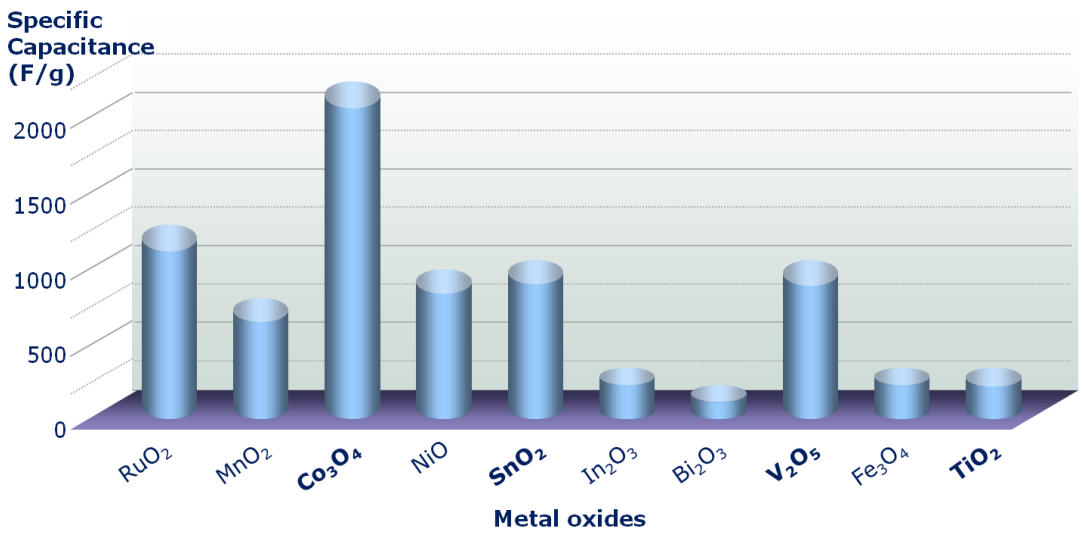

Figure 5.2. The specific capacitance values for different metal oxides.

To improve the electronic conductivity of carbon materials, they are modified with nitrogen-containing functional groups. The nitrogen-containing functional groups can provide the improved capacitance through the pseudo-capacitance effects and the improved wettability of carbon materials with electrolytes. Furthermore, the electronic conductivity of carbon materials can increase through the nitrogen doping, and the improved electronic conductivity can provide the high power density. Therefore, in future study, the nitrogen doped carbon materials will be prepared by heat treatment of the porous carbon materials in a furnace at 900ºC for 1 hr in gas mixture of NH_3 and N_2 (1:4 v/v) as depicted in Figure 5.3.

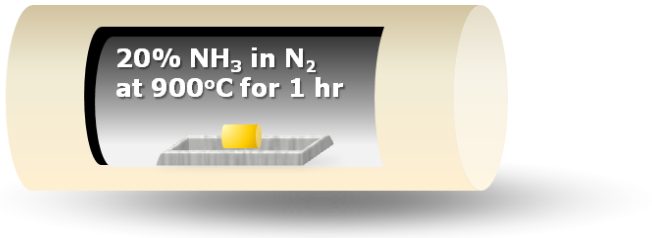

Figure 5.3. A schematic illustration of nitrogendoped carbon materials preparation.

REFERENCES

CHAPTER I

(1) Li, G.; Shrotriya, V.; Huang, J.; Yao, Y.; Moriarty, T.; Emery, K.; Yang, Y., High-efficiency solution processable polymer photovoltaic cells by self-organization of polymer blends, *Nature Materials* **2005**, 4,864-868.

(2) Bockstaller, M. R.; Thomas, E. L., Nanostructures from phase separated polymers, Dekker Encyclopedia of Nanoscience and Nanotechnology 2nd Edition- 6 Volume (edited by Contescu, C. I.; Putyera, K.), CRC Press **2008**, 3093-3108.

(3) Sperling, L. H., Introduction to physical polymer science 4th Ed., John Wiley & Sons **2005**, 145-156.

(4) Ougizawa, T.; Inoue, T., UCST and LCST behavior in polymer blends and its thermodynamic interpretation, *Polymer Journal* **1986**, 18, 521-527.

(5) Roe, R., Zin, W., Determination of the polymer-polymer interaction parameter for the polystyrene-polybutadiene pair, *Macromolecules* **1980**, 13, 1221-1228.

(6) Zacharius, S. L.; Brinke, G.; MacKnight, W. J.; Karasz, F. E., Evidence for critical double points in blends of polystyrene and poly(o-chlorostyrene), *Macromolecules* **1983**, 16, 381-387.

(7) Patterson, D., Free volume and polymer solubility. A qualitative view, *Macromolecules* **1969**, 2, 672-677.

(8) Cahn, J. W.; Hilliard, J. E., Free energy of a nonuniform system. III. Nucleation in a two-component incompressible fluid, *The Journal of Chemical Physics* **1959**, 31, 688-699.

(9) Robeson, L., Polymer blends: A comprehensive review (edited by Roberson L. M.), Hanser Publications **2007**.

(10) Walsh, D. J.; Rostami, S., Binodal and spinodal curves: A simulation for various high polymer mixtures, *Polymer* **1985**, 26, 418-422.

(11) Bockstaller, M. R.; Thomas, E. L., Nanostructures derived from phase-separated polymers, Dekker Encyclopedia of Nanoscience and Nanotechnology, Taylor & Francis **2007**.

(12) Nesterov, A. E.; Lipatov, Y. S., Thermodynamics of Polymer Blends: Polymer Thermodynamics Library (Vol 1), Technomic Publishing **1998**, 275-277.

(13) Thomas, S.; Grohens, Y.; Jyotishkumar, P., Characterization of Polymer Blends: Miscibility, Morphology and Interfaces, Wiley-VCH Verlag GmbH & Co. **2015**, 584.

(14) Rathi, P.; Huang, T. M.; Dayal, P.; Kyu, T., Crystalline-amorphous interaction in relation to the phase diagrams of binary polymer blends containing a crystalline constituent, *The Journal of Physical Chemistry B* **2008**, 112, 6460-6466.

(15) Qiu, Z. B.; Yang, W. T., Crystallization kinetics and morphology of poly(butylene succinate)/poly(vinyl phenol) blend, *Polymer* **2006**, 47, 6429-6437.

(16) Li, J.; Li, W.; Cheng, H.; Zhang, L.; Li, Y.; Han, C. C., Early stages of nucleation and growth in melt crystallized polyethylene, *Polymer* **2012**, 53, 2315-2319.

(17) Mark, H. F., Encyclopedia of Polymer Science and Technology, Concise 3rd Ed., John Wiley & Sons, Inc. **2007**, 302-306.

(18) Hiemenz, P. C.; Lodge, T. P., Polymer Chemistry 2nd Ed., CRC Press 2007, 536-544.

(19) Sperling, L. H., Introduction to physical polymer science 4th Ed., John Wiley & Sons **2005**, 260-271.

(20) Benmouna, F.; Bouabdellah-Dembahria, Z.; Benmouna, M., Polymerization-induced phase separation: Phase behavior developments and hydrodynamic interaction, *Journal of Macromolecular Science Part B: Physics* **2013**, 52, 998-1008.

(21) Luo, K., The morphology and dynamics of polymerization-induced phase separation, *European Polymer Journal* **2006**, 42, 1499-1505.

(22) Vaz, N. A.; Smith, G. W.; Montgomery, G. P., A light control film composed of liquid crystal droplets dispersed in a UV-curable polymer, *Molecular Crystals and Liquid Crystals* **1987**, 146, 1-15.

(23) Yagci, Y.; Jockusch, S.; Turro, N. J., Photoinitiated Polymerization: Advances, Challenges, and Opportunities, *Macromolecules* **2010**, 43, 6245-6260.

(24) Kim, J. Y.; Cho, C. H.; Palffy-Muhoray, P.; Kyu, T., Polymerization-induced phase separation in a liquid-crystal-polymer mixture, *Physical Review Letters* **1993**, 71, 2232-2235.

(25) Lee, J.; Ha, J. U.; Choe, S.; Lee, C.; Shim, S. E., Synthesis of highly monodisperse polystyrene microspheres via dispersion polymerization using an amphoteric initiator, *Journal of Colloid and Interface Science* **2006**, 298, 663-671.

(26) Chan, P. K.; Rey, A. D., Polymerization-induced phase separation: 2. Morphological analysis, *Macromolecules* **1997**, 30, 2135-2143.

(27) Liu, Y., Polymerization-induced phase separation and resulting thermomechanical properties of thermosetting/reactive nonlinear polymer blends: A review, *Journal of Applied Polymer Science* **2013**, 127, 3279-3292.

(28) Kwok, A. Y.; Prime, E. L.; Qiao, G. G.; Solomon, D. H., Synthetic hydrogels 2. Polymerization induced phase separation in acrylamide systems, *Polymer* **2003**, 44, 7335-7344.

(29) Jordan, J.; Jacob, K. I.; Tannenbaum, R.; Sharaf, M. A.; Jasiuk, I., Experimental trends in polymer nanocomposites - A review, *Materials Science and Engineering: A* **2005**, 393, 1-11.

(30) Jeon, I.; Baek, J., Nanocomposites derived from polymers and inorganic nanoparticles, *Materials* **2010**, 3, 3654-3674.

(31) Schmidt, G.; Malwitz, M. M., Properties of polymer–nanoparticle composites, *Current Opinion in Colloid and Interface Science* **2003**, 8, 103-108.

(32) Alexandre, M.; Dubois, P., Polymer-layered silicate nanocomposites: preparation, properties and uses of a new class of materials, *Materials Science Engineering: R: Reports* **2000**, 28, 1-63.

(33) Ke, Y.; Long, C.; Qi, Z., Crystallization, properties, and crystal and nanoscale morphology of PET-clay nanocomposites, *Journal of Applied Polymer Science* **1999**, 71, 1139-1146.

(34) Burnside, S. D.; Giannelis, E. P., Synthesis and properties of new poly(dimethylsiloxane) nanocomposites, *Chemistry of Materials* **1995**, 7, 1597-1600.

(35) Jamel, M. M.; Khoshnoud, P.; Gunashekar, S.; Abu-Zahra, N., Enhancement of dimensional stability of rigid PVC foams using E-glass fibers, *Journal of Minerals and Materials Characterization and Engineering* **2015**, 3, 65-75.

(36) Messersmith, P. B.; Giannelis, E. P., Synthesis and barrier properties of poly(ε-caprolactone)-layered silicate nanocomposites, *Journal of Polymer Science Part A: Polymer Chemistry* **1995**, 33, 1047-1057.

(37) Rong, M. Z.; Zhang, M. Q.; Pan, S. L.; Lehmann, B.; Frierich, K., Analysis of the interfacial interactions in polypropylene/silica nanocomposites, *Polymer International* **2004**, 53, 176-183.

(38) Suryanarayana, C; Froes, F. H., The structure and mechanical properties of metallic nanocrystals, *Metallurgical Transctions A* **1992**, 23A, 1071-1081.

(39) Chandra, A.; Turng, L.; Gopalan, P.; Rowell, R. M.; Gong, S., Study of utilizing thin polymer surface coating on the nanoparticles for melt compounding of polycarbonate/alumina nanocomposites and their optical properties, *Composites Science and Technology* **2008**, 68, 768-776.

(40) Peponi, L.; Puglia, D.; Torre, L.; Valentini, L.; Kenny, J. M., Processing of nanostructured polymers and advanced polymeric based nanocomposites, *Materials Science and Engineering: R: Reports* **2014**, 85, 1-46.

(41) Tanahashi, M., Development of fabrication methods of filler/polymer nanocomposites: With focus on simple melt-compounding-based approach without surface modification of nanofillers, *Materials* **2010**, 3, 1593-1619.

(42) Kalaitzidou, K.; Fukushima, H.; Drzal, L. T., A new compounding method for exfoliated graphite–polypropylene nanocomposites with enhanced flexural properties and lower percolation threshold, *Composites Science and Technology* **2007**, 67, 2045-2051.

(43) Preghenella, M.; Pegoretti, A.; Migliaresi, C., Thermo-mechanical characterization of fumed silica-epoxy nanocomposites, *Polymer* **2005**, 46, 12065-12072.

(44) Alexandre, M.; Pluta, M.; Dubois, P.; Jérôme, R., Metallocene catalyzed polymerization of ethylene in the presence of graphite, 1. synthesis and characterization of the composites, *Macromolecular Chemistry and Physics* **2001**, 202, 2239–2246.

(45) Scharlach, K.; Kaminsky, W., New polyolefin-nanocomposites by in situ polymerization with metallocene catalysts, *Macromolecular Symposia* **2008**, 261, 10-17.

(46) Hood, M. A.; Mari, M.; Muñoz-Espí, R., Synthetic strategies in the preparation of polymer/inorganic hybrid nanoparticles, *Materials* **2014**, 7, 4057-4087.

(47) Ver Meer, M. A., Polymer/mesoporous metal oxide composites, Iowa State University (doctoral dissertation) **2010**.

(48) Paul, D. R.; Robeson, L. M., Polymer nanotechnology: Nanocomposites, *Polymer* **2008**, 49, 3187-3204.

(49) State, M.; Brands, P. J.; van de Vosse, F. N., Improving the thermal dimensional stability of flexible polymer composite backing materials for ultrasound transducers, *Ultrasonics* **2010**, 50, 458-466.

(50) Wang, K.; Chen, L.; Wu, J.; Toh, M. L.; He, C.; Yee, A. F., Epoxy nanocomposites with highly exfoliated clay: Mechanical properties and fracture mechanisms, *Macromolecules* **2005**, 38, 788-800.

(51) Pattanayak, A.; Jana, S. C., Properties of bulk-polymerized thermoplastic polyurethane nanocomposites, *Polymer* **2005**, 46, 3394-3406.

(52) Herrera-Franco, P. J.; Valadez-González, A., Mechanical properties of continuous natural fibre-reinforced polymer composites, *Composites: Part A* **2004**, 35, 339-345.

(53) Tsekmes, I. A.; Kochetov, R.; Morshuis, P. H. F.; Smit, J. J., Thermal conductivity of polymeric composites: A review, IEEE International Conference on Solid Dielectric **2013**, 678-681.

(54) Shinde, S. L.; Goela, J. S., High Thermal Conductivity Materials, Springer **2006**.

(55) Ha, S. M.; Lee, H. L.; Lee, S.; Kim, B. G.; Kim, Y. S.; Won, J. C.; Choi, W. J.; Lee, D. C.; Kim, J.; Yoo, Y., Thermal conductivity of graphite filled liquid crystal polymer composites and theoretical predictions, *Composites Science and Technology* **2013**, 88, 113-119.

(56) Wen, S.; Chung, D. D. L., Effects of carbon black on the thermal, mechanical and electrical properties of pitch-matrix composites, *Carbon* **2004**, 42, 2393-2397.

(57) Wang, S.; Chung, D. D. L., Thermal fatigue in carbon fibre polymer-matrix composites, monitored in real time by electrical resistance measurements, *Polymers & Polymer Composites* **2001,** 9, 135-140.

(58) He, H.; Fu, R.; Han, Y.; Shen, Y.; Song, X., Thermal conductivity of ceramic particle filled polymer composites and theoretical predictions, *Journal of Materials Science* **2007**, 42, 6749-6754.

(59) Singh, R.; Sharma, P. K., Effective thermal conductivity of metal filled polymer composites, *Indian Journal of Pure & Applied Physics* **2011**, 49, 112-116.

(60) Su, J.; Xiao, Y.; Ren, M., Enhanced thermal conductivity in epoxy nanocomposites with hybrid boron nitride nanotubes and nanosheets, *Physica Status Solidi A* **2013**, 210, 2699-2705.

(61) Li, Z.; Luo, G.; Wei, F.; Huang, Y., Microstructure of carbon nanotubes/PET conductive composites fibers and their properties, *Composites Science and Technology* **2006**, 66, 1022-1029.

(62) Yang, S.; Lozano, K.; Lomeli, A.; Foltz, H. D.; Jones, R., Electromagnetic interference shielding effectiveness of carbon nanofiber/LCP composites, *Composites Part A: Applied Science and Manufacturing* **2005**, 36, 691-697.

(63) Kachoosangi, R. T.; Musameh, M. M.; Abu-Youse, I.; Yousef, J. M.; Kanan, S. M.; Xiao, L.; Davies, S. G., Russell, A.; Compton, R. G., Carbon nanotube-ionic liquid composite sensors and biosensors, *Analytical Chemistry* **2009**, 81, 435-442.

(64) Wu M. ; Shaw, L. L., A novel concept of carbon-filled polymer blends for applications in PEM fuel cell bipolar plates, *International Journal of Hydrogen Energy* **2005**, 30, 373-380.

(65) Mamunya, Y. P.; Zois, H.; Apekis, L.; Lebedev, E. V., Influence of pressure on the electrical conductivity of metal powders used as fillers in polymer composites, *Powder Technology* **2004**, 140, 49-55.

(66) Bigg, D. M., Mechanical, thermal, and electrical properties of metal fiber-filled polymer composites, *Polymer Engineering & Science* **1979**, 19, 1188-1192.

(67) Horibe, H.; Kamimura, T.; Yoshida, K., Electrical conductivity of polymer composites filled with carbon black, *Japanese Journal of Applied Physics* **2005**, 44, 2025-2029.

(68) Li, Y.; Samad, Y. A.; Polychronopoulou, K.; Alhassan, S. M.; Liao, K., Highly electrically conductive nanocomposites based on polymer-infused graphene sponges, *Scientific Reports* **2014**, 4, 1-6.

(69) Chang, C.; Liu, Y., Electrical conductivity enhancement of polymer/multiwalled carbon nanotube (MWCNT) composites by thermally-induced defunctionalization of MWCNTs, *ACS Applied Material Interfaces* **2011**, 3, 2204-2208.

(70) Guo, W.; Liu, C.; Sun, X.; Yang, Z.; Kia, H. G.; Peng, H., Aligned carbon nanotube/ polymer composite fibers with improved mechanical strength and electrical conductivity, *Journal of Materials Chemistry* **2012**, 22, 903-908.

(71) Camargo, P. H. C.; Satyanarayana, K. G.; Wypych, F., Nanocomposites: Synthesis, structure, properties and new application opportunities, *Materials Research* **2009**, 12, 1-39.

(72) Cuppoletti, J., Nanocomposites and polymers with analytical methods, InTech **2011**, 3-28.

(73) Kango, S.; Kalia, S.; Celli, A.; Njuguna, J.; Habibi, Y.; Kumar, R., Surface modification of inorganic nanoparticles for development of organic-inorganic nanocomposites-A review, *Progress in Polymer Science* **2013**, 38, 1232-1261.

(74) Roy, P.; Srivastava, S. K., Nanostructured anode materials for lithium ion batteries, *Journal of Materials Chemistry A* **2015**, 3, 2454-2484.

(75) Purvins, A.; Sumner, M., Optimal management of stationary lithium-ion battery system in electricity distribution grids, *Journal of Power Sources* **2013**, 242, 742-755.

(76) Hong, S. Y.; Kim, Y.; Park, Y.; Choi, A.; Choi, N.; Lee, K. T., Charge carriers in rechargeable batteries: Na ions vs. Li ions, *Energy & Environmental Science* **2013**, 6, 2067-2081.

(77) Ellis, B. L.; Nazar, L. F., Sodium and sodium-ion energy storage batteries, *Current Opinion in Solid State and Materials Science* **2012**, 16, 168-177.

(78) Kim, S.; Seo, D.; Ma, X.; Ceder, G.; Kang, K., Electrode materials for rechargeable sodium-ion batteries: potential alternatives to current lithium-ion batteries, *Advanced Energy Materials* **2012**, 2, 710-721.

(79) Slater, M. D.; Kim, D.; Lee, E.; Johnson, C. S., Sodium-Ion Batteries, *Advanced Functional Materials* **2013**, 23, 947-958.

(80) Kim, Y.; Kim, Y.; Choi, A.; Woo, S.; Mok, D.; Choi, N.; Jung, Y. S.; Ryu, J. H.; Oh, S. M.; Lee, K. T., Tin phosphide as a promising anode material for Na-ion batteries, *Advanced Materials* **2014**, 26, 4139-4144.

(81) Doeff, M. M.; Ma, Y.; Visco, S. T.; De Jonghe, L. C., Electrochemical Insertion of Sodium into Carbon, *Journal of The Electrochemical Society* **1993**, 140, L169-L170.

(82) Chen, T.; Liu, Y.; Pan, L.; Lu, T.; Yao, Y.; Sun, Z.; Chua, D. H. C.; Chen, Q., Electrospun carbon nanofibers as anode materials for sodium ion batteries with excellent cycle performance, *Journal of Materials Chemistry A* **2014**, 2, 4117-4121.

(83) Ge, P.; Fouletier, M., Electrochemical interaction of sodium in graphite, *Solid State Ionics* **1988**, 28-30, 1172-1175.

(84) Nithya, C.; Gopukumar, S., Sodium ion batteries: a newer electrochemical storage, *WIREs Energy and Environment* **2015**, 4, 253-278.

(85) Alcántara, R.; Jaraba, M.; Lavela, P.; Tirado, J. L., NiCo2O4 spinel: first report on a transition metal oxide for the negative electrode of sodium-ion batteries, *Chemistry of Materials* **2002**, 14, 2847-2848

(86) Jiang, Y.; Hu, M.; Zhang, D.; Yuan, T.; Sun, W.; Xu, B.; Yan, M., Transition metal oxides for high performance sodium ion battery anodes, *Nano Energy* **2014**, 5, 60-66.

(87) Wang, L.; Zhang, K.; Hu, Z.; Duan, W.; Cheng, F.; Chen, J., Porous CuO nanowires as the anode of rechargeable Na-ion batteries, *Nano Research* **2014**, 7, 199-208.

(88) Li, W.; Chou, S.; Wang, J.; Liu, H.; Dou, S., A new, cheap, and productive FeP anode material for sodium-ion batteries, *Chemical Communications* **2015**, 51, 3682-3685.

(89) Wang, J. W.; Liu, X. H.; Mao, S. X.; Huang, J. Y., Microstructural evolution of Tin nanoparticles during in situ sodium insertion and extraction, *Nano Letters* **2012**, 12, 5897-5902.

(90) Cloud, J. E.; Wang, Y.; Yoder, T. S.; Taylor, L. W.; Yang, Y., Colloidal nanocrystals of lithiated group 14 elements, *Angewandte Chemie International Edition* **2014**, 53, 14527-14532.

(91) Qian, J. F.; Chen, Y.; Wu, L.; Cao, Y. L.; Ai, A. P.; Yang, H. X., High capacity Na-storage and superior cyclability of nanocomposite Sb/C anode for Na-ion batteries, *Chemical Communications* **2012**, 48, 7070-7072.

(92) Yamamoto, T.; Nohira, T.; Hagiwara, R.; Fukunaga, A.; Sakai, S.; Nitta, K.; Inazawa, S., Charge–discharge behavior of tin negative electrode for a sodium secondary battery using intermediate temperature ionic liquid sodium bis(fluorosulfonyl)amide–potassium bis(fluorosulfonyl)amide, *Journal of Power Sources* **2012**, 217, 479–484.

(93) Ellis, L. D.; Ferguson, P. P.; Obrovac, M. N., Sodium insertion into tin cobalt carbon active/inactive nanocomposite, *Journal of The Electrochemical Society* **2013**, 160, A869-A872.

(94) Abel, P. R.; Lin, Y.; de Souza, T.; Chou, C.; Gupta, A.; Goodenough, J. B.; Hwang, G. S.; Heller, A.; Mullins, C. B., Nanocolumnar germanium thin films as a high-rate sodium-ion battery anode material, *The Journal of Physical Chemisty C* **2013**, 117, 18885-18890.

(95) Darwiche, A.; Marino, C.; Sougrati, M. T.; Fraisse, B.; Stievano, L.; Monconduit, L., Better cycling performances of bulk Sb in Na-ion batteries compared to Li-ion systems: an unexpected electrochemical mechanism, *Journal of The American Chemical Society* **2012**, 134, 20805-20811.

(96) Wachtler, M.; Besenhard, J. O.; Winter, M., Tin and tin-based intermetallics as new anode materials for lithium-ion cells, *Journal of Power Sources* **2001**, 94, 189-193.

(97) Xiao, L.; Cao, Y.; Xiao, J.; Wang, W.; Kovarik, L.; Nie, Z.; Liu, J., High capacity, reversible alloying reactions in SnSb/C nanocomposites for Na-ion battery applications, *Chemical Communications* **2012**, 48, 3321–3323.

(98) Farbod, B.; Cui, K.; Kalisvaart, W. P.; Kupsta, M.; Zahiri, B.; Kohandehghan, A.; Lotfabad, E. M.; Li, Z.; Luber, E. J.; Mitlin, D., Anodes for sodium ion batteries based on tin–germanium–antimony alloys, *ACS Nano* **2014**, 8, 4415-4429.

(99) Chaudhuri, S.K.; Lovley, D.R., Electricity generation by direct oxidation of glucose in mediatorless microbial fuel cells, *Nature Biotechnology* **2003**, 21, 1229-1232.

(100) Tsai, H.; Wu, C.; Lee, C.; Shih, E. P., Microbial fuel cell performance of multiwall carbon nanotubes on carbon cloth as electrodes, *Journal of Power Sources* **2009**, 194, 199-205.

(101) Sanchez, D. V. P.; Jacobs, D.; Gregory, K.; Huang, J.; Hu, Y.; Vidic, R.; Yun, M., Changes in carbon electrode morphology affect microbial fuel cell performance with shewanella oneidensis MR-1, *Energies* **2015**, 8, 1817-1829.

(102) Collinson, M. M., Nanoporous gold electrodes and their applications in analytical chemistry, *ISRN Analytical Chemistry* **2013**, 2013, 1-21.

(103) Tang, K.; Fu, L.; White, R. J.; Yu, L.; Titirici, M.; Antonietti, M.; Maier, J., Hollow carbon nanospheres with superior rate capability for sodium-based batteries, *Advanced Energy Materials* **2012**, 2, 873-877.

(104) Wang, K.; Li, Z.; Wang, Y.; Liu, H.; Chen, J.; Holmes, J.; Zhou, H., Carbon nanocages with nanographene shell for high-rate lithium ion batteries, *Journal of Materials Chemistry* **2010** , 20 , 9748-9753.

(105) Wenzel, S.; Hara, T.; Janek, J.; Adelhelm, P., Room-temperature sodium-ion batteries: Improving the rate capability of carbon anode materials by templating strategies, *Energy & Environmental Science* **2011**, 4, 3342-3345.

(106) Wang, H.; Wu, Z.; Meng, F.; Ma, D.; Huang, X.; Wang, L.; Zhang, X., Nitrogen-doped porous carbon nanosheets as low-cost, high-performance anode material for sodium-ion batteries, *ChemSusChem* **2013**, 6, 56-60.

(107) Ein-Eli, Y., A new perspective on the formation and structure of the solid electrolyte interface at the graphite anode of Li-ion cells, *Electrochemcal and Solid-State Letters* **1999**, 2, 212-214.

(108) Luo, W.; Bommier, C.; Jian, Z.; Li, X.; Carter, R.; Vail, S.; Lu, Y.; Lee, J.; Ji, X., Low-surface-area hard carbon anode for Na-ion batteries via graphene oxide as a dehydration agent, *ACS Applied Materials & Interfaces* **2015**, 7, 2626-2631.

(109) Agubra, V. A.; Fergus, J. W., The formation and stability of the solid electrolyte interface on the graphite anode, *Journal of Power Sources* **2014**, 268, 153-162.

(110) Peled, E., The electrochemical behavior of alkali and alkaline earth metals in nonaqueous battery systems - the solid electrolyte interphase model, *Journal of The Electrochemical* **1979**, 126, 2047-2051.

(111) Ushirogata, K.; Sodeyama, K.; Okuno, Y.; Tateyama, Y., Additive effect on reductive decomposition and binding of carbonate-based solvent toward solid electrolyte interphase formation in lithium-ion battery, *Journal of the American Chemical Society* **2013**, 135, 11967-11974.

(112) Ganesh, P.; Kent, P. R. C.; Jiang, D., Solid−electrolyte interphase formation and electrolyte reduction at Li-ion battery graphite anodes: Insights from first-principles molecular dynamics, *Journal of Physical Chemistry C* **2012**, 116, 24476-24481.

(113) Lee, J. T.; Nitta, N.; Benson, J.; Magasinski, A.; Fuller, T. F.; Yushin, G., Comparative study of the solid electrolyte interphase on graphite in full Li-ion battery cells using X-ray photoelectron spectroscopy, secondary ion mass spectrometry, and electron microscopy, *Carbon* **2013**, 52, 388-397.

(114) Chan, C. K.; Ruffo, R.; Hong, S. S.; Cui, Y., Surface chemistry and morphology of the solid electrolyte interphase on silicon nanowire lithium-ion battery anodes, *Journal of Power Sources* **2009**, 189, 1132-1140.

(115) Dang, F.; Oaki, Y.; Kokubu, T.; Hosono, E.; Zhou, H.; Imai, H., Formation of nanostructured MnO/Co/solid–electrolyte interphase ternary composites as a durable anode material for lithium-ion batteries, *Chemistry An Asian Journal* **2013**, 8, 760-764.

(116) Winter, M.; Novak, P.; Monnier, A., Graphites for lithium-ion cells: the correlation of the first-cycle charge loss with the Brunauer-Emmett-Teller surface area, *Journal of The Electrochemical* **1998**, 145, 428-436.

(117) Zheng, T.; Gozdz,A. S.; Amatucci, G. G., Reactivity of the solid electrolyte interface on carbon electrodes at elevated temperatures, *Journal of The Electrochemical Society* **1999**, 146, 4014-4018.

CHAPTER II

(1) Chen, B.; Evans, J. R. G., Mechanical properties of polymer-blend nanocomposites with organoclays: polystyrene/ABS and high impact polystyrene/ABS, *Journal of Polymer Science: Part B: Polymer Physics* **2011**, 49, 443-454.

(2) Veenstra, H.; Verkooijen, P. C. J.; van Lent, B. J. J.; van Dam, J.; de Boer, A. P.; Nijhof, A., On the mechanical properties of co-continuous polymer blends: experimental and modeling, *Polymer* **2000**, 41, 1817-1826.

(3) Inoue, T., Reaction-induced phase decomposition in polymer blends, *Progress in Polymer Science* **1995**, 20, 119-153.

(4) Quintens, D.; Groeninckx, G.; Guest, M.; Aerts, L., Mechanical-behavior related to the phase morphology of PC/SAN polymer blends, *Polymer Engineering and Science* **1990**, 30, 1474-1483.

(5) Benmouna, F.; Bouabdellah-Dembahri, Z.; Benmouna, M., Polymerization-induced phase separation: phase behavior developments and hydrodynamic interaction, *Journal of Macromolecular Science, Part B* **2013**, 52, 998-1008.

(6) Liu, Y., Polymerization-induced phase separation and resulting thermomechanical properties of thermosetting/reactive nonlinear polymer blends: a review, *Journal of Applied Polymer Science* **2013**, 127, 3279-3292.

(7) Tjong, S. C., Structural and mechanical properties of polymer nanocomposites, *Materials Science and Engineering: R* **2006**, 53, 73-197.

(8) Arash, B.; Wang, Q.; Varadan, V. K., Mechanical properties of carbon nanotube/polymer composites, *Scientific Reports* **2014**, 4.

(9) Chapman, R.; Mulvaney, P., Electro-optical shifts in silver nanoparticle films, *Chemical Physics Letters* **2001**, 349, 358-362.

(10) Wilson, O.; Wilson, G. J.; Mulvaney, P., Laser writing in polarized silver nanorod films, *Advanced Materials* **2002**, 14, 1000-1004.

(11) Jeon, I.; Baek, J., Nanocomposites derived from polymers and inorganic nanoparticles, *Materials* **2010**, 3, 3654-3674.

(12) Sim, L. C.; Ramanan, S. R.; Ismail, H.; Seetharamu, K. N.; Goh, T. J., Thermal characterization of Al_2O_3 and ZnO reinforced silicone rubber as thermal pads for heat dissipation purposes, *Thermochimica Acta* **2005**, 430, 155-165.

(13) de Salazar, J. M. G.; Barrena, M. I.; Morales, G.; Matesanz, L.; Merino, N., Compression strength and wear resistance of ceramic foams-polymer composites, *Materials Letters* **2006**, 60, 1687-1692.

(14) Bora, M. O.; Coban, O.; Avcu, E.; Fidan, S.; Sinmazcelik, T., The effect of TiO_2 filler content on the mechanical, thermal, and tribological properties of TiO_2/PPS composites, *Polymer Composites* **2013**, 34, 1591-1599.

(15) Zhou, W., Thermal and dielectric properties of the AlN particles reinforced linear low-density polyethylene composites, *Thermochimica Acta* **2011**, 512, 183-188.

(16) Asi, O., Mechanical properties of glass-fiber reinforced epoxy composites filled with Al_2O_3 particles, *Journal of Reinforced Plastics and Composites* **2009**, 28, 2861-2867.

(17) Mallakpour, S.; Dinari, M., Enhancement in thermal properties of poly(vinyl alcohol) nanocomposites reinforced with Al_2O_3 nanoparticles, *Journal of Reinforced Plastics and Composites* **2013**, 32, 217-224.

(18) Zhi, C. Y.; Bando, Y.; Wang, W. L.; Tang, C. C.; Kuwahara, H.; Golberg, D., Mechanical and thermal properties of polymethyl methacrylate-BN nanotube composites, *Journal of Nanomaterial*s **2008**.

(19) Tong, X.; Zhao, H. C.; Tang, T.; Feng, Z. L.; Huang, B. T., Preparation and characterization of poly(ethyl acrylate)/bentonite nanocomposites by in situ emulsion polymerization, *Journal of Polymer Science: Part A: Polymer Chemistry* **2002**, 40, 1706-1711.

(20) Saadatfar, M.; Khatibi, A. A.; Mortazavi, B., Effective parameters on the stress-strain curve of nylon 66/clay nanocomposite using FEM, *Strain* **2011**, 47, E442-E446.

(21) Bikiaris, D. N.; Vassiliou, A.; Pavlidou, E.; Karayannidis, G. P., Compatibilisation effect of PP-g-MA copolymer on iPP/SiO_2 nanocomposites prepared by melt mixing, *European Polymer Journal* **2005**, 41, 1965-1978.

(22) Mirjalili, F.; Chuah, L.; Salahi, E., Mechanical and morphological properties of polypropylene/nano alpha-Al_2O_3 composites, *The Scientific World Journal* **2014**, 2014, 718765-718765.

(23) Khalid, M.; Ratnam, C. T.; Luqman, C. A.; Salmiaton, A.; Choong, T. S. Y.; Jalaludin, H., Thermal and dynamic mechanical behavior of cellulose- and oil palm empty fruit bunch (OPEFB)-filled polypropylene biocomposites, *Polymer-Plastics Technology and Engineering* **2009**, 48, 1244-1251.

(24) Reynaud, E.; Jouen, T.; Gauthier, C.; Vigier, G.; Varlet, J., Nanofillers in polymeric matrix: a study on silica reinforced PA6, *Polymer* **2001**, 42, 8759-8768.

(25) Mai, K. C.; Li, Z. J.; Qiu, Y. X.; Zeng, H. M., Mechanical properties and fracture morphology of Al(OH)(3)/polypropylene composites modified by PP crafting with acrylic acid, *Journal of Applied Polymer Science* **2001**, 80, 2617-2623.

(26) Qiu, W. L.; Zhang, F. R.; Endo, T.; Hirotsu, T., Preparation and characteristics of composites of high-crystalline cellulose with polypropylene: effects of maleated polypropylene and cellulose content, *Journal of Applied Polymer Science* **2003**, 87, 337-345.

(27) Fu, J.; Naguib, H. E., Effect of nanoclay on the mechanical properties of PMMA/clay nanocomposite foams, *Journal of Cellular Plastics* **2006**, 42,325-342.

CHAPTER III

(1) Goodenough, J. B., Rechargeable batteries: challenges old and new, *Journal of Solid State Electrochemistry* **2012**, 16, 2019-2029.

(2) Dunn, B.; Kamath, H.; Tarascon, J. M., Electrical energy storage for the grid: a battery of choices, *Science* **2011**, 334, 928-935.

(3) Van den Bossche, P.; Vergels, F.; Van Mierlo, J.; Matheys, J.; Autenboer, W., SUBAT: An assessment of sustainable battery technology, *Journal of Power Sources* **2006**, 162, 913-919.

(4) Cheng, F. Y.; Liang, J.; Tao, Z. L.; Chen, J., Functional materials for rechargeable batteries, *Advanced Materials* **2011**, 23, 1695-1715.

(5) Tarascon, J. M.; Armand, M., Issues and challenges facing rechargeable lithium batteries, *Nature* **2001**, 414, 359-367.

(6) Goodenough, J. B.; Kim, Y., Challenges for rechargeable Li batteries, *Chemistry of Materials* **2010**, 22, 587-603.

(7) Song, M.-K.; Park, S.; Alamgir, F. M.; Cho, J.; Liu, M., Nanostructured electrodes for lithium-ion and lithium-air batteries: the latest developments, challenges, and perspectives, *Materials Science & Engineering R* **2011**, 72, 203-252.

(8) Kim, J.; Lee, D. J.; Jung, H. G.; Sun, Y. K.; Hassoun, J.; Scrosati, B., An advanced lithium-sulfur battery, *Advanced Functional Materials* **2013**, 23, 1076-1080.

(9) Shcherbakova, A.; Kleit, A.; Cho, J., The value of energy storage in South Korea's electricity market: a hotelling approach, *Applied Energy* **2014**, 125, 93-102.

(10) Palomares, V.; Casas-Cabanas, M.; Castillo-Martinez, E.; Han, M. H.; Rojo, T., Update on Na-based battery materials. A growing research path, *Energy & Environmental Science* **2013**, 6, 2312-2337.

(11) Slater, M. D.; Kim, D.; Lee, E.; Johnson, C. S., Sodium-ion batteries. *Advanced Functional Materials* **2013**, 23, 947-958.

(12) Doeff, M. M.; Cabana, J.; Shirpour, M., Titanate anodes for sodium ion batteries, *Journal of Inorganic and Organometallic Polymers and Materials* **2014**, 24, 5-4.

(13) Hueso, K. B.; Armand, M.; Rojo, T., High temperature sodium batteries: status, challenges and future trends, *Energy & Environmental Science* **2013**, 6, 734-749.

(14) Hong, S. Y.; Kim, Y.; Park, Y.; Choi, A.; Choi, N. S.; Lee, K. T., Charge carriers in rechargeable batteries: Na ions vs. Li ions, *Energy & Environmental Science* **2013**, 6, 2067-2081.

(15) Alcantara, R.; Jaraba, M.; Lavela, P.; Tirado, J. L., $NiCo_2O_4$ spinel: first report on a transition metal oxide for the negative electrode of sodium-ion batteries, *Chemistry of Materials* **2002**, 14, 2847-2848.

(16) Stevens, D. A.; Dahn, J. R., High capacity anode materials for rechargeable sodium-ion batteries, *Journal of the Electrochemical Society* **2000**, 147, 1271-1273.

(17) Cha, H. A.; Jeong, H. M.; Kang, J. K., Nitrogen-doped open pore channeled graphene facilitating electrochemical performance of TiO_2 nanoparticles as an anode material for sodium ion batteries, *Journal of Materials Chemistry A* **2014**, 2, 5182-5186.

(18) Datta, D.; Li, J. W.; Shenoy, V. B., Defective graphene as a high-capacity anode material for Na- and Ca-ion batteries, *ACS Applied Materials & Interfaces* **2014**, 6, 1788-1795.

(19) Liu, W.; Li, H.; Xie, J. Y.; Fu, Z. W., Rechargeable room-temperature CF_x-sodium battery, *ACS Applied Materials & Interfaces* **2014**, 6, 2209-2212.

(20) Lu, Y. H.; Wang, L.; Cheng, J. G.; Goodenough, J. B., Prussian blue: a new framework of electrode materials for sodium batteries, *Chemical Communications* **2012**, 48, 6544-6546.

(21) Wu, L. M.; Buchholz, D.; Bresser, D.; Chagas, L. G.; Passerini, S., Anatase TiO_2 nanoparticles for high power sodium-ion anodes, *Journal of Power Sources* **2014**, 251, 379-385.

(22) Xiong, H.; Slater, M. D.; Balasubramanian, M.; Johnson, C. S.; Rajh, T., Amorphous TiO_2 nanotube anode for rechargeable sodium ion batteries, *Journal of Physical Chemisty Letters* **2011**, 2, 2560-2565.

(23) Pan, H. L.; Lu, X.; Yu, X. Q.; Hu, Y. S.; Li, H.; Yang, X. Q.; Chen, L. Q., Sodium storage and transport properties in layered $Na_2Ti_3O_7$ for room-temperature sodium-ion batteries, *Advanced Energy Materials* **2013**, 3, 1186-1194.

(24) Kim, H. S.; Yu, S. H.; Sung, Y. E.; Kang, S. H. Carbon treated self-ordered TiO_2 nanotube arrays with enhanced lithium-ion intercalation performance, *Journal Alloys and Compounds* **2014**, 597, 275-281.

(25) Bi, Z. H.; Paranthaman, M. P.; Menchhofer, P. A.; Dehoff, R. R.; Bridges, C. A.; Chi, M. F.; Guo, B. K.; Sun, X. G.; Dai, S., Self-organized amorphous TiO_2 nanotube arrays on porous Ti foam for rechargeable lithium and sodium ion batteries, *Journal of Power Sources* **2013**, 222, 461-466.

(26) Jiang, H.; Ma, J.; Li, C., Mesoporous carbon incorporated metal oxide nanomaterials as supercapacitor electrodes, *Advanced Materials* **2012**, 24, 4197-4202.

(27) Liu, J.; Zhang, Q.; Yang, J.; Ma, H.; Tade, M. O.; Wang, S.; Liu, J., Facile synthesis of carbon-doped mesoporous anatase TiO_2 for the enhanced visible-light driven photocatalysis, *Chemical Communication* **2014**, 50, 13971-13974.

(28) Martinez, C.; Corma, A., Inorganic molecular sieves: preparation, modification and industrial application in catalytic processes, *Coordination Chemistry Reviews* **2011**, 255, 1558-1580.

(29) Choura, M.; Belgacem, N. M.; Gandini, A., Acid-catalyzed polycondensation of furfuryl alcohol: mechanisms of chromophore formation and cross-linking, *Macromolecules* **1996**, 29, 3839-3850.

(30) Mareche, J. F.; Begin, D.; Furdin, G.; Puricelli, S.; Pajak, J.; Albiniak, A.; Jasienko-Halat, M.; Siemieniewska, T., Monolithic activated carbons from resin impregnated expanded graphite, *Carbon* **2001**, 39, 771-773.

(31) Niederberger, M.; Bartl, M. H.; Stucky, G. D., Benzyl alcohol and titanium tetrachloride - a versatile reaction system for the nonaqueous and low-temperature preparation of crystalline and luminescent titania nanoparticles, *Chemisty of Materials* **2002**, 14, 4364-4370.

(32) Garnweitner, G.; Grote, C., In situ investigation of molecular kinetics and particle formation of water-dispersible titania nanocrystals, *Physical Chemistry Chemical Physics* **2009**, 11, 3767-3774.

(33) Brunauer, S.; Emmett, P. H.; Teller, E., Adsorption of gases in multimolecular layers, *Journal of American Chemical Society* **1938**, 60, 309-318.

(34) Barrett, E. P.; Joyner, L. G.; Halenda, P. P., The determination of pore volume and area distributions in porous substances. 1. Computations from nitrogen isotherms, *Journal of American Chemical Society* **1951**, 73, 373-380.

(35) Luo, W.; Schardt, J.; Bommier, C.; Wang, B.; Razink, J.; Simonsen, J.; Ji, X. L., Carbon nanofibers derived from cellulose nanofibers as a long-life anode material for rechargeable sodium ion batteries, *Journal of Materials Chemistry A* **2013**, 1, 10662-10666.

(36) Kim, K.-T.; Ali, G.; Chung, K. Y.; Yoon, C. S.; Yashiro, H.; Sun, Y.-K.; Lu, J.; Amine, K.; Myung, S.-T., Anatase titania nanorods as an intercalation anode material for rechargeable sodium batteries, *Nano Letters* **2014**, 14, 416-422.

(37) Lee, M. N.; Mohraz, A., Bicontinuous macroporous materials from Bijel templates, *Advanced Materials* **2010**, 22, 4836-4841.

(38) Herzig, E. M.; White, K. A.; Schofield, A. B.; Poon, W. C. K.; Clegg, P. S., Bicontinuous emulsions stabilized solely by colloidal particles, *Nature Materials* **2007**, 6, 966-971.

(39) Zhu, J.; Yang, J.; Bian, Z.-F.; Ren, H.; Liu, Y.-M.; Cao, Y.; Li, H.-X.; He, H.-Y.; Fan, K.-N., Nanocrystalline anatase TiO_2 photocatalysts prepared via a facile low temperature nonhydrolytic sol-gel reaction of $TiC1_4$ and benzyl alcohol, *Applied Catalysis B-Environmental* **2007**, 76, 82-91.

(40) Song, C.; Wang, T.; Wang, X.; Qiu, J.; Cao, Y., Preparation and gas separation properties of poly(furfuryl alcohol)-based C/CMS composite membranes, *Separation and Purification Technology* **2008**, 58, 412-418.

(41) Senapati, K. K.; Borgohain, C.; Phukan, P., $CoFe_2O_4$-ZnS nanocomposite: a magnetically recyclable photocatalyst, *Catalysis Science & Technology* **2012**, 2, 2361-2366.

(42) Vu, A.; Stein, A., Multiconstituent synthesis of $LiFePO_4$/C composites with hierarchical porosity as cathode materials for lithium ion batteries, *Chemistry of Materials* **2011**, 23, 3237-3245.

(43) Mi, H. Y.; Xu, Y. L.; Shi, W.; Yoo, H. D.; Park, S. J.; Park, Y. W.; Oh, S. M., Polymer-derived carbon nanofiber network supported SnO_2 nanocrystals: a superior lithium secondary battery material, *Journal of Materials Chemistry* **2011**, 21, 19302-19309.

(44) Hasegawa, G.; Ishihara, Y.; Kanamori, K.; Miyazaki, K.; Yamada, Y.; Nakanishi, K.; Abe, T., Facile preparation of monolithic $LiFePO_4$/carbon composites with well-defined macropores for a lithium-ion battery, *Chemistry of Materials* **2011**, 23, 5208-5216.

(45) Wu, Y. M.; Wen, Z. H.; Li, J. H., Hierarchical carbon-coated $LiFePO_4$ nanoplate microspheres with high electrochemical performance for Li-ion batteries, *Advanced Materials* **2011**, 23, 1126-1129.

(46) Xu, Y.; Zhu, Y.; Liu, Y.; Wang, C., Electrochemical performance of porous carbon/Tin composite anodes for sodium-ion and lithium-ion batteries, *Advanced Energy Materials* **2013**, 3, 128-133.

(47) Ji, X.; Herle, S.; Rho, Y.; Nazar, L. F., Carbon/MoO_2 composite based on porous semi-graphitized nanorod assemblies from in-situ reaction of tri-block polymers, *Chemistry of Materials* **2007**, 19, 374-383.

(48) Ravikovitch, P. I.; Neimark, A. V., Experimental confirmation of different mechanisms of evaporation from ink-bottle type pores: equilibrium, pore blocking, and cavitation, *Langmuir* **2002**, 18, 9830-9837.

(49) Ji, L.; Gu, M.; Shao, Y.; Li, X.; Engelhard, M. H.; Arey, B. W.; Wang, W.; Nie, Z.; Xiao, J.; Wang, C.; Zhang, J.-G.; Liu, J., Controlling SEI formation on SnSb-porous carbon nanofibers for improved Na ion storage, *Advanced Materials* **2014**, 26, 2901-2908.

(50) Pan, H. L.; Hu, Y. S.; Chen, L. Q., Room-temperature stationary sodium-ion batteries for large-scale electric energy storage, *Energy & Environmental Science* **2013**, 6, 2338-2360.

(51) Chen, T.; Liu, Y.; Pan, L.; Lu, T.; Yao, Y.; Sun, Z.; Chua, D. H. C.; Chen, Q., Electrospun carbon nanofibers as anode materials for sodium ion batteries with excellent cycle performance, *Journal of Materials Chemistry A* **2014**, 2, 4117-4121.

(52) Xu, Y.; Lotfabad, E. M.; Wang, H. L.; Farbod, B.; Xu, Z. W.; Kohandehghan, A.; Mitlin, D., Nanocrystalline anatase TiO_2: a new anode material for rechargeable sodium ion batteries, *Chemical Communications* **2013**, 49, 8973-8975.

(53) Ponrouch, A.; Goni, A. R.; Palacin, M. R., High capacity hard carbon anodes for sodium ion batteries in additive free electrolyte, *Electrochemistry Communications* **2013**, 27, 85-88.

(54) Yoon, S. B.; Jegal, J. P.; Roh, K. C.; Kim, K. B., Electrochemical impedance spectroscopic investigation of sodium ion diffusion in MnO_2 using a constant phase element active in desired frequency ranges, *Journal of the Electrochemical Society* **2014**, 161, H207-H213.

(55) Yu, P.; Ritter, J. A.; White, R. E.; Popov, B. N., Ni-composite microencapsulated graphite as the negative electrode in lithium-ion batteries - II. Electrochemical impedance and self-discharge studies, J *Journal of the Electrochemical Society* **2000**, 147, 2081-2085.

(56) Markovsky, B.; Levi, M. D.; Aurbach, D., The basic electroanalytical behavior of practical graphite-lithium intercalation electrodes, *Electrochimica Acta* **1998**, 43, 2287-2304.

CHAPTER IV

(1) Tarascon, J. M.; Armand, M., Issues and challenges facing rechargeable lithium batteries, *Nature* **2001**, 414, 359-367.

(2) Goodenough, J. B.; Kim, Y., Challenges for Rechargeable Li Batteries, *Chemistry of Materials* **2010**, 22, 587-603.

(3) Reddy, A. L. M.; Gowda, S. R.; Shaijumon, M. M.; Ajayan, P. M., Hybrid Nanostructures for Energy Storage Applications, *Advanced Materials* **2012**, 24, 5045-5064.

(4) Kim, M. G.; Cho, J., Reversible and High-Capacity Nanostructured Electrode Materials for Li-Ion Batteries, *Advanced Functional Materials* **2009**, 19, 1497-1514.

(5) Shcherbakova, A.; Kleit, A.; Cho, J., The value of energy storage in South Korea's electricity market: a hotelling approach, *Applied Energy* **2014**, 125, 93-102.

(6) Bommier, C.; Luo, W.; Gao, W. Y.; Greaney, A.; Ma, S. Q.; Ji, X., Predicting capacity of hard carbon anodes in sodium-ion batteries using porosity measurements, *Carbon* **2014**, 76, 165-174.

(7) Lee, J.; Chen, Y. M.; Zhu, Y.; Vogt, B. D., Fabrication of Porous Carbon/TiO_2 Composites through Polymerization-Induced Phase Separation and Use As an Anode for Na-Ion Batteries, *ACS Applied Materials & Interfaces* **2014**, 6, 21011-21018.

(8) Doeff, M. M.; Cabana, J.; Shirpour, M., Titanate Anodes for Sodium Ion Batteries, *Journal of Inorganic and Organometallic Polymers and Materials* **2014**, 24, 5-14.

(9) Chen, T.; Liu, Y.; Pan, L.; Lu, T.; Yao, Y.; Sun, Z.; Chua, D. H. C.; Chen, Q., Electrospun carbon nanofibers as anode materials for sodium ion batteries with excellent cycle performance, *Journal of Materials Chemistry A* **2014**, 2, 4117-4121.

(10) Luo, W.; Schardt, J.; Bommier, C.; Wang, B.; Razink, J.; Simonsen, J.; Ji, X. L., Carbon nanofibers derived from cellulose nanofibers as a long-life anode material for rechargeable sodium-ion batteries, *Journal of Materials Chemistry A* **2013**, 1, 10662-10666.

(11) Ponrouch, A.; Goni, A. R.; Palacin, M. R., High capacity hard carbon anodes for sodium ion batteries in additive free electrolyte, *Electrochemistry Communications* **2013**, 27, 85-88.

(12) Tang, K.; Fu, L.; White, R. J.; Yu, L.; Titirici, M.-M.; Antonietti, M.; Maier, J., Hollow carbon nanospheres with superior rate capability for sodium-based batteries, *Advanced Energy Materials* **2012**, 2, 873-877.

(13) Wenzel, S.; Hara, T.; Janek, J.; Adelhelm, P. Room-temperature sodium-ion batteries: Improving the rate capability of carbon anode materials by templating strategies, *Energy & Environmental Science* **2011**, 4, 3342-3345.

(14) Alcantara, R.; Lavela, P.; Ortiz, G. F.; Tirado, J. L., Carbon microspheres obtained from resorcinol-formaldehyde as high-capacity electrodes for sodium-ion batteries, *Electrochemical and Solid State Letters* **2005**, 8, A222-A225.

(15) Bi, Z.; Paranthaman, M. P.; Menchhofer, P. A.; Dehoff, R. R.; Bridges, C. A.; Chi, M.; Guo, B.; Sun X.; Dai, S., Self-organized amorphous TiO_2 nanotube arrays on porous Ti foam for rechargeable lithium and sodium ion batteries, *Journal of Power Sources* **2013**, 222, 461-466.

(16) Wu, L.; Buchholz, D.; Bresser, D.; Chagas, L. G.; Passerini, S., Anatase TiO_2 nanoparticles for high power sodium-ion anodes, *Journal of Power Sources* **2014**, 251, 379-385.

(17) Yan, Z.; Liu, L.; Tan, J.; Zhou, Q.; Huang, Z.; Xia, D.; Shu, H.; Yang, X.; Wang, X., One-pot synthesis of bicrystalline titanium dioxide spheres with a coreeshell structure as anode materials for lithium and sodium ion batteries, *Journal of Power Sources* **2014**, 269, 37-45.

(18) Wu, L.; Bresser, D.; Buchholz, D.; Giffin, G. A.; Castro, C. R.; Ochel, A.; Passerini, S., Unfolding the mechanism of sodium insertion in anatase TiO_2 nanoparticles, *Advanced Energy Materials* **2015**, 5, 1401142-1401152.

(19) Xiong, H.; Slater, M. D.; Balasubramanian, M.; Johnson, C. S.; Rajh, T., Amorphous TiO_2 nanotube anode for rechargeable sodium ion batteries, *Journal of Physical Chemistry Letters* **2011**, 2, 2560-2565.

(20) Bresser, D.; Oschmann, B.; Tahir, M. N.; Mueller, F.; Lieberwirth, I.; Tremel, W.; Zentel, R.; Passerini, S., Carbon-coated anatase TiO_2 nanotubes for Li- and Na-ion Anodes, *Journal of The Electrochemical Society* **2015**, 162, A3013-A3020.

(21) Cha, H. A.; Jeong, H. M.; Kang, J. K., Nitrogen-doped open pore channeled graphene facilitating electrochemical performance of TiO_2 nanoparticles as an anode material for sodium ion batteries, *Journal of Materials Chemistry A* **2014**, 2, 5182-5186.

(22) Yang, Y.; Ji, X.; Jing, M.; Hou, H.; Zhu, Y.; Fang, L.; Yang, X.; Chen, Q.; Banks, C. E., Carbon dots supported upon N-doped TiO_2 nanorods applied into sodium and lithium ion batteries, *Journal of Materials Chemistry A* **2015**, 3, 5648-5655.

(23) Ge, Y.; Jiang, H.; Zhu, J.; Lu, Y.; Chen, C.; Hu, Y.; Qiu, Y.; Zhang, X., High cyclability of carbon-coated TiO_2 nanoparticles as anode for sodium-ion batteries, *Electrochimica Acta* **2015**, 157, 142-148.

(24) Xiao, L.; Cao, Y.; Xiao, J.; Wang, W.; Kovarik, L.; Nie, Z.; Liu, J., High capacity, reversible alloying reactions in SnSb/C nanocomposites for Na-ion battery applications, *Chemical Communications* **2012**, 48, 3321-3323.

(25) Wu, L.; Hu, X.; Qian, J.; Pei, F.; Wu, F.; Mao, R.; Ai, X.; Yang, H.; Cao, Y., A Sn–SnS–C nanocomposite as anode host materials for Na-ion batteries, *Journal of Materials Chemistry A* **2013**, 1, 7181-7184.

(26) Jo, C.; Park, Y.; Jeong, J.; Lee, K. T.; Lee, J., Structural effect on electrochemical performance of ordered porous carbon electrodes for Na-ion batteries, *ACS Applied Materials & Interfaces* **2015**, 7, 11748-11754.

(27) Goriparti, S.; Miele, E.; De Angelis, F.; Di Fabrizio, E.; Zaccaria, R. P.; Capiglia, C., Review on recent progress of nanostructured anode materials for Li-ion batteries, *Journal of Power Sources* **2014**, 257, 421-443.

(28) Ishii, Y.; Kanamori, Y.; Kawashita, T.; Mukhopadhyay, I.; Kawasaki, S., Mesoporous carbon-titania nanocomposites for high-power Li-ion battery anode material, *Journal of Physics and Chemistry of Solids* **2010**, 71, 511-514.

(29) Arora, P.; White, R. E.; Doyle, M., Capacity fade mechanisms and side reactions in lithium-ion batteries, *Journal of The Electrochemical Society* **1998**, 145, 3647-3667.

(30) Markevich, E.; Baranchugov, V.; Salitra, G.; Aurbach, D.; Schmidt, M. A., Behavior of Graphite Electrodes in Solutions Based on Ionic Liquids in In Situ Raman Studies, *Journal of The Electrochemical Society* **2008**, 155, A132-A137.

(31) Agubra, V.; Fergus, J., Lithium ion battery anode aging mechanisms, *Materials* **2013**, 6, 1310-1325.

(32) Muñoz-Márquez, M. A.; Zarrabeitia, M.; Castillo-Martínez, E.; Eguía-Barrio, A.; Rojo, T.; Casas-Cabanas, M., Composition and evolution of the solid-electrolyte interphase in $Na_2Ti_3O_7$ electrodes for Na-ion batteries: XPS and Auger parameter analysis, *ACS Applied Materials & Interfaces* **2015**, 7, 7801-7808.

(33) Oh, S.; Hwang, J.; Yoon, C. S.; Lu, J.; Amine, K.; Belharouak, I.; Sun, Y., High electrochemical performances of microsphere C-TiO_2 anode for sodium-ion battery, *ACS Applied Materials & Interfaces* **2014**, 6, 11295-11301.

(34) Marêché, J. F.; Bégin, D.; Furdin, G.; Puricelli, S.; Pajak, J.; Albiniak, A.; Jasienko-Halat, M.; Siemieniewska, T., Monolithic activated carbons from resin impregnated expanded graphite, *Carbon* **2001**, 39, 771-773.

(35) Chen, H.; Chen, S.; Li, L.; Jin, S., Quantitative determination of ε-phase in polymorphic HNIW using X-ray diffraction patterns, *Propellants, Explosives, Pyrotechnics* **2008**, 33, 467-471.

(36) Sing, K., The use of nitrogen adsorption for the characterisation of porous materials, *Colloids and Surfaces A: Physicochemical and Engineering Aspects* **2001**, 187, 3-9.

(37) Kim, K.; Ali, G.; Chung, K. Y.; Yoon, C. S.; Yashiro, H.; Sun, Y.; Lu, J.; Amine, K.; Myung, S., Anatase titania nanorods as an intercalation anode material for rechargeable sodium batteries, *Nano Letters* **2014**, 14, 416-422.

(38) Yoon, S. B.; Jegal, J. P.; Roh, K. C.; Kim, K. B., Electrochemical impedance spectroscopic investigation of sodium ion diffusion in MnO_2 using a constant phase element active in desired frequency ranges, *Journal of the Electrochemical Society* **2014**, 161, H207-H213.

(39) Tanaka, S.; Doi, A.; Matsui, T.; Miyake, Y., Mass transport and electrolyte accessibility through hexagonally ordered channels of self-assembled mesoporous carbons, *Journal of Power Sources* **2013**, 228, 24-31.

(40) Ramasamy, R. P.; Feger, C.; Strange, T.; Popov, B. N., Discharge characteristics of silver vanadium oxide cathodes, *Journal of Applied Electrochemistry* **2006**, 36, 487-497.

(41) Yan, D.; Yu, C.; Bai, Y.; Zhang, W.; Chen, T.; Hu, B.; Sun, Z.; Pan, L., Sn-doped TiO*2* nanotubes as superior anode materials for sodium ion batteries, *Chemical Communications* **2015**, 51, 8261-8264.

(42) Chen, T.; Guai, G. H.; Gong, C.; Hu. W.; Zhu, J.; Yang, H.; Yan, Q.; Li, C. M., Thermoelectric Bi_2Te_3-improved charge collection for high-performance dyesensitized solar cells, *Energy & Environmental Science* **2012**, 5, 6294-6298.

(43) Hu, W.; Li, L.; Tong, W.; Li, G.; Yan, T., Tailoring the nanoscale boundary cavities in rutile TiO2 hierarchical microspheres for giant dielectric performance, *Journal of Materials Chemistry* **2010**, 20, 8659-8667.

(44) Fong, R.; Vonsacken, U.; Dahn, J. R., Studies of lithium intercalation into carbons using nonaqueous electrochemical-cells, *Journal of the Electrochemical Society* **1990**, 137, 2009-2013.

(45) Ji, L.; Gu, M.; Shao, Y.; Li, X.; Engelhard, M. H.; Arey, B. W.; Wang, W.; Nie, Z.; Xiao, J.; Wang, C.; Zhang, J.-G.; Liu, J., Controlling SEI formation on SnSb-porous carbon nanofibers for improved Na ion storage, *Advanced Materials* **2014**, 26, 2901-2908.

(46) Komaba, S.; Murata, W.; Ishikawa, T.; Yabuuchi, N.; Ozeki, T.; Nakayama, T.; Ogata, A.; Gotoh, K.; Fujiwara, K., Electrochemical Na insertion and solid electrolyte interphase for hard-carbon electrodes and application to Na-ion batteries, *Advanced Functional Materials* **2011**, 21, 3859-3867.

(47) Lee, J. T.; Nitta, N.; Benson, J.; Magasinski, A.; Fuller, T. F.; Yushin, G., Comparative study of the solid electrolyte interphase on graphite in full Li-ion battery cells using X-ray photoelectron spectroscopy, secondary ion mass spectrometry, and electron microscopy, *Carbon* **2013**, 52, 388-397.

(48) Eshkenazi, V.; Peled, E.; Burstein, L.; Golodnitsky, D., XPS analysis of the SEI formed on carbonaceous materials, *Solid State Ionics* **2004**, 170, 83-91.

(49) An, Y.; Zuo, P.; Du, C.; Ma, Y.; Cheng, X.; Lin, J.; Yin, G., Effects of VC-LiBOB binary additives on SEI formation in ionic liquid-organic composite electrolyte, *RSC Advances* **2012**, *2*, 4097-4102.

(50) Verma, P.; Maire, P.; Novak, P., A review of the features and analyses of the solid electrolyte interphase in Li-ion batteries, *Electrochimica Acta* **2010**, 55, 6332-6341.

(51) Yuan, W.; Zhou, Y.; Li, Y.; Li, C.; Peng, H.; Zhang, J.; Liu, Z.; Dai, L.; Shi, G., The edge- and basal-plane-specific electrochemistry of a single-layer graphene sheet, *Scientific Reports* **2013**, 3.

(52) Zaghib, K.; Nadeau, G.; Kinoshita, K., Influence of edge and basal plane sites on the electrochemical behavior of flake-like natural graphite for Li-ion batteries, *Journal of Power Sources* **2001**, 97-8, 97-103.